Plasmonics (2023) 18:441–483
https://doi.org/10.1007/s11468-022-01775-9

THz Imaging Technology Trends and Wide Variety of Applications: a Detailed Survey

Vulugundam Anitha[1] · Ankur Beohar[1] · Anveshkumar Nella[1]

Received: 23 September 2022 / Accepted: 14 December 2022 / Published online: 4 January 2023

Abstract
Terahertz (THz) imaging is a non-invasive and high spatial-resolution technique that uses non-ionizing electromagnetic signals in a frequency range of 0.1–10 THz. Hence, this article focuses on diverse THz imaging techniques, THz antennas and designing methods, image reconstruction algorithms, and its applications. The antennas include planar patch, photoconductive, dielectric-resonator, substrate-integrated waveguide, wire, and wave guide. In this study, it is noted that antennas with high efficient conducting materials having a compact size, high gain, and high directional properties are required for THz imaging. The image reconstruction algorithms cover back-projection algorithm, range migration algorithm, phase-shift migration algorithm, single-band compressed sensing reconstruction and compressed sensing hyper spectral image reconstruction. High-resolution image reconstruction algorithms and challenges are also reported. From this study, it is noted that a multi–input–multi–output-based phase shift migration algorithm is used for THz imaging due to its high-accuracy and low computation time. It is also noted that the image quality can be enhanced by introducing an inverse fresnel diffraction algorithm into THz images retrieved by compressed sensing. Applications of THz imaging focus on cell detection (tissue-detection, cancer-detection, and bacteria-detection), concealed objects detection, food safety and quality inspection, and monitoring the water level of plant leaves.

Keywords Back projection algorithm · Compressed sensing · Concealed object detection · Phase-shift migration algorithm · Range migration algorithm · THz imaging

Introduction

Terahertz frequency band 0.1–10 THz is commonly considered an essential tool for addressing the requirements of technologies and applications that demand high-speed transmission and high-resolution imaging. These technologies are quickly developing and have an extensive range of potential applications including remote sensing, biological detection, ultra-fast short-range wireless communications, and basic material research. One of THz radiation's most prominent benefits is its capacity to penetrate a variety of materials including those that are opaque to visible and near-infrared light or produce only low-contrast X-ray images, such as plastics, wood and paper, textiles, and semiconductors. As demonstrated in Fig. 1, the use of shorter wavelengths in the THz range results in noticeably higher imaging resolution, which is useful in many applications. Applications of THz technology include diagnostic imaging, sensing, communications, industrial quality assurance systems, security inspection, military and biomedical health, and technical diagnostic systems. As part of its black-body radiation, everything greater than around 10 K emits THz radiation [1]. For an accurate description of the cold (10–20 K) dust found in the Milky Way galaxy's interstellar medium, observations at these frequencies are essential. However, in far-off starburst galaxies, this thermal emission is incredibly weak. Gyrotrons, backward wave oscillators (BWO), far-infrared lasers (also known as "fir lasers"), quantum cascade lasers, free electron lasers (Fel), synchrotron light sources, photo mixing sources, and single-cycle sources, including photoconductive, surface field, photo-Dember, and optical

✉ Vulugundam Anitha
anitha.vulugundam@gmail.com

Ankur Beohar
ankurbeohar16@gmail.com

Anveshkumar Nella
nellaanvesh@gmail.com

[1] School of EEE, VIT Bhopal University, Bhopal, India 466114

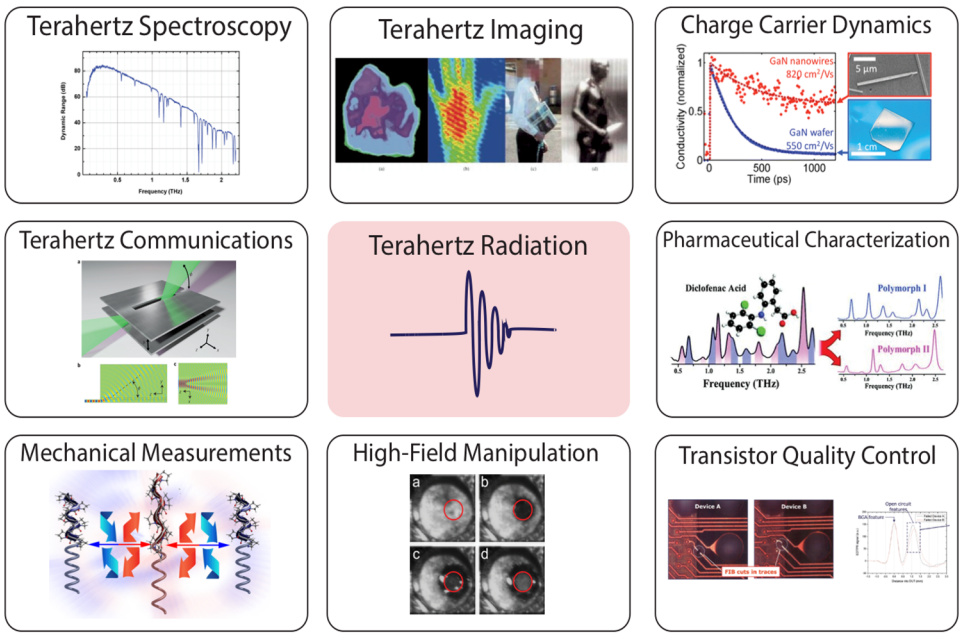

Fig. 1 THz applications

rectification emitters, are possible sources of THz radiation. In order to create waves in the THz band at 542 GHz, a novel source was created that employed a resonant tunneling diode (RTD) in which the voltage dropped as the current increased [1, 2].

THz imaging technology has a wide range of potential applications but has not yet been put into practical use due to the high equipment costs and/or the requirement for highly qualified operators. This is because, unlike the visible domain where all current smart phones have megapixel imaging arrays, it is challenging to construct a THz pixelated-detector array since there are not enough suitable materials available. Due to their narrowband or cryogenic temperature requirements, the majority of multipixel THz-detector arrays now in use are narrowband [3, 4]. However, micro bolometer arrays hold considerable potential because they are capable of wideband detection at room temperature [5]. Micro bolometer arrays have actually been used with digital holography to create amplitude and phase images at a single THz frequency [6, 7]. Contrarily, to achieve the sub-picosecond temporal resolution provided by THz-spectrometers, spectral pictures would need to be taken several times at different frequencies, which is necessary to see ultra-fast dynamics. Even though the aforementioned problems can be avoided by mapping out a THz image [8] using electro-optic THz detection and an optical CCD array, this method necessitates a Ti: Sapphire laser with a low repetition rate regeneration amplifier, which makes the system a whole expensive, bulky, and rigid.

Over the past two decades, THz science and technology have undergone significant development. New THz sources may allow for extremely quick THz imaging systems. Numerous THz imaging and spectroscopy systems are built on the foundation of photoconductive antennas, which also have exciting potential in a wide range of scientific domains. A commercial fiber-coupled photoconductive antenna is used as the THz source in this real-time THz imaging technique and an uncooled microbolometer camera is used as the detection device. However, compact and small THz antenna sources with on-chip manufacturing and excellent directivity are needed for imaging applications in order to produce a deep depth of field for greater picture resolution. High Q-factor graphene-loaded aperture antennas are also able to detect breast cancer cells. Better imaging can be achieved by combining an antenna with a radio in a technique that can be thought of as a sensor. THz digital holography (TDH) is positioned to replace conventional terahertz imaging methods in a useful, perhaps revolutionary way by integrating the advantages of widely available sources. A full-field phase imaging technique is reflective THz digital holography (TDH). It can acquire the surface profile and depth information of the sample and the amplitude and phase information from the numerical reconstruction of a recorded digital hologram. It has been employed for imaging of the sample concealed behind the material, which is transparent to THz wave, in contrast to the transmission TDH. Reflection TDH can record holograms using two parallel recording planes to produce high-resolution images. The iterative phase restoration algorithm eliminates the innate "twin image" problem [9]; however, it requires recording many holograms. Off-axis Fresnel reflection TDH imaging can capture a single-frame hologram that reveals the object's complex amplitude. Fresnel or angular spectrum propagation in the reconstruction procedure calls for precise reconstruction distance and numerous Fourier transforms. A phase

retrieval technique using THz radiation as an alternative to THz digital holography is named as THz ptychography. It is a non-holographic coherent lensless imaging technique. In the THz band, ptychography has recently been proved to be capable of reconstructing the intricate value distributions of both the illumination probe and the object at the same time [10]. It has developed into a desirable and essential imaging technique because it does not need a reference beam and can photograph lengthy samples. Ptychography is often realized using a localized probe to scan the object and several overlapped diffraction patterns, which results in a limited imaging throughput. One technique for obtaining a complex-valued reconstruction of a sample from the measurement of its diffraction pattern is iterative phase retrieval. A phase retrieval approach called the ptychographical iterative engine (or PIE) uses a sequence of diffraction patterns that are recorded as a known illumination function and is translated into a set of overlapping positions with respect to a target sample.

This work focuses on three diverse aspects involved in THz imaging trends. It involves THz antennas and reconstruction algorithms along with mathematical equations and application aspects. The different antennas that are used at THz frequencies include horn antennas, travelling wave corner cube antennas, log periodic antennas, graphene antennas, dielectric resonator antennas, photoconductive antennas, lens antennas, and on-chip antennas. Reconstruction algorithms are also thoroughly discussed along with their methodologies. Terahertz spectroscopy applications in cell detection, concealed object detection in terahertz ranges, food safety and quality inspection, and agricultural applications are discussed in-detail. This kind of extensive research survey study is not reported in the literature, which makes this article as unique for the community.

This paper is broadly divided into 5 major sections. The "THz Antennas" section discusses various THz antenna trends used for THz imaging applications. The "Algorithms for THz Image Reconstruction" section describes state-of-art in numerous algorithms adopted for THz image reconstruction. The "Application Specifics of THz Imaging" section presents different applications of THz imaging in wide variety areas and the "Conclusion" section highlights as a summary of our review.

THz Antennas

As mentioned earlier, compact and small THz antenna sources with on-chip manufacturing and excellent directivity are needed for imaging applications. So, this section explains how to tackle the obstacles and opportunities that come with developing a THz-enabled antenna. The THz system's antenna is a crucial component that requires extreme precision. Compact, high-directional, and high-gain antennas are preferred for high-resolution, low-latency, and high-data-rate THz systems especially in applications with constrained space. When creating the antenna for THz, there are a number of challenges that must be overcome, which calls for the creation of original solutions. THz links will be crucial for high-data-rate communication over short distances. The authors of the paper [11] presented the following antennas for usage in short-range wireless communication systems. (1) In short-range wireless communication systems, a simple rectangular microstrip antenna operating at THz frequencies is used. This microstrip antenna is extremely small, making it ideal for satellite communication. (2) In the sub-THz range, a single-element antenna with a dipole and reflector is utilized. This antenna offers a gain of 5.14 dBi and 38.6% impedance bandwidth between 294 and 410 GHz. (3) Two systems are illustrated that use the same dipole structure but add more directors to boost gain while preserving roughly the same bandwidth. Gains of 8.01 dBi and 9.6 dBi are obtained. (4) To produce a maximum gain of 13.6 dBi with an efficiency of roughly 89% and a planar compact construction commensurate with state-of-the-art literature, an array of 1×4 elements is used. The electromagnetic wave propagation phenomenon in the atmosphere is the fundamental hurdle in creating THz-long-distance wireless communication networks. Satellite-to-satellite communications are unaffected by the environment. Three main design ideas may be derived for contemporary THz antennas based on the evolution of THz antennas as shown in Fig. 2.

Now, this section discusses THz antenna categories as follows. The antennas covered are dipole antenna, microstrip antenna, horn antenna, travelling wave corner cube antenna, log periodic antenna, planar graphene antenna, dielectric resonator antenna, photoconductive antenna, lens antenna, and on-chip antenna.

Microstrip Antennas

The microstrip antenna is an important part of THz-based wireless communication systems. Security to wireless communications with data rates greater than 10 GB/sec is possible [13, 14] with carrier frequencies above 300 GHz. This can be accomplished if oscillators and amplifier sources have fractional bandwidth of around 10%. If sufficiently powerful, compact, and wideband sources are available, this capacity may be realized using fairly straightforward, inexpensive amplitude modulation techniques. Modern advancements in wearable smart gadgets and ultra-high-speed THz communication systems need the development of low-cost, low-profile, highly efficient antenna designs with high directionality. A photonic crystal-based planar antenna for THz applications with photonic bandgap (PBG)-based crystal polyimide substrate is presented in [15]. At resonance frequency 0.63 GHz,

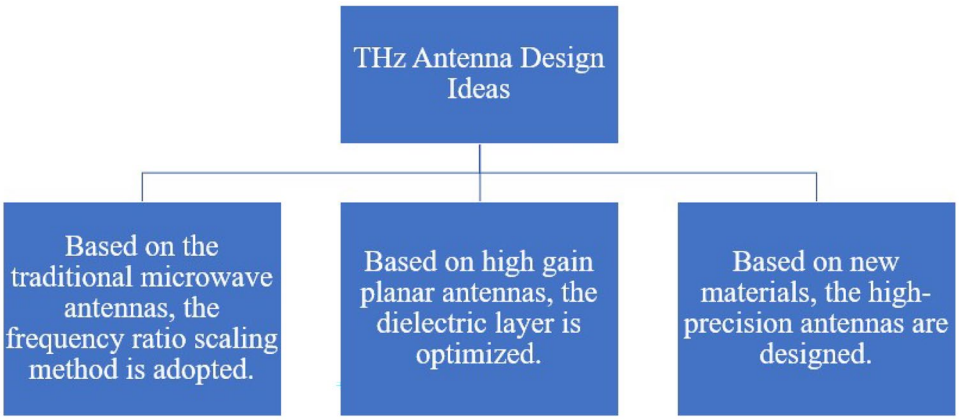

Fig. 2 THz antenna design ideas [12]

this antenna performs optimally in terms of gain (9.45 dB), directivity (9.99 dBi), and exceptionally satisfactory VSWR (< 2). The effects of changing the sizes of the PBG unit cells are also examined in order to achieve a − 10 dB bandwidth of 28.97 GHz (0.616 to 0.64 THz) [15] (Fig. 3).

In [16], a microstrip antenna based on a substrate with a synthesized photonic bandgap (PBG) is created. Authors used a finite integral technique for binary particle swarm optimization (BPSO) that improves the performance of the antenna in terms of side lobe reduction, return loss, and fractional bandwidth. The first design, a dual-band antenna, has a 5.39% lower return loss than the initial antenna built on the air-hole PBG substrate, and the second design has a 128% greater fractional bandwidth (bandwidth of 128 GHz). The gain of both antennas is about 9.17 dB. Initially, Eqs. (1) and (2) are used to compute the width (W_p) and length (L_p) of the rectangular patch, where ε_{reff} is the effective dielectric constant, f_r is the required resonance frequency, c is the speed of light, and h is the antenna substrate thickness [17]. The obtained values are then optimized by modelling metals as perfect electrical conductors.

$$W_p = \frac{c}{2f_r}\sqrt{\frac{2}{\varepsilon_{reff}+1}} \tag{1}$$

$$L_p = \frac{c}{2f_r\sqrt{\varepsilon_{reff}}} - 2\Delta l \tag{2}$$

where

$$\Delta l = 0.412h\frac{(\varepsilon_{reff}+0.3)(\frac{W_p}{h}+0.264)}{(\varepsilon_{reff}-0.258)(\frac{W_p}{h}+0.8)} \tag{3}$$

Figures 4 and 5 show the antennas 1, 2, and 3 and the corresponding optimized filling patterns of unit cells. As compared to the original antenna design, both of these optimization solutions show a reduction in side-lobes. The antennas have a resonance frequency of about 0.65 THz, which is needed for current wireless communication technologies as well as a range of other intriguing applications. According to return loss statistics, using the PBG structure is a smart strategy for lowering surface waves, leading to appreciable improvements.

Horn Antennas

THz antennas are available in a variety of designs, including THz horn antennas, bow-tie dipole, graphene-based antennas, pyramidal cavity with a dipole, dielectric lens planar antennas, photo conductive antennas, and angle reflector array THz antennas for generating THz source radiation. Based on the material used in production, there are three different types of THz antennas: dielectric, metallic, and novel material antennas. In a high-speed THz communication system, the horn antennas shown in Fig. 6 can be utilized as stand-alone antennas or as a feed source for a lens antenna or a transmitting antenna. Horn antennas have been used extensively in high gain THz antennas due to their straight-forward construction, excellent performance, low cross-polarization, and wide frequency spectrum.

A horn antenna is a form of metallic antenna that operates in the THz frequency spectrum. With a gain of 20 to 30 dBi and a low cross-polarization level of − 30 dB, corrugated and dual-mode antennas offer the advantage of symmetric radiation patterns with a coupling efficiency of 97–98%. Due to the THz wave's incredibly high frequency and the horn antenna's relatively small size, processing the horn's tip end can be difficult, especially when creating antenna arrays [22]. The CSIRO ICT Center [23] has offered conventional antennas for THz communication systems such as horns (Fig. 7), transmitters, and lenses, as well as recommendations for THz antenna requirements.

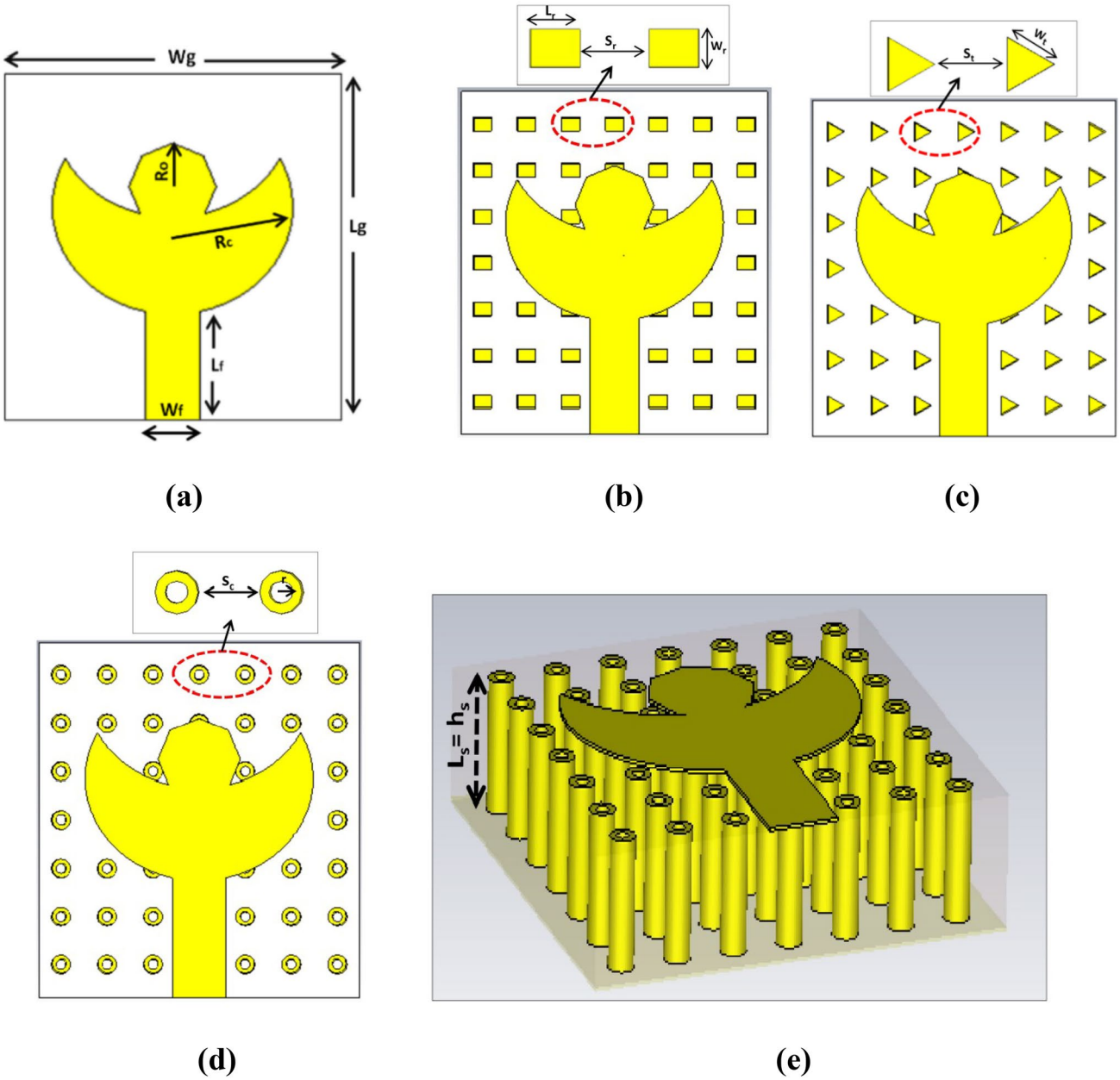

Fig. 3 **a**–**d** PBG-based THz antenna types A–D. **e** Inner view of Type D antenna [15]

Travelling Wave Corner Cube and Log-Periodic Antennas

The travelling wave corner cube antenna [24, 25] is a different metallic antenna that consists of a travelling wave antenna hung within a longitudinal cavity etched on a silicon wafer and incorporated into a 1.2-micron dielectric layer, as illustrated in Fig. 8. Because of its simplistic design and low manufacturing costs, it can be used in frequency bands above 0.6 THz. The side lobe and cross-polarization levels of the antenna are higher, owing to its open structure. As a result, the coupling efficiency (about 50%) of the antenna is relatively low.

Log periodic sinusoidal antennas, logarithmic periodic antennas, dual U-shaped antennas, and butterfly antennas, as shown in Fig. 9, are examples of narrowband and wideband edge-emitting antennas. They can be utilized with low-impedance detectors for THz dielectric antennas. A dielectric substrate and an antenna radiator make up dielectric antennas. When constructed properly, dielectric antennas can achieve impedance matching with the detector which makes the antenna easy to manufacture, integrate, and

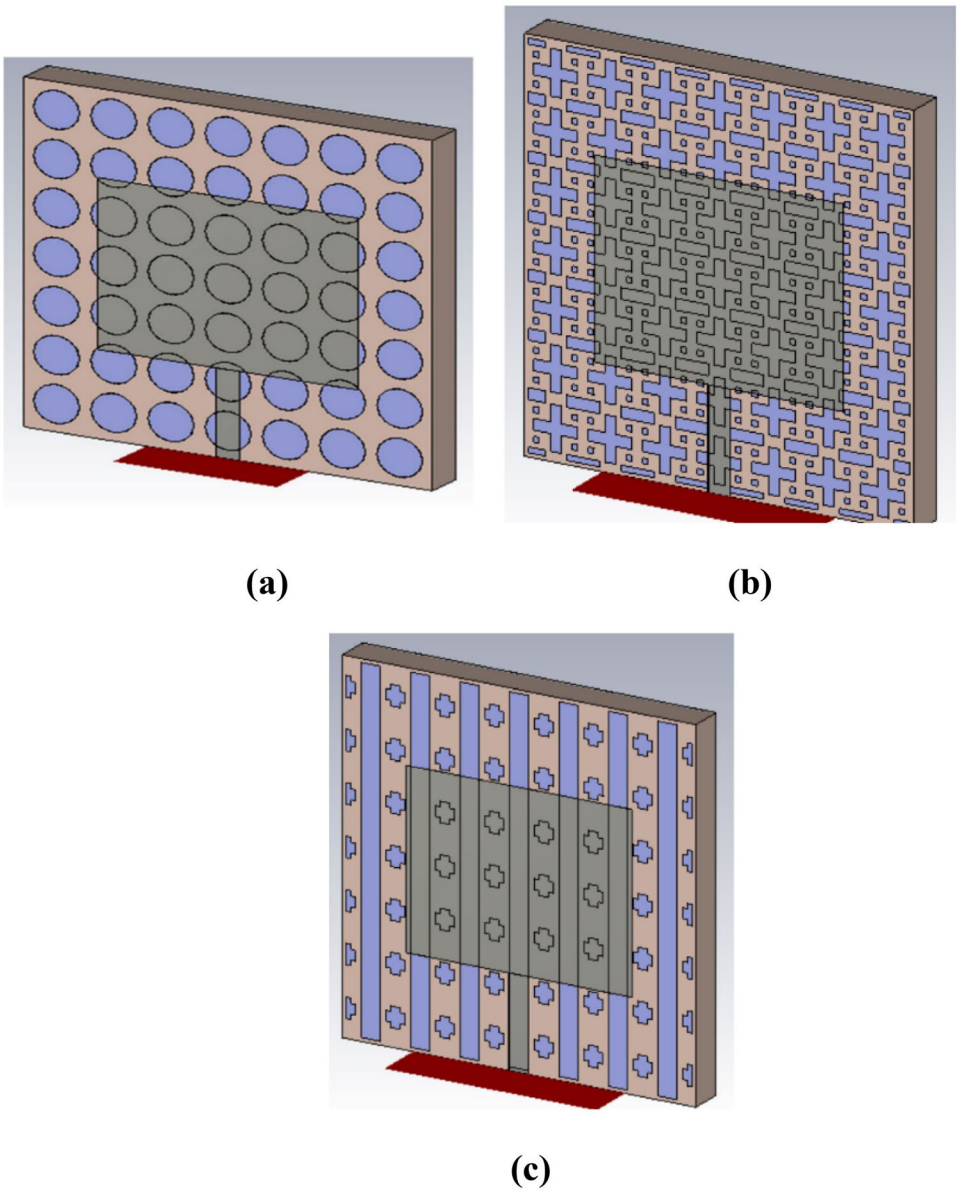

Fig. 4 PBG structures: **a** antenna 1, **b** antenna 2, **c** antenna 3 [16]

1	1	1	0	0	0	0	1	1	1
0	0	0	0	1	1	0	0	0	0
0	1	0	0	1	1	0	0	1	0
0	0	0	0	1	1	0	0	0	0
0	1	1	1	1	1	1	1	1	0
0	1	1	1	1	1	1	1	1	0
0	0	0	0	1	1	0	0	0	0
0	1	0	0	1	1	0	0	1	0
0	0	0	0	1	1	0	0	0	0
1	1	1	0	0	0	0	1	1	1

(a)

1	1	0	0	0	0	0	0	1	1
1	1	0	0	0	0	0	0	1	1
1	1	0	0	0	0	0	0	1	1
1	1	0	0	1	1	0	0	1	1
1	1	0	1	1	1	1	0	1	1
1	1	0	1	1	1	1	0	1	1
1	1	0	0	1	1	0	0	1	1
1	1	0	0	0	0	0	0	1	1
1	1	0	0	0	0	0	0	1	1
1	1	0	0	0	0	0	0	1	1

(b)

Fig. 5 Optimized unit cell filling pattern: **a** antenna 1, **b** antenna 2 [16]

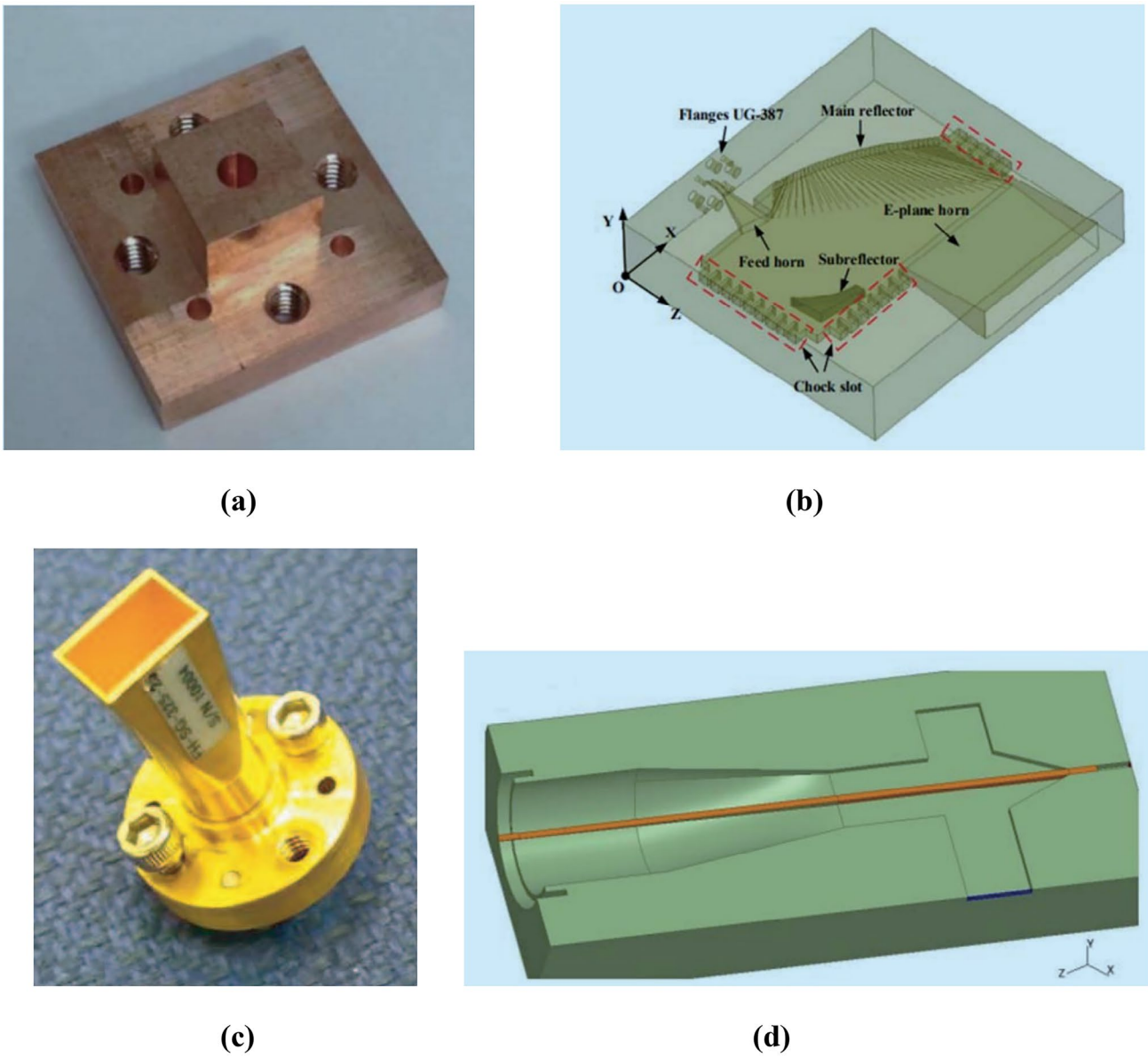

Fig. 6 **a**–**d** THz horn antennas [18–21]

use. More complicated bent-wire antenna shapes can also be designed using a genetic algorithm [26]. However, as the frequency reaches the THz range, a surface wave effect is formed because the dielectric antennas are connected to the dielectric substrate as shown in Fig. 10. This fatal fault causes significant energy loss and a drop in antenna radiation efficiency during operation. The higher-order modes inside the substrate increase in proportion to the thickness of the substrate. As the number of higher-order modes grows, so does the coupling efficiency between the antenna and the substrate medium. Energy is lost as a result of this condition. For decreasing the surface wave effect, three optimization schemes are used: The first is to load the lens onto the antennas, which increases gain by utilizing the antenna bunching feature. The second is to create electromagnetic waves in higher-order modes by reducing the thickness of the substrate. Third, spatial filtering features of an electromagnetic band gap (EBG) can be employed to suppress high-order modes by substituting an EBG for the substrate dielectric material.

Planar Graphene Antennas

Planar graphene antennas, shown in Fig. 11, are gaining popularity as a technique for boosting bandwidth and producing small antennas. Graphene has outstanding dynamic

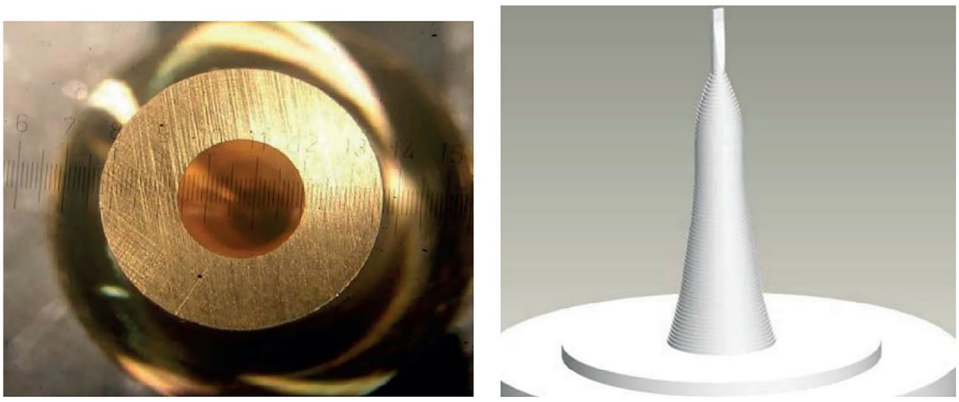

Fig. 7 **a** Horn antenna at 0.84THz and **b** horn antenna at 1.7THz [23]

continuous control qualities by altering the bias voltage and the products of surface plasmons. Surface plasmons are present at the junction of substrates with positive and negative dielectric constants [27, 28]. The plasmon dispersion relation on the metal's surface is described by the Drude model. However, the metal cannot naturally link to and transform energy from electromagnetic waves in free space. To stimulate the surface plasmon wave, further materials are required. When a metal conductor conducts electricity perpendicular to the surface, the surface plasmon wave attenuates rapidly which results in a skin effect [29, 30]. Obviously, the antennas' performance falls dramatically in the high-frequency range due to their small size and skin effect, rendering them unsuitable for THz antennas. Graphene, on the other hand, can absorb and regulate light in a wide variety of wavelengths. THz frequencies are the most prevalent for graphene's in-band transition. Graphene has better surface plasmon material properties thanks to collective plasma oscillation. The surface plasma of graphene not only increases binding and decreases loss, but it also allows for continuous electrical adjustment [31, 32]. Graphene also has a complicated conductivity in the THz frequency band. As a result, the THz plasma mode is linked to sluggish wave propagation. These properties demonstrate that graphene can be used in the THz frequency band to replace metal materials.

For THz applications, authors in [33] implemented an annular dielectric resonator antenna (DRA). A graphene disc is put into a silicon-based DR to achieve frequency response tunability. Figure 12 depicts an antenna configuration with a silicon dioxide substrate ($\epsilon_s = 3.8$) put on top of the conducting ground plane. Using the formulas in Eq. (4) [34], the dimensions were tweaked in an effort to get the intended result.

$$f_{lmn} = \frac{6.324c}{4r_0\pi\sqrt{\epsilon_r + 2}}\left[0.27 + 0.36\left(\frac{r_0}{h}\right) + 0.002\left(\frac{r_0}{h}\right)^2\right] \quad (4)$$

In Eq. (4), the parameters l, m and n are the integers, refer to the field variation in terms of half-wavelength along the azimuth, radius, and height of the DR [35]. Two structures are implemented and evaluated to better understand antenna operation. One is without a graphene disc on top of the silicon DR, and another one is with a graphene disc on top of the silicon DR. Figure 12 shows the resonance of DRA, without a graphene disc at the top, is 4.088 THz. The

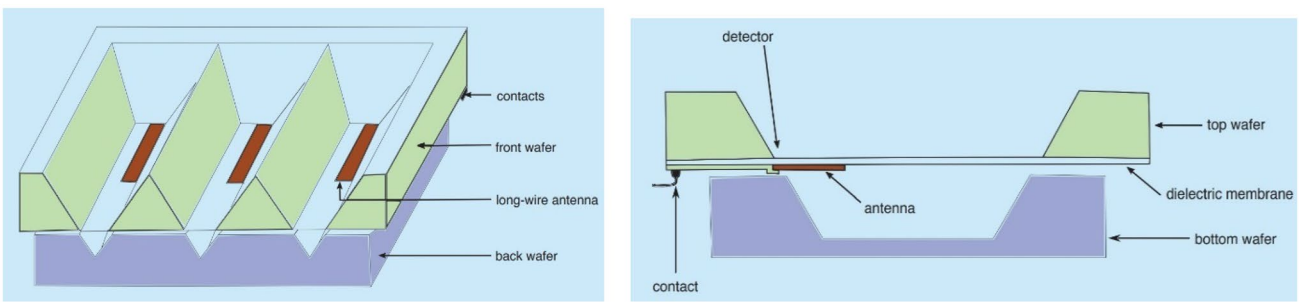

(a) **(b)**

Fig. 8 Travelling wave corner cube antenna **a** configuration and **b** side view [24]

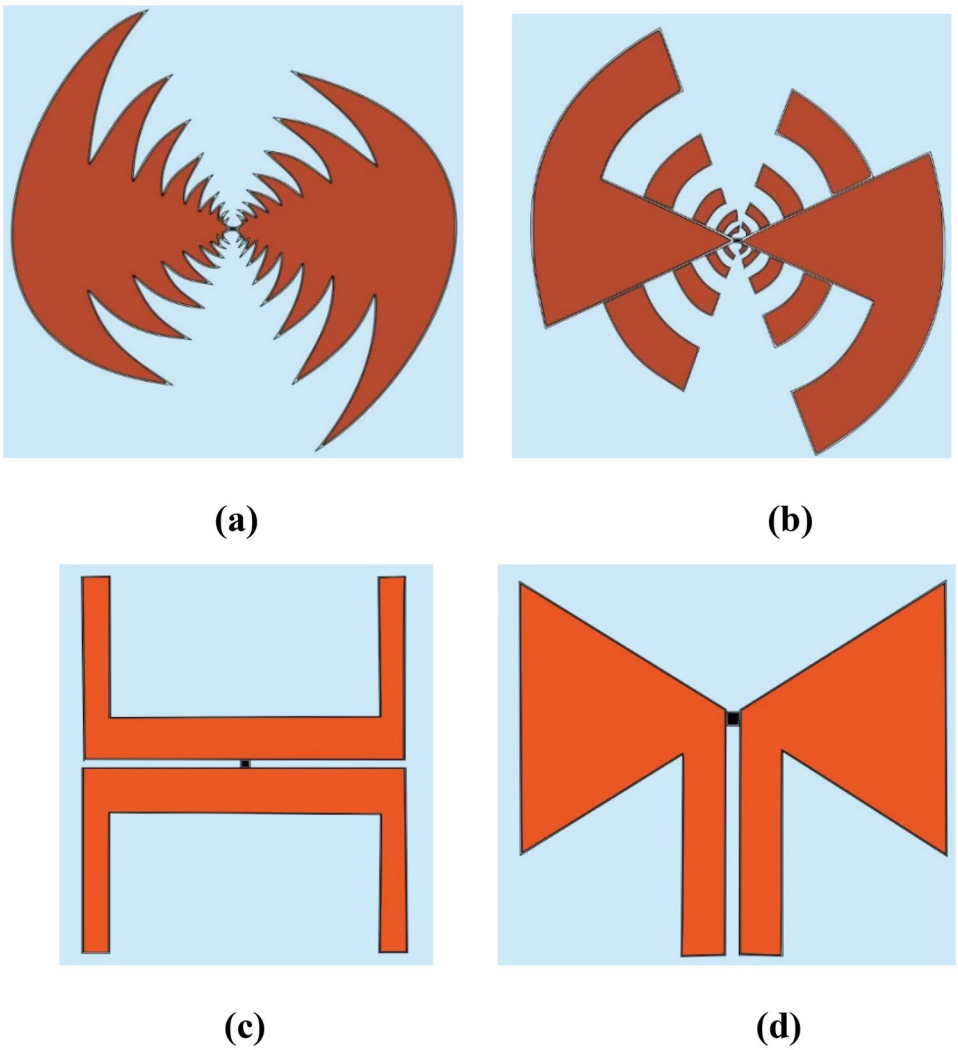

Fig. 9 Planar THz antennas [12]

graphene disc is then placed on top of the antenna, resulting in a new resonance frequency of 4.104 THz. The change in material profile and medium properties at the junction of the silicon DR and graphene barrier can be explained by the shift in resonant frequency that occurs after the graphene disc is installed. The change in resonant frequency also demonstrates that adding a graphene ring merely increases the value of the impedance's inductive and capacitive

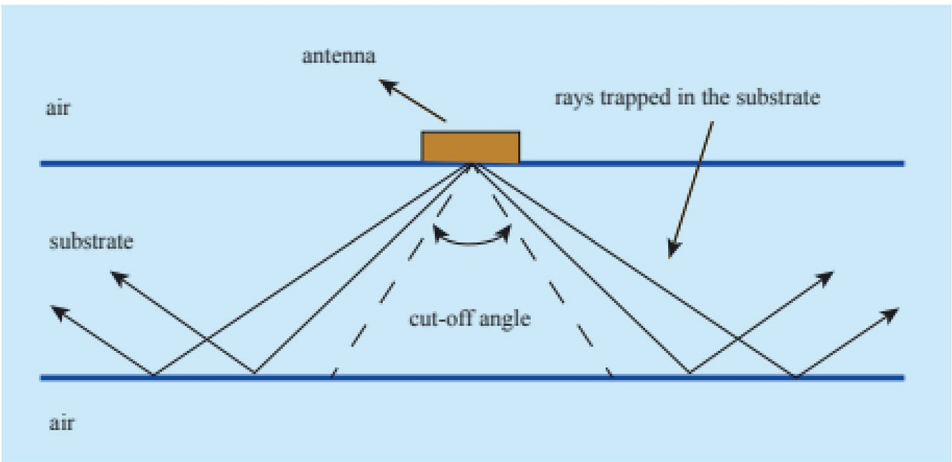

Fig. 10 Diagram illustrating the surface wave effect of an antenna [12]

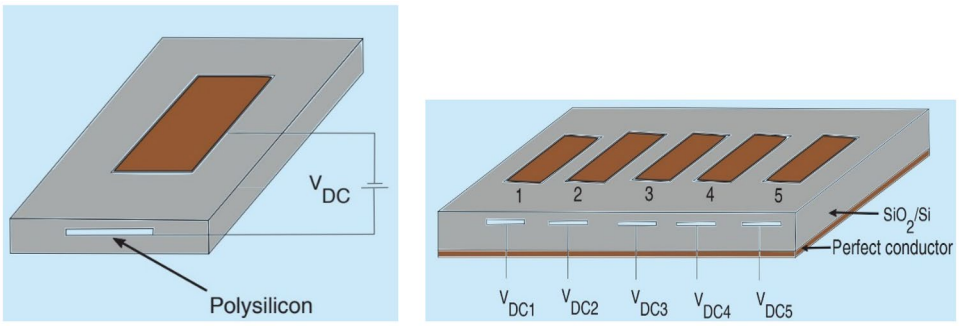

Fig. 11 **a** Nano-patch graphene antenna element. **b** Directional graphene antenna array [27]

components, which may be implemented as a parallel tank circuit using circuit theory [36]. Over the operational pass band, the antenna has a gain and radiation efficiency of above 3 dBi and 72%, respectively as shown in Fig. 12c, d.

Photoconductive Antennas, Horn Antennas, Lens Antennas, and On-Chip Antennas

THz photoconductive antennas, THz horn antennas, THz lens antennas, THz microstrip antennas, and THz on-chip antennas are among the typical five THz antennas. Photoconductive antennas (PCAs) are used to create and detect the THz wave. Photoconductive antenna development and invention have a considerable impact on the THz communication system and related fields. The photoconductive material was exposed to the laser pulse directly in the antenna gap. When a laser beam is shined on a photoconductive semiconductor (such as GaAs, InP, or other comparable materials), an electron–hole pair is produced. The electron–hole pair accelerates the motion to produce photocurrent under the influence of the bias electric field, modifying the conductance between the electrodes. The resulting photoconductive current generates the THz signal if the laser signal is sufficiently brief, roughly 100 fs. The laser used to excite the carriers in the semiconductor is in the infrared frequency range. The PCA is depicted schematically in Fig. 13.

Photoconductive antennas (PCA) exist in a variety of forms, although dipole antennas and big aperture antennas are the most popular. The bow-tie PCA is a dipole antenna deformation among them, while the logarithmic-helical antenna is commonly used for large aperture antenna integration. Bow-tie photoconductive antennas offer a number

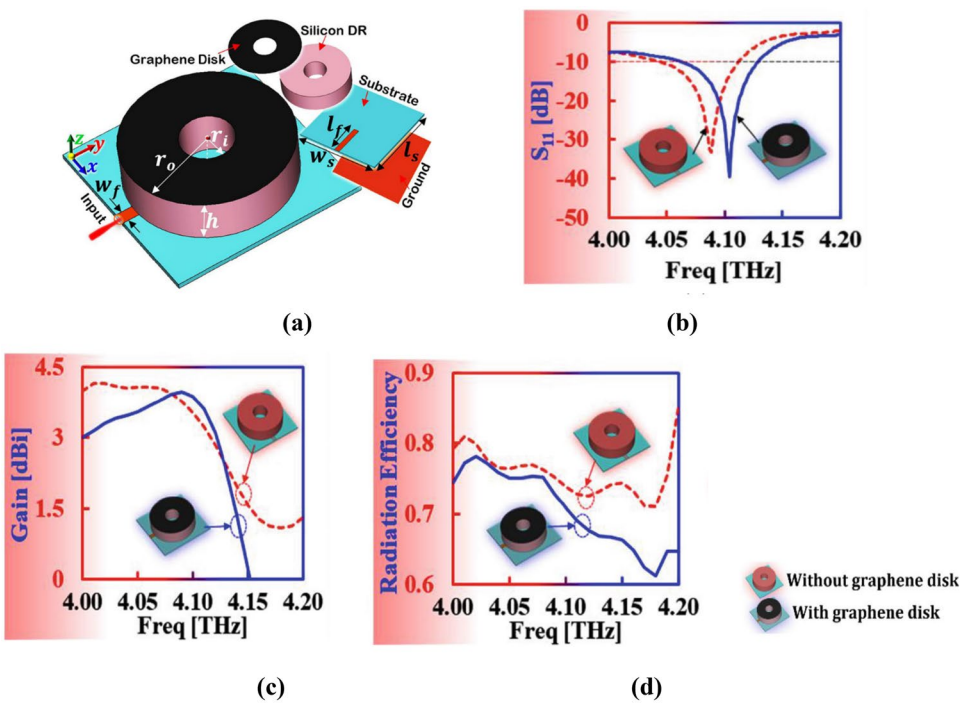

Fig. 12 **a** Geometry of silicon DR-based tunable DRA. **b** S_{11} parameter, **c** gain, and **d** radiation efficiency [33]

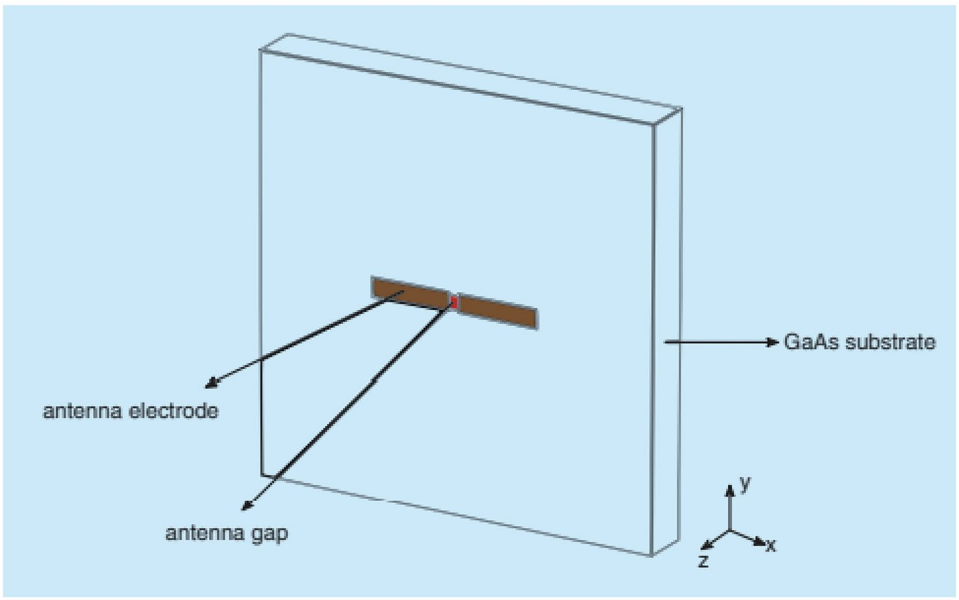

Fig. 13 PCA Schematic [37]

of benefits, including construction simplicity, compactness, miniaturization, and low cost. Photoconductive antennas can benefit from advancements in size, substrate material, and geometry. Log-helical antennas are commonly employed in photoconductive emitters because of their constant radiation impedance and low reactance. The current operational frequency band is mostly in the THz range, with little study in the higher frequency range. Future studies should concentrate on the THz frequency band, implying that log-helix antennas still have a lot of work ahead of them. Figure 14 compares the aperture efficiency, radiation efficiency, and directivity of several bow-tie PCAs. The bow-tie antenna surpasses other types of antennas in terms of radiation efficiency and aperture efficiency, whereas the grid antenna array has the best directivity, as shown in Fig. 14. These models offer good radiation efficiency, directivity, and aperture efficiency, and can be used as a reference for THz antenna designs.

The lens's focusing and imaging characteristics help the THz antennas function better by lowering side-lobe, cross-polarization levels, obtaining high gain, and strong directivity. Lenses come in two varieties: accelerating lenses and delaying antennas. They are categorized based on how much the electromagnetic wave path's electrical length is reduced or enhanced [38]. The former is normally a metal plate lens in the E-plane with a phase velocity larger than the speed of light; the latter is representative with a phase velocity less than the speed of light. The lens' focusing properties may also be utilized to lower side lobes and cross-polarization levels, which is a great design feature for THz antennas. The same can be used to improve the performance of antennas with low directionality and gain (such as horn and waveguide). At the time, both silicone and metal lenses are frequently utilized (Fig. 15). In the construction of integrated antennas, silicon lenses are widely employed. Metal lenses can be produced by hand. More research on the use of lenses in conjunction with innovative technologies or other types of THz antennas is needed. Future THz lens antennas are expected to be able to be miniaturized to satisfy low-cost, high-gain needs.

When antennas are interfaced with integrated circuits (ICs), it is said to be on-chip implementation. This kind of arrangement removes parasitic effects and uncertainty generated by interconnections [45, 50, 51]. This implementation design has flexibility [50] without the need for an additional matching network. So that it saves time, space, and money. But on-chip antennas have a few drawbacks like large losses, unreliable patterns, and low gain [46, 52, 53]. As shown in Fig. 16, an on-chip antenna with a chip-integrated dielectric resonator (CIDR) is presented in [54]. The hybrid DR cavity modes resulted in the increase of the bandwidth as well as the gain. A bandwidth of 28.6% from 284 to 377 GHz is attained for gains greater than 5 dBi. At 295 GHz, the manufactured sample has a peak gain of 8.6 dBi and a maximum radiation efficiency of 44%. The antenna is a potential choice for fully integrated THz transceiver systems due to its wide bandwidth, high gain, and low profile. To the authors' best knowledge, this is the largest fully integrated on-chip antenna (OCA) operating at THz frequencies.

Table 1 provides the performance comparison of different THz antennas. Microstrip antennas are best suitable for short-range wireless communication systems. In photonic crystal-based design, photonic bandgap (PBG) structures are integrated into microstrip patch antennas to achieve better radiation properties. They can achieve a gain of up to 9.17 dB and a radiation efficiency of 91.08%. Moreover, PBG-based substrates can be used to overcome the limitation of surface waves in planar microstrip antennas. Horn antennas are suitable for

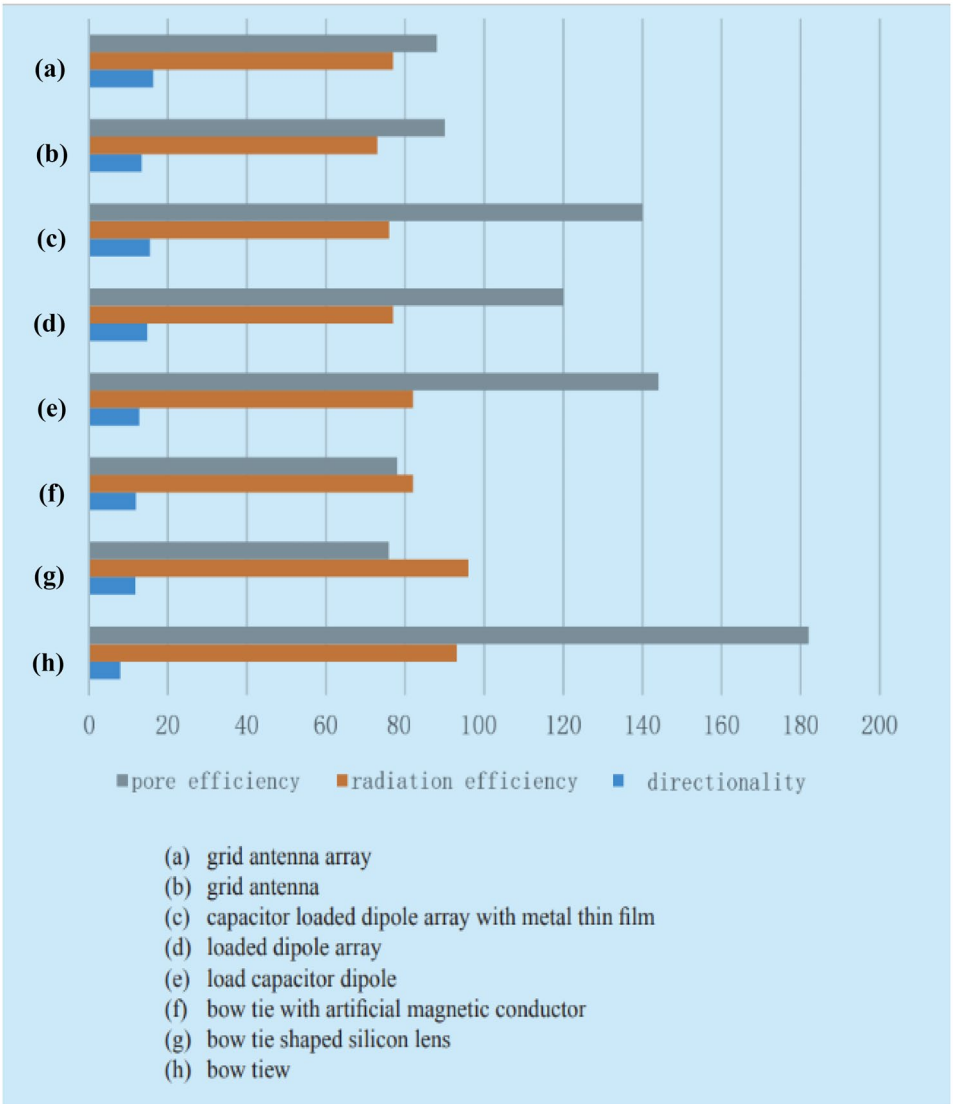

Fig. 14 Comparison among different types of bow-tie PCAs [12]

high-speed THz communication systems. Adding a dielectric lens to horn antennas improves overall antenna gain of 20 to 30 dBi. The remarkable features of graphene have been used to develop tiny and reconfigurable resonant, leaky-wave, and reflect array antennas with unsurpassed THz radiation efficiency and functionality. To accomplish frequency response tunability, a graphene disc is placed in a silicon-based dielectric resonator (DR) and achieves a radiation efficiency of 72–75%. For THz imaging applications, high-directional antennas with high gain and compact size are preferred.

Algorithms for THz Image Reconstruction

THz imaging has been used in a variety of sectors, including biological imaging, non-destructive security evaluation, and industrial process control [55]. THz imaging on the other hand has faced numerous challenges such as limited resolution and definition. The time domain spectroscopic (TDS) technique is the most commonly used THz imaging method. With this technique, the determination of the field amplitude, phase, and polarization can be done simultaneously. THz near-field technology with subwavelength aperture size detecting probes improves the spatial resolution beyond the diffraction limit. However, sometimes it may not be practical during human screening scenarios. Charge-coupled devices (CCDs) [56] and bolo meters [57] in the THz frequency band can be adapted to suit specific imaging applications. Furthermore, the approach of three-dimensional electromagnetic imaging is also feasible because the frequency range employed in the tests is in the millimeter wave region of the electromagnetic spectrum, which lies in the low THz frequency range. Electromagnetic imaging will be the inverse of

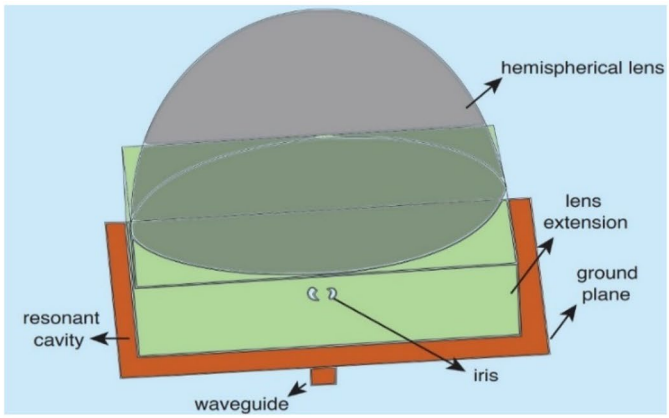

(a)

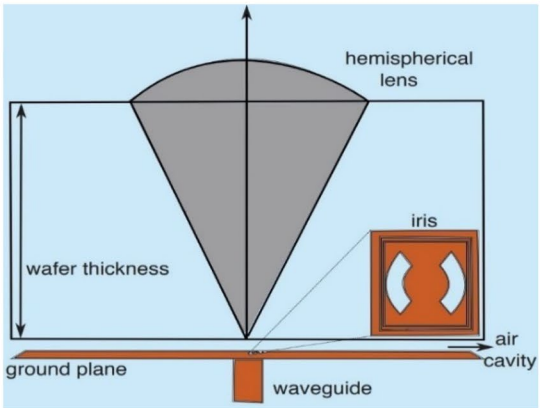

(b)

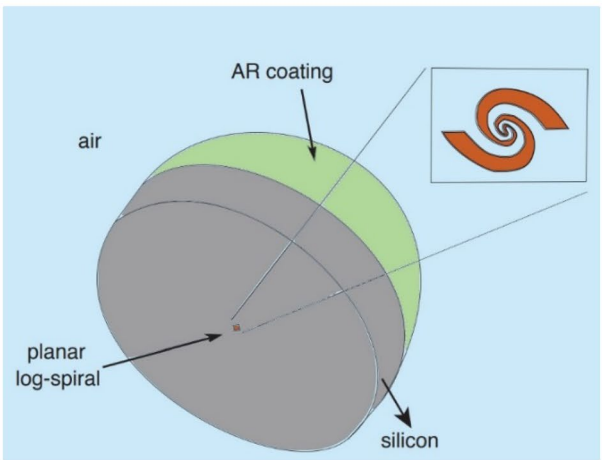

(c)

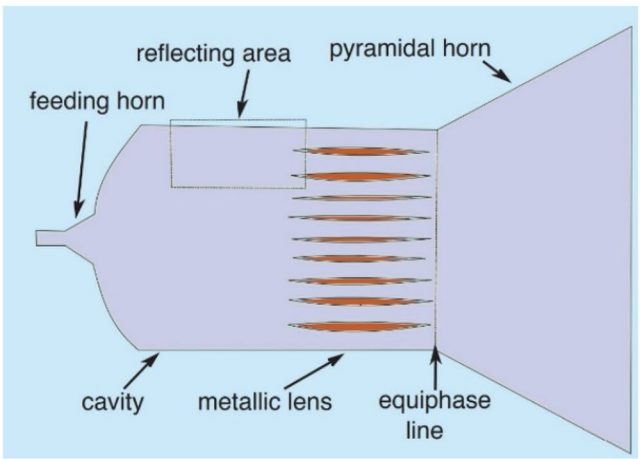

(d)

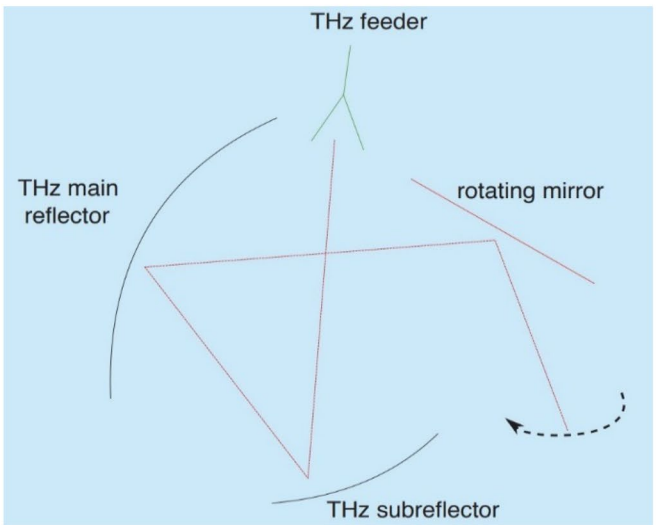

(e)

(f)

Fig. 15 **a**–**f** THz lens antennas [39–44]

Table 1 Performance comparison of different THz antennas

Ref	Type of the antenna	Applications	Frequency	Gain (dBi)	Directivity (dBi)	S_{11} (dB)	Substrate material
[11]	Dipole antenna with a reflector	High-speed wireless communication systems	0.3THz	5.14	5.74	–	Indium phosphide (InP) and benzocyclobutene (BCB)
	Dipole antenna with 3 directors			8.01	8.44	− 30	
	Dipole antenna with 5 directors			9.61	10.2	− 34	
	Array of 1 × 4 elements			13.6	14.1	− 37	
[13]	Microstrip patch antenna	Short-distance wireless communication	0.7–0.85 THz	3.497	6.038	− 40	RT/duriod 6006
[16]	Microstrip patch antenna	Wireless communication technology	0.65 THz	9.17	9.58	− 67.49	Photonic bandgap (PGB)
[19]	Offset dual-reflector antenna	Space communications, astronomy, and imaging systems	0.325–0.5 THz	32	–	− 30	–
[33]	Tunable THz dielectric resonator antenna	THz applications	4.088 THz	3.81	5.07	− 30	Silicon dioxide
	Tunable THz dielectric resonator antenna with graphene disk		4.104 THz	3.79		− 40	
[42]	Metallic lens antenna	Short-range communications	0.412 THz	27.6	–	− 35	–
[45]	Multilayered stacked patch antenna	Radar applications	0.3 THz	23	–	− 20	Quartz
[46]	On-chip slot antenna: circular shape	CMOS Technology	0.3 THz	5.30	7.05	− 20	Silicon
	On-chip slot antenna: diamond shape		0.3 THz	5.94	6.97	− 35	
[47]	Microstrip slot antenna	Wireless body area networks (WBAN)	0.852 THz	2.5	2.6	− 20	RT/duriod 6010
[48]	Microstrip antenna array	Medical application	0.1 THz 0.635 THz 0.835 THz	15.8 16.5 16.37	–	− 38 − 41.5 − 30.4	Liquid crystalline polymer (LCP)
[49]	Stacked Microstrip antenna	Bio-medical application	8.2 THz	6.48	6.33	− 38.85	FR-4

electromagnetic field scattering [58] if initial and boundary conditions are correct. It is guided by the scalar Helmholtz equation. An analytical solution is difficult to acquire due to the nonlinear nature of this equation. Fortunately, for the vast majority of practical issues, numerical answers are sufficient. With the help of Born approximation [59, 60], scalar Helmholtz equations become linear and can be solved in traditional ways. The objective was to convert complex data into two-dimensional (2D) or three-dimensional (3D) images. The direct method is to use linearized Helmholtz equations to generate an equation from samples from each channel. This is always an ill-posed problem, which is why regulation of the inverse problem is crucial for this form of processing. The image reconstruction techniques used in THz imaging are divided into two categories based on analytical reconstruction and iterative reconstruction. By using analytical reconstruction techniques, the issue of creating a picture and predicting the distribution can be solved mathematically directly. Iterative reconstruction approaches require a more difficult mathematical solution with multiple stages to produce images. Iterative reconstruction has drawn criticism for its computational overhead, which is claimed to be up to eight minutes for every iteration.

Back Projection Algorithm (BPA) and Range Migration Algorithm (RMA)

Synthetic aperture radar (SAR) imaging and focal plane imaging are the two most frequent working mechanisms for THz imaging. For digital focusing in SAR imaging, the two prominent algorithms used are back projection algorithm (BPA) and range migration algorithm (RMA). They implement calculations in the spatial domain and spatial frequency domain respectively. Because of the short wavelengths at THz frequencies, objects can be seen with extremely fine

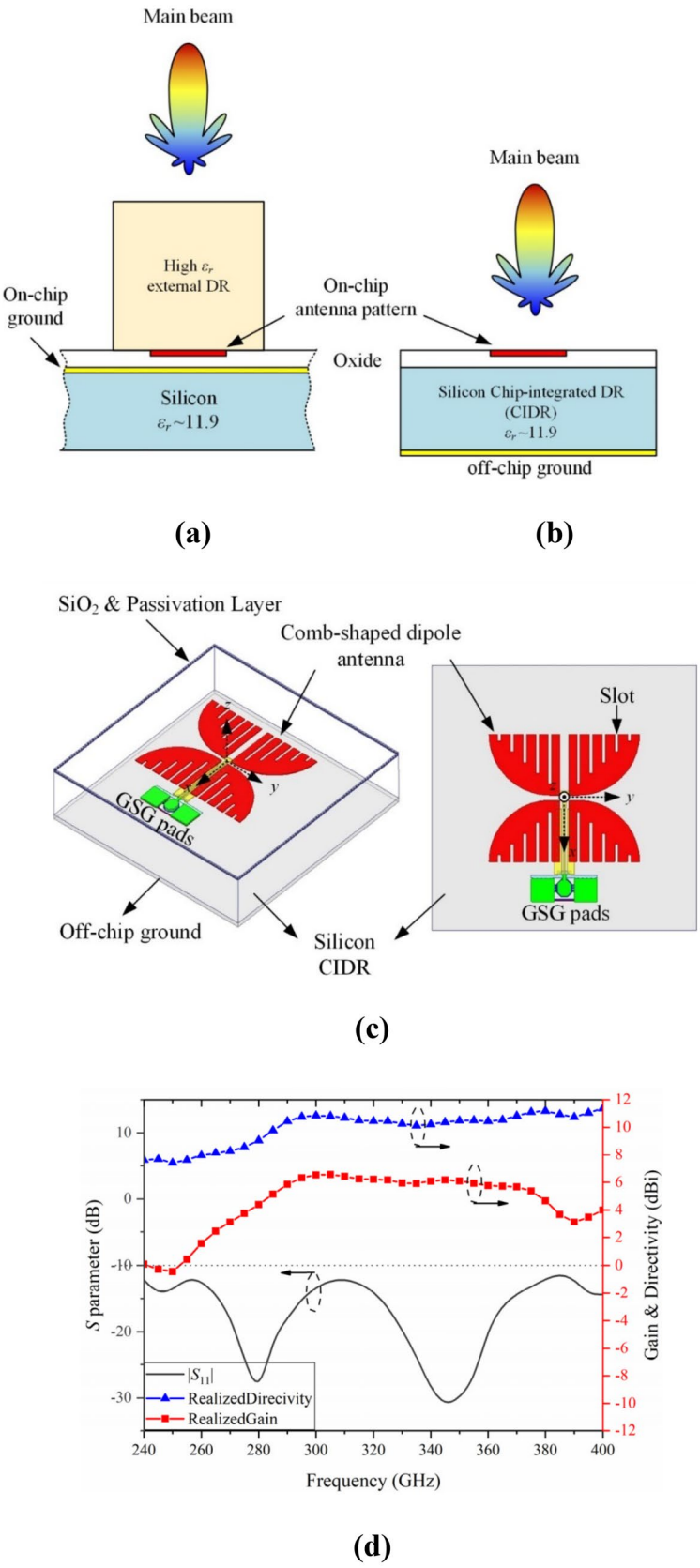

Fig. 16 **a** On-chip DRA. **b** On-chip antenna with silicon CIDR. **c** 3D view. **d** Directivity, gain and $|S_{11}|$ [54]

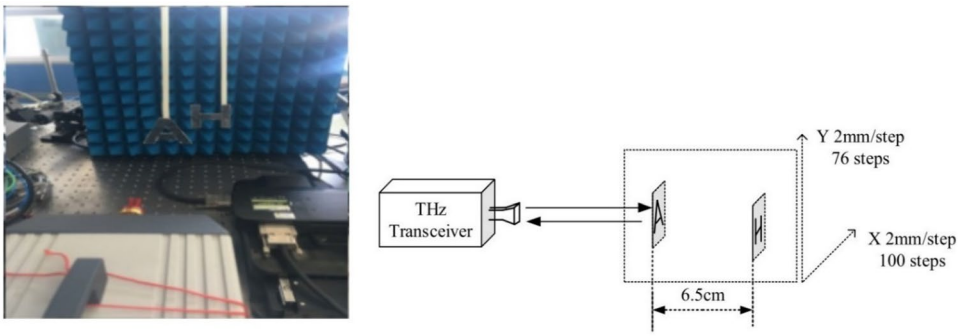

Fig. 17 THz near-field SAR imaging. **a** Experimental setup, **b** block diagram [61]

features. THz imaging, on the other hand, is not as advanced as microwave imaging. The near-field scenario can make a difference in determining whether we should merely duplicate earlier accomplishments at microwave frequencies. These two algorithms perform the same job, but in two different domains. In the study [61], BPA and RMA are compared in THz near-field imaging. Figure 17 depicts the facilities as well as the objects of interest. Metal foil is used to make the two letters A and H, which are separated by 6.5 cm. For data acquisition, frequency sweeping.

The raw results of experiments which are obtained are not visible due to diffraction. The letters' edges are a little blurry. Furthermore, there is a low contrast ratio between the background and the target. Two imaging methods are used to recreate the items in order to see the letters clearly. Figure 18 shows restored photos that are much clearer than those of the raw results, thanks to the use of BPA and RMA. Although both methods are capable of recovering the letters, RMA outperforms BPA. BPA has a greater depth of focus in comparison. Threshold processing and averaging techniques are used with matching results to help visualize the result more clearly. As a result, the targets contour is better defined, and the noise in the target-free area is effectively suppressed.

BPA and RMA can be used to create 3D images with a fine-range resolution. To see the data more clearly, point cloud processing is performed. To remove background noise

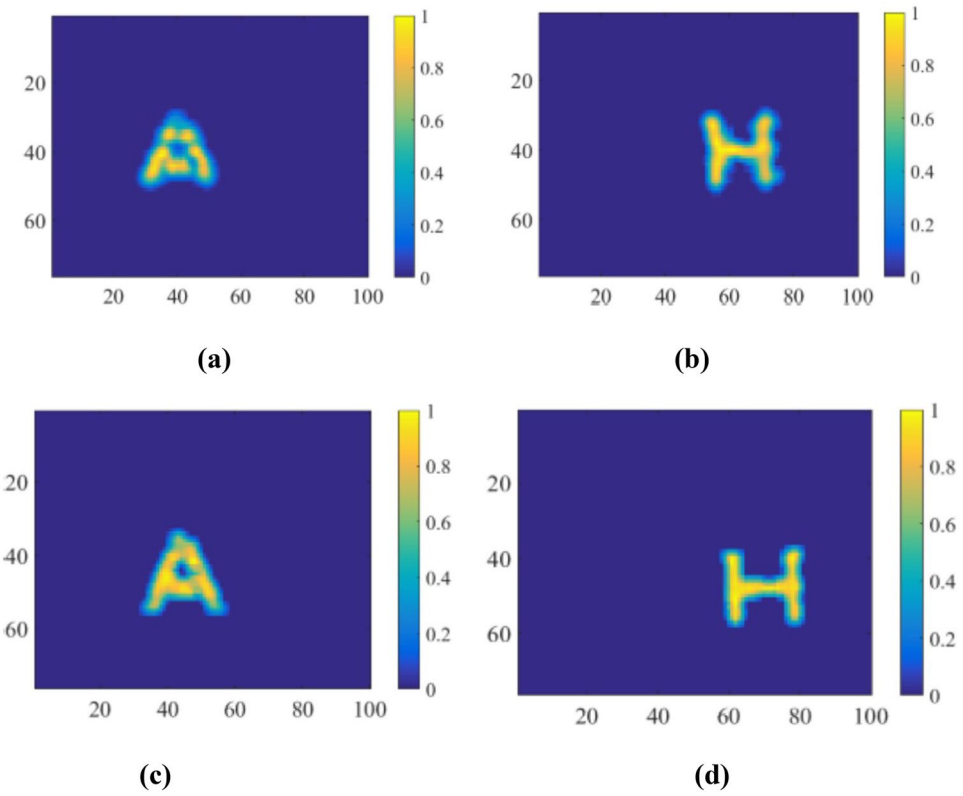

Fig. 18 2-D images **a** and **b** by bp and **c** and **d** by RMA [61]

from outside the target, threshold processing is performed. The bandwidth of the transceiver determines the range resolution of a SAR imaging system. Figure 19a shows a 3D image created using BPA, while Fig. 19b shows a 3D image created with RMA. BPA and RMA can be utilized to create fine-range resolution 3D pictures.

Phase Migration Algorithm (PMA)

The phase-shift migration algorithm (PMA) was created to address the shortcomings of the previous two algorithms. In comparison to RMA and BPA, PMA has a number of advantages. As per the experiments, positioning precision relative to RMA is quite exact and the ability to work without knowing the distance in advance is extremely useful. In the case of PMA, distance between the objective scene center and scanning array need not be known when the frequency sampling interval matches the scope requirement of the objective. In both mono-static and multi-static scenarios, the principle of the phase-shift migration algorithm (PMA) is deduced. In monostatic PMA, assume the antenna is located at (x, y, z_L), and the target's dispersion point is located at (x, y, z). The imaging task goal is to reconstruct the reflection coefficient of (x, y, z), which is written as $p\ (x, y, z)$. The antenna positions form a planar array in this case and it is always considered to be parallel to one of the coordinate planes, whose third coordinate component is z_L. Based on the assumptions made above, the system response (S) can be described using Eq. (5) as discussed in [62].

$$S\left(x',y',k\right)=\iiint_{x,y,z} p(x,y,z)e^{-j2k\sqrt{(x-x')^2+(y-y')^2+(z-z_L)^2}}dx\,dy\,dz \tag{5}$$

where k indicates the wavenumber of the signal used and X, Y, and Z span the domain to be imaged, which is represented by the dashed rectangular box in Fig. 20.

The entire method may be realized in the mono-static situation by following stages. To begin, the signals must be converted to the frequency domain. The echoes are frequently complex base band signals. Hilbert transformation needs to be used if only real signals are available. Then 2D-FT in both cross-range directions will be performed on Eq. (6). The system response must be calculated from Eq. (7) if the excitation source is not a Dirac delta function. The pulse compression along the range direction is realized by Eq. (8). Δk is an irrelevant factor in the process that can be ignored. Finally, 2D-FT and 2D-IFT will be realized by FFT.

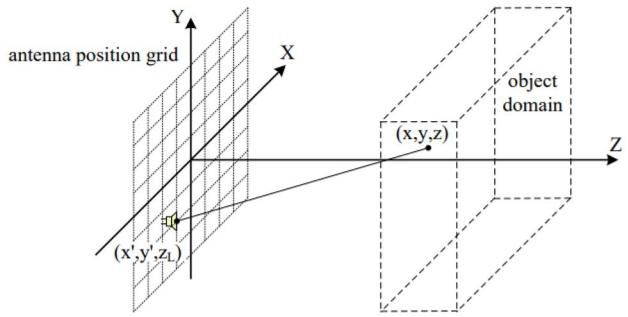

Fig. 20 Monostatic case in phase-shift migration algorithm (PMA) [63]

$$S\left(k_{x'},k_{y'},k\right)=\int_z P\left(k_{x'},k_{y'},z\right)e^{-jk_z(z-z_L)}dz \tag{6}$$

where $\mathrm{S}\left(\mathrm{k_{x'}},\ \mathrm{k_{y'}},\ \mathrm{k}\right)$ is 2D Fourier transformation (2D-FT) of $\mathrm{S}\left(\mathrm{x}'\ \mathrm{y}',\ \mathrm{k}\right)$ relative to the position variables x, y and $\mathrm{P}\left(\mathrm{k_{x'}},\mathrm{k_{y'}},\mathrm{z}\right)$ is the 2D-FT of p(x, y, z) relative to x and y. k_z is the wave number defined by $\mathrm{k_z}=\sqrt{4\mathrm{k}^2-\mathrm{k}_{\mathrm{x}'}^2-\mathrm{k}_{\mathrm{y}'}^2}$.

$$S\left(k_{x'},k_{y'},k\right)=\frac{E(k_{x'},k_{y'},k)}{o(k)} \tag{7}$$

wherein $\mathrm{E}\left(\mathrm{k_{x'}},\ \mathrm{k_{y'}},\ \mathrm{k}\right)$ refers to the received signal at the location (x', y') in wavenumber domain, and o(k) refers to the transmitted signal in the wavenumber domain.

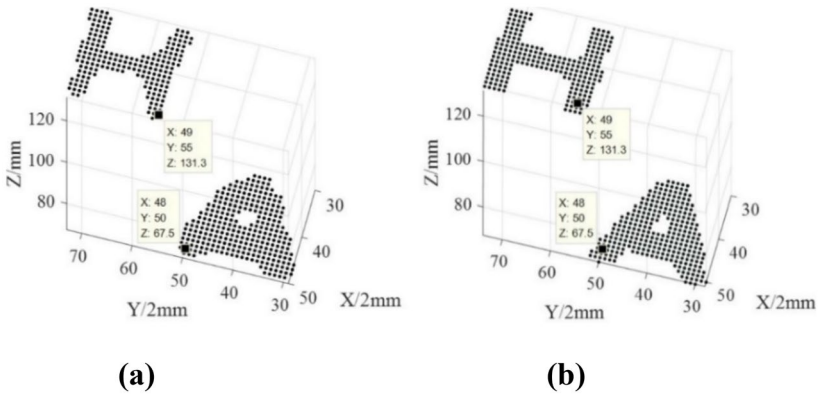

Fig. 19 3-D image of target, **a** BPA **b** RMA [61]

$$P(k_{x'}, k_{y'}, z) = \sum_{k_i} S(k_{x'}, k_{y'}, k_i) e^{j\sqrt{4k_i^2 - k_{x'}^2 - k_{y'}^2}(z - z_L)} \Delta k \quad (8)$$

where k_i is the sample in the wavenumber domain, Δk is the sample interval of wavenumber k. In [63], authors used two types of targets to reconstruct the images with PMA as illustrated in Fig. 21. The first is seven extremely small metal points that are positioned in a precise way to test the performance of positioning and focusing. The second is a metal fan with eight blades that examines the algorithm capacity to present things with complex shapes. Figure 21 shows the 3D pictures reconstructed, PMA is significantly faster than BPA while maintaining BPA's high precision, resulting in a compromise between BPA and RMA.

When MIMO technology is employed, the related scenario is referred to as the multistatic case. Figure 22 schematically depicts the array geometry, which is known as a plus array [64], as well as the experiment setup.

The responsiveness of the system in the multistatic case can be described by

$$S(x_t, y_t, x_r, y_r, k) = \iiint_{x,y,z} P(x, y, z) e^{-jk\sqrt{(x-x_t)^2+(y-y_t)^2+(z-z_t)^2}} e^{-jk\sqrt{(x-x_r)^2+(y-y_r)^2+(z-z_r)^2}} dxdydz \quad (9)$$

The objective to be imaged is the reflection coefficient function P(x, y, z), and the system response is a 5D matrix. In both monostatic and multistatic scenarios, the principle of phase-shift migration algorithm (PMA) is derived. In the multistatic scenario, the sample criteria and spatial resolution evaluation are obtained. The application and performance of PMA are confirmed by electromagnetic field simulation and experimental results (Fig. 23). In comparison to RMA and BPA, the advantages and disadvantages of PMA are stated as follows: (1) high positioning precision compared to RMA, as demonstrated in simulations and experiments, (2) the ability to operate without having a priori knowledge of the distance, (3) requires more calculation than RMA but can be done in parallel, (4) Must be used in a situation of equal-interval sampling.

Compressed Sensing (CS)

There was a shortage of room temperature high power sources that are required for THz imaging along with recording focal plane arrays. Compressed imaging with a single pixel camera can be used to solve this problem [65]. The idea behind compressed imaging was to reconstruct a picture using low-dimensional detection and then solve the ill-posed inversion using computational procedures. Figure 24 shows the compressed sensing (CS) method for achieving THz single-pixel imaging technology for improving measurement efficiency [66]. It recovers a high-quality THz image with a lesser number of measurements than the total number of image pixels. Furthermore, the use of photo-induced semiconductor carriers is critical for improving the CS technique's practicability [67]. It enables quick sampling of the THz wavefront and allows for the measurement mask to be changed voluntarily. Compressed sensing will be able to extract both the amplitude and phase information of a THz field at a time. The measuring masks are usually placed close to the sample to reduce the diffraction impact [67, 68]. CS recovers THz temporal images and the Fourier transformation, and IFD techniques are used to rebuild a sharp THz spectrum image.

Metals in the shapes of "T," "H," and "Z" are selected as the samples as shown in Fig. 25a. From Fig. 25b, due to diffraction, the image quality of the reconstructed image of three letters at the peak position is very poor. By utilizing Eq. (10), the reconstructed images are obtained, as shown in Fig. 26d.

$$U(x_1, y_1) = -\frac{e^{-jkd}}{j\lambda d} \iint_{\infty} U(x_0, y_0) exp\left\{-j\frac{k}{2d}\left[(x_0 - x_1)^2 + (y_0 - y_1)^2\right]\right\} dx_0 dy_0 \quad (10)$$

where $U(x_0,y_0)$ is the THz spectral image contaminated by the diffraction, (x_0,y_0) and (x_1,y_1) are the spatial coordinates on the sampling ad reconstruction planes. k is the wave number of the THz field in a vacuum and λ is the wavelength. By using Fourier transformation, it is clear to see how the THz field's diffraction phenomenon is greatly lessened and the quality of the image is significantly improved.

Reconstructing High-Resolution (HR) Image

CT (computed tomography) is a type of imaging that creates tomographic (cross-sectional) pictures by combining numerous transmission measurements from various angles. The most common methods for probing the sample are X-ray and ultrasound. Existing THz CT techniques frequently depends on continuous wave (CW) source and detector technologies because of their high output power. However, major drawback of CW systems is its low operating frequency, which results in low diffraction restricted resolution below several hundred GHz. Continuous wave (CW) and pulsed sources use methods that were established for X-ray CT to reconstruct cross-sectional images. These are primarily based on the Radon imaging model [70], which does not account for physical factors such as scattering, diffraction, and refraction in electromagnetic wave propagation. Image reconstruction

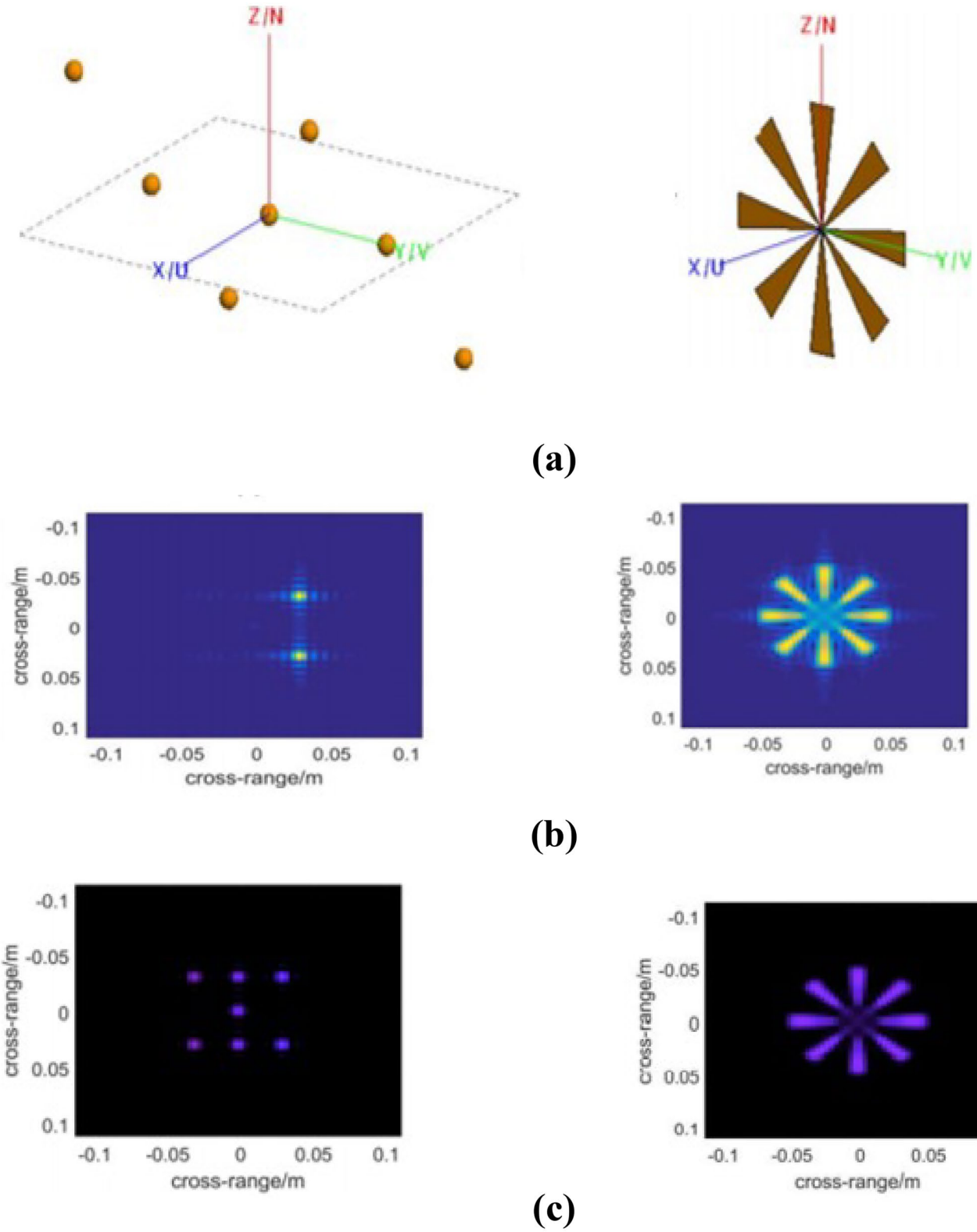

Fig. 21 PMA simulation result in monostatic case: **a** targets: seven metal points and metal fan, **b** slice figures, **c** 3-D reflectivity figures [63]

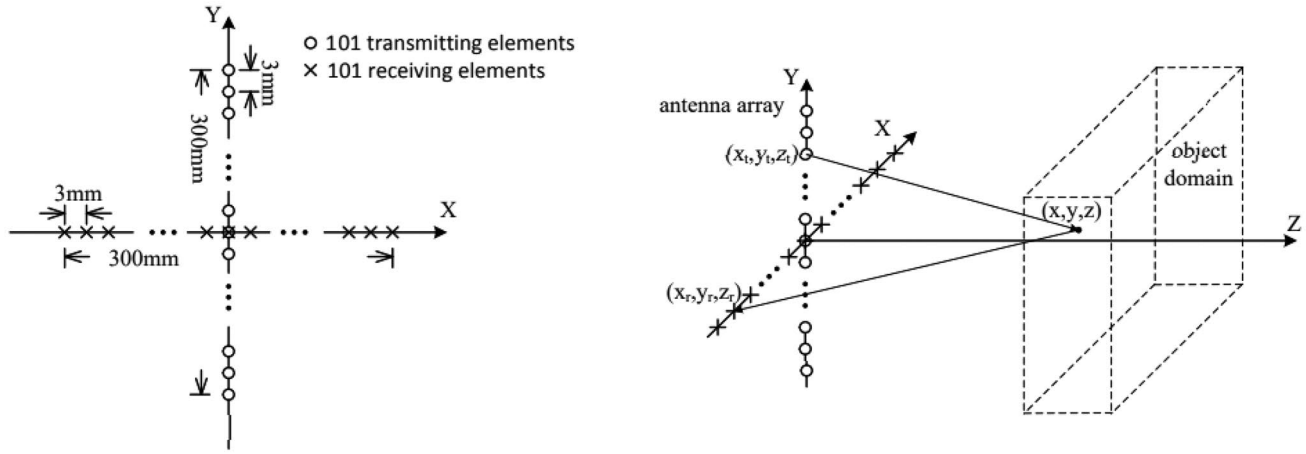

Fig. 22 Multistatic case in phase-shift migration algorithm (PMA) [63]

has been reported to be improved using broadly valid imaging models such as Snell's law of refraction or Helmholtz's equation. However, this comes at the expense of requiring prior knowledge of the sample shape and/or a large increase in processing effort. Two types of algorithms include reconstructing an HR THz image from multiframe low resolution (LR) images and from an LR-degraded THz image. In [69], authors examined various strategies for reconstructing high-resolution (HR) THz pictures. Figure 26 depicts the observation model of HR reconstruction.

The continuous scene is considered to be band-limited and is appropriately sampled at or above the Nyquist rate in order to rebuild an HR image from numerous LR images. The outcome is an HR image, represented by the letter x, that is free of distortion and noise. An LR image, indicated as y_k, is created by warping, blurring, down sampling, and adding noise to an HR image. M, B, D, and n, respectively, are the matrix operators that represent each process. Equation (11) expresses the observation model [71] that describes the link between the HR picture x and the kth LR image:

$$y_k = DB_kM_kx + n_k \tag{11}$$

This is a simple observation model that ignores the combined effect of many spoiling processes. The final goal is to figure out how to merge fresh information from distinct LR images to rebuild an HR image. As a result, HR reconstruction from multiple LR images is an inverse problem of the observation model, i.e., finding the best solution for x from y_k, $1 \le k \le p$. Figure 27 depicts the basic workflow for implementing HR reconstruction. Registration, interpolation, and deblurring [71–73] are the three processes that make up the entire process. To get the optimum effect, these three stages are usually iterated.

The projection onto convex sets (POCS) algorithm is a method for determining the best solution that meets the constraints which can be expressed as a series of convex sets. But it has a poor convergence speed and low algorithm efficiency [74]. The mean square error (MSE) reduces as the number of iterations increases, but the blurring effect worsens. The HR image is estimated using the iterative back

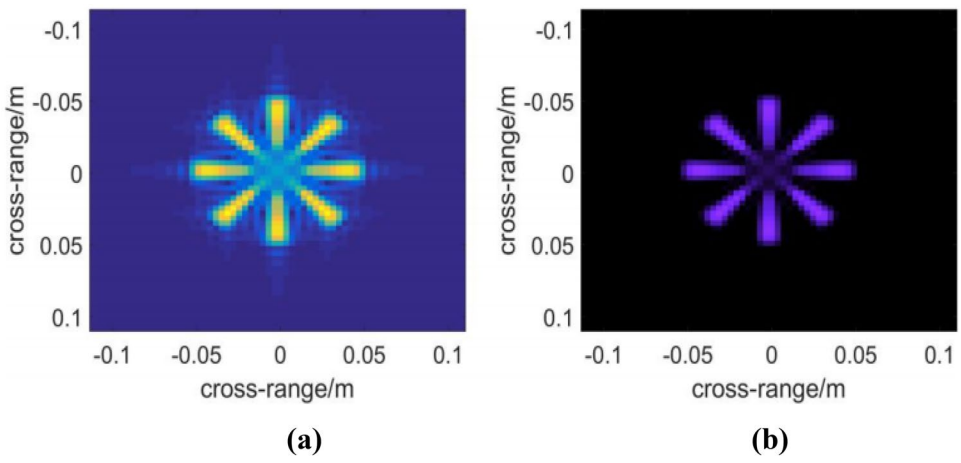

Fig. 23 PMA simulation result in multistatic case **a** slice figure, **b** 3D reflectivity figure [63]

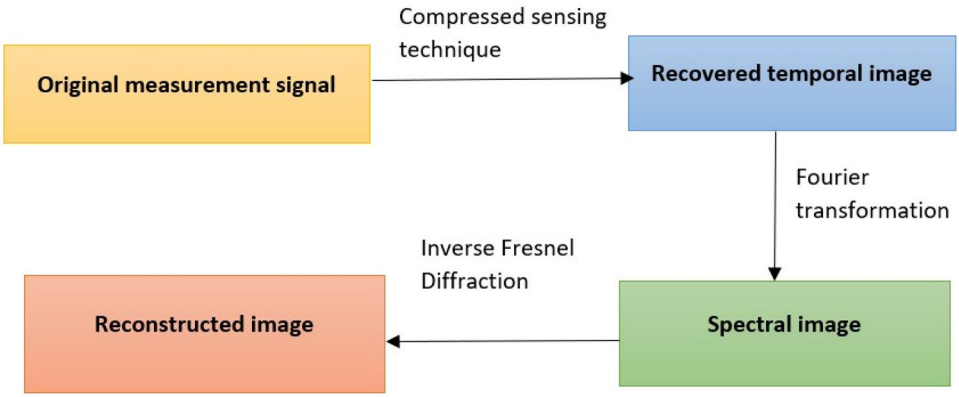

Fig. 24 Image reconstruction scheme using compressed sensing (CS) technique [66]

projection (IBP) method by back projecting the error (difference) between the calculated LR pictures via image blur and the observed LR images. The ideal solution to the HR image matrix $x[n_1,n_2]$ is obtained by repeating this method iteratively to reduce the energy of error. When the largest difference of the elements between $x^{n+1}[n_1,n_2]$ and $x^n[n_1,n_2]$ is smaller than a particular threshold, the iteration process can be stopped. The IBP iteration process can be expressed as

$$\hat{x}^{n+1}\left[n_1,n_2\right]=\hat{x}^n\left[n_1,n_2\right]+\sum\nolimits_{m_1,m_2\epsilon y_k^{m_1,n_1}}(\hat{y}_k\left[m_1,m_2\right]-\hat{y}_k^n\left[m_1,m_2\right])Xh^{BP}[m_1,m_2:n_1,n_2] \tag{12}$$

where $\hat{y}_k^n=W_k\hat{x}^n$ are the calculated LR images from the approximation of x^n after n iterations, $\gamma_k^{m_1,n_1}$ represents the set $\{m_1,m_2\epsilon y_k|m_1,m_2 \text{isinfluenced by } n_1,n_2 \text{ where } n_1,n_2\epsilon x^n\}$ and h^{BP} is the back projection kernel that controls the contributions of error $(\hat{y}_k\left[m_1,m_2\right]-\hat{y}_k^n\left[m_1,m_2\right]$ to $\hat{x}^n[n_1,n_2]$. The matrix W_k represents the blurring and deterioration effects that relate to the calculated HR image $\hat{x}$ and LR images $\hat{y}_k$. With only the averaging effect taken into consideration, the matrix W_k is chosen to be the PSF, which contains only the averaging operator. The choice of the back projection kernel (h^{BP}) affects the characteristics of the optimal solution. When a priori knowledge of image noise is unknown, the Lucy–Richardson (L-R) HR Algorithm performs well, and in many cases, the gray-level distribution can be approximated by a Poisson field [75]. When THz waves scan imaging targets, the THz energy on each pixel can be seen as the transient time-scale interaction of several THz photons with the imaging dot, and each pixel is independent. As a result, a Poisson field might be used to approximate the gray-level distribution of the THz image. The L-R iteration can be expressed as follows:

$$\hat{f}_{k+1}(x,y)=\hat{f}_k(x,y)\left[h(-x,-y)*\frac{g(x,y)}{h(x,y)*\hat{f}_k(x,y)}\right] \tag{13}$$

where $\hat{f}$ is the estimated value of the degraded image, g is the degraded image, and h is the PSF. The horizontal direction is represented by the coordinate x, and the positive direction is right, whereas the vertical direction is represented by the coordinate y, and the positive way is upward. While restoring the edges, L-R algorithm will produce low-frequency noise. To suppress this noise, the number of iterations needs to be increased. The pixel weight control can preserve the texture and edges while enhancing the imaging target-background contrast. The wavelet decomposition reconstruction approach is another high-resolution (HR) THz picture reconstruction methodology. The first step is to interpolate the LR THz image. Then, using 2D wavelet decomposition, the interpolated LR THz image is processed. Select the first layer wavelet coefficients for reconstruction (bi-orthogonal wavelet bases are used here) and finally, obtain the HR image. The abovementioned HR reconstruction technique is schematically depicted in Fig. 28. In the HR rebuilt image, there is a clear improvement in resolution. To improve contrast, the false-color image is created using the grayscale as illustrated.

Angular Spectrum Method

In order to recreate an image from a hologram, digital holography (DH) uses the angular spectrum approach as its core component. With this method, the hologram can be accessed and altered digitally in its spatial frequency domain. Any wave field can be divided into individual plane waves flowing in various directions. The angular spectrum approach [80] takes advantage of this property. These plane waves combine to form an intricate wave field, like a hologram.

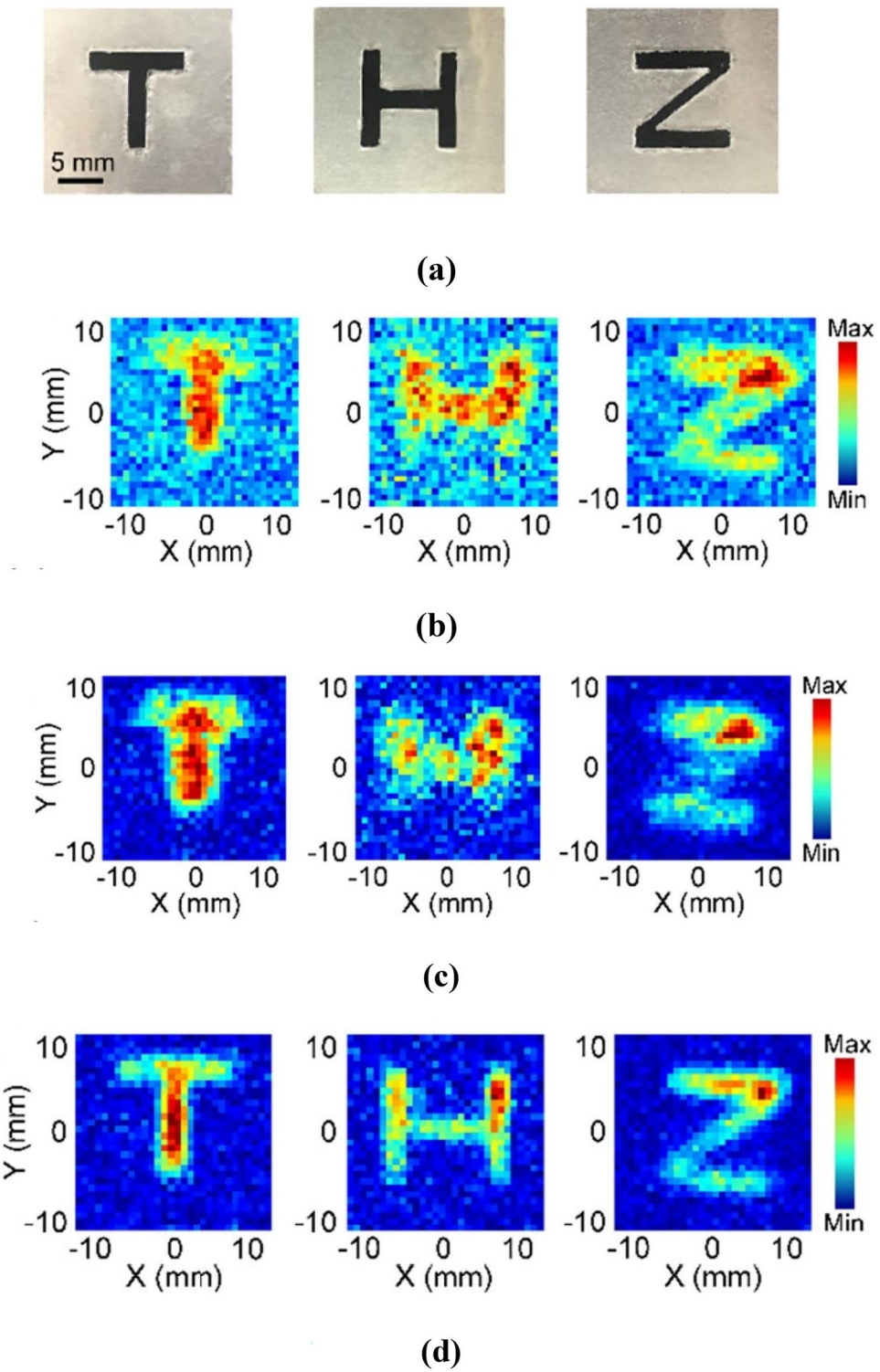

Fig. 25 **a** Pictures of the metals in the shape of T, H, and Z, **b** temporal image, **c** spectral images, **d** reconstructed THz image [66]

The complex wave field at any other location in space can be recovered by digitally propagating the individual plane waves after breakdown into their component parts.

Given that the objects are often larger than the millimeter-scale wavelengths and the interferometer is meter-sized, the majority of TDH occurs just within the Fresnel diffraction region specified by Equation.

$$N_F = \frac{(2a)^2}{\lambda d} \tag{14}$$

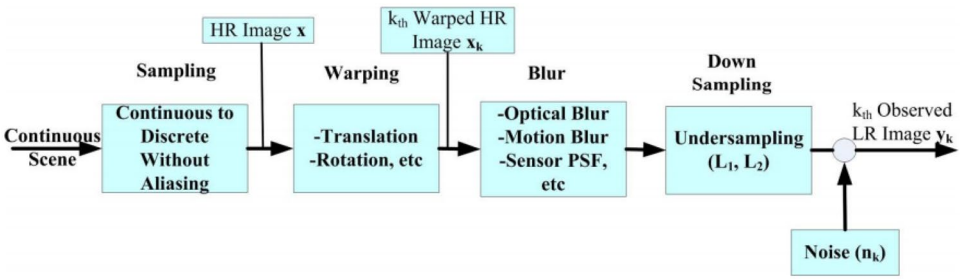

Fig. 26 Observation model for reconstructing HR image [69]

where N_F is the dimensionless Fresnel number of an optical component, a is the aperture (or object) radius, d is the path length and λ is the wavelength. An advantage of the Fresnel approximation is the fact that only one Fourier transform is required. But, because the Fresnel reconstruction method does not allow for digital filtering as part of the reconstruction process, it cannot take advantage of one of the major attributes of digital holography (DH). Furthermore, the second Fourier transform required for the angular spectrum method is easy to perform on a computer.

Ptychographic Iterative Engine (PIE)

The fundamental method of ptychography involves scanning an item across an illumination function at overlapping places and gathering a collection of diffraction patterns, often known as ptychograms [81]. It achieved its breakthrough by combining the ptychographic idea with iterative phase retrieval techniques used in coherent diffraction imaging (CDI) [82, 83], giving rise to what is known as ptychographic iterative engines (PIE). A schematic of ptychography in the transmission is shown in Fig. 29.

PIE analyzes the diffraction patterns that were captured from an object that was irradiated by a largely localized, movable wave field. Traditional iterative techniques struggle to handle complex (phase and modulus) or soft (bandwidth-limited) illuminating functions. Extended ptychographic iterative engines (ePIE) [84] were developed by permitting simultaneous reconstruction of the probe beam which provides significant advancements in PIE's convergence and robustness. Thereafter, by modifying the update functions and appropriating the momentum concept from the machine learning community. Recently, it has been demonstrated that optimizers that use automatic differentiation (AD) [85] can also be used to recover the object when solving the phase problem in ptychography instead of PIE-related techniques. Axial multi-image phase retrieval is a coherent diffractive imaging method that reconstructs the entire object wave field using a variety of diffraction patterns based on axial movement diversity.

Table 2 discusses different THz image reconstruction algorithms and applications. The back projection algorithm (BPA) and range migration algorithm (RMA) are two popular methods in SAR imaging. Early imaging algorithms relied heavily on monostatic SAR. Later, as bistatic SAR systems became available, numerous monostatic-based methods were adapted and made an extension to bistatic SAR imaging. For imaging applications with complex bistatic data, a traditional back-projection algorithm (BPA) based on phase-compensated and coherent summations in the time/space domain is a typical technology, although it has a high computational cost. A modified range Doppler technique for bistatic SAR focusing was described based on a Taylor series expansion. The aforementioned strategies cannot be immediately applied to the MIMO imaging process since the MIMO system differs from the SAR system in terms of data gathering. However, it is important to note that the development of the MIMO imaging technique has considerably benefited from bistatic SAR. MIMO-based developed algorithms are best suitable for THz imaging in a complex environment. On the other hand, THz ptychography is the trending lensless imaging technique based on ptychography iterative engine (PIE) algorithms.

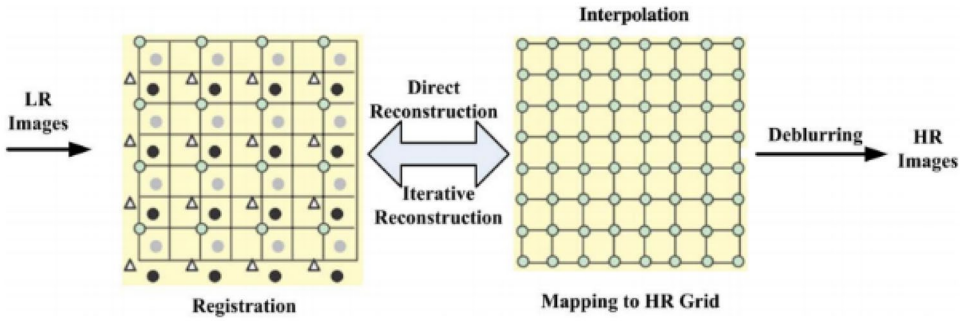

Fig. 27 Basic reconstruction flow [69]

Table 2 THz image reconstruction algorithms and applications

Ref	Reconstruction algorithm	Applications	Features	Merits	Demerits
[61, 63]	Back Projection Algorithm (BPA)	➔ Remote sensing ➔ X-ray imaging	➔ Analytical Reconstruction algorithm ➔ Time-domain Algorithm ➔ By integrating echoes at different frequencies, BPA reconstructs the image of the object	➔ Simple ➔ High computational efficiency and ➔ Robust	➔ Unacceptably high computational resource usage ➔ Too slow to use in a real-time system
	Range Migration Algorithm (RMA)	➔ SAR Imaging	➔ Frequency-domain algorithm ➔ To find Fourier transform numerically, Stolt interpolation and approximations are used	➔ Better performance with respect to cross range resolution ➔ RMA performs better in terms of filtering for out-of-focus objects	➔ Interpolation errors are inevitable and result in range direction defocusing
[63]	Phase-shift Migration Algorithm (PMA)	➔ THz imaging reconstruction	➔ Combines the features of BPA, RMA and RDA algorithms	➔ Performs significantly more quickly than BPA ➔ Reconstruct images with high precision	➔ More computation intensive ➔ PMA should be used in the case of equal-interval sampling only
[65]	Compressed Sensing (CS) Algorithm	➔ Single-pixel THz imaging ➔ Radar reconstruction ➔ Radar remote sensing	➔ Uses a continuous-wave THz source	➔ Eliminates the requirement for THz beam or object raster scanning ➔ Speeds up the acquisition process	➔ Data processing time is more ➔ Presents poor image sharpness
[66]	Inverse Fresnel Diffraction (IFD) Algorithm	➔ Single—pixel THz imaging	➔ To improve the image quality, CS recovers THz images using the IFD technique	➔ Removes the impact of the diffraction ➔ Capable of recreating a precise THz spectrum picture	➔ Successful reconstructions can only be obtained when the small-angle number, a derived quantity, is much less than one
[70]	Phase-contrast THz-CT Algorithm	➔ THz computed tomography (THz CT)	➔ Fast THz time-domain spectrometer ➔ Uses different image reconstruction approaches, cross-sectional images are reconstructed from sinograms	➔ Efficient ➔ Robustness ➔ Accuracy	➔ Low operation frequency, less than a few hundred GHz ➔ Resolution is low due to diffraction limitations
[76]	Multi Input Multi Output- Phase Shift Migration (MIMO-PSM) Algorithm	➔ THz MIMO 2D Imaging	➔ Spatial -frequency domain ➔ Implemented the PSM into MIMO reconstruction ➔ Elicited from the explosion reflection model	➔ Highly efficient ➔ Fast imaging algorithm for MIMO imaging ➔ Reconstruction of a high-quality image is possible	➔ Absence of zero padding operation ➔ Not suitable for 3D imaging
[77]	Multi Input Multi Output- Side Looking- Enhanced Phase Shift Migration (MIMO-SL-EPSM) Algorithm	➔ THz MIMO 2D Imaging	➔ Spatial -frequency domain ➔ Derived and applied the modified phase shift factor in the transmitting array ➔ Necessary phase compensation, zero-padding is also added	➔ Fast wavenumber domain transformation ➔ Used to transmitting array systems that use randomness in their distribution	➔ Hardware constraints ➔ There are restrictions on the maximum amount of transmitting and receiving channels

Table 2 (continued)

Ref	Reconstruction algorithm	Applications	Features	Merits	Demerits
[78]	Phase Shift Migration with Modified Coherent Factor Algorithm	➔ MIMO-SAR 3D Imaging	➔ Creates a synthetic echo describing the difference wavenumber ➔ It is suggested to calculate incoherent power using wavenumber domain	➔ Provides very efficient computation ➔ Floating-point operations (FLOPs) index is low	➔ Coherent summations in spatial domain suffer from huge computational cost
[79]	Super-resolution imaging method	➔ Analyzing agricultural product THz imaging ➔ Useful for diverse biological product analysis	➔ With the use of a neural network, this technique embeds a graph for local pixels in low-resolution ➔ A sizable collection of THz images is not necessary for the model's training	➔ Performs super resolution ability beyond hardware limitations	➔ The rate of resolution enhancement is constant ➔ Imaging acquisition speed is still slower

Application Specifics of THz Imaging

THz radiation has several notable characteristics like its low energy and non-ionizing nature for non-destructive testing. Hence, it is applicable in a variety of disciplines including medical diagnostics, drug detection, security screening, and material property analysis. Foreign body detection, chemical residue detection, and moisture content are all possible with THz time-domain spectroscopy (TDS). As a result, it can be used to monitor and control food processing [86–90]. Trees and plants can have their leaf water dynamics measured using a TDS device [91]. THz spectroscopy has also been used to analyze several pesticide compounds [92–95]. In recent years, reflection mode THz pulsed spectroscopy (TPS) has shown potential in detecting cancerous tissue [96, 97], as shown in Fig. 30. This technique demonstrates clear separation of malignant and healthy tissues in all recently removed tissues and cell types.

THz Spectroscopy Applications in Cell Detection

Early diagnosis of any disease requires accurate and quick detection. Flow cytometry, fluorescent molecular tomography, and multiphoton microscopy are examples of cell detection approaches that rely heavily on labeling technology. They have excellent precision, sensitivity, and selectivity. However, these technologies unavoidably involve chemical or biological tagging. THz spectroscopy with high resolution is evolving into a reagent-free, label-free, non-invasive, and optical approach for the detection and identification of living cells, thanks to new instruments.

Tissue THz Spectroscopy

Because of the increased interest in developing THz technology, THz spectroscopy may now be used to identify and distinguish healthy, dehydrated, burned, and sick tissues. THz spectroscopy allows time-resolved analysis of these dynamic processes. It is the process of determining phase and amplitude data, which are related to tissue absorption coefficient and index of refraction. Because of these characteristics, THz spectroscopy has the ability to detect tissue. Fresh tissue, like skin tissues (− 70% by volume), contains a large amount of water, which exhibits significant absorption at THz frequencies ($u_a = 300\ cm^{-1}$, at 1.5 THz). Other tissue preparation methods which include paraffin, frozen and formalin-fixed tissues have been developed to remove the effects of significant optical absorption of water. Cancer patients' paraffin-embedded tissues appeared to have greater refractive index and absorption coefficients than healthy tissues recently. Additionally, snap-frozen tissues were regularly evaluated to limit the influence of water, and

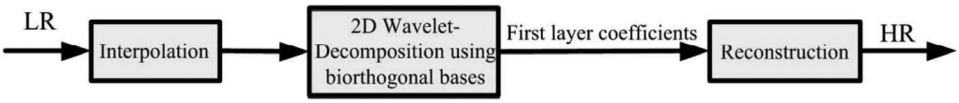

Fig. 28 Schematic flow of wavelet decomposition reconstruction approach [69]

several studies demonstrated that Alzheimer's patients' tissues absorbed less water than normal tissues. In the same manner, because water's significant optical absorption causes just a few millimeters of penetration in biological tissues, THz in vivo spectroscopy applications are currently limited to the surface of biological tissues. Meanwhile, the ability to absorb a lot of water is useful since it allows for a delicate form of soft-tissue contrast. Different skin tissues have significantly variable refractive indexes and absorption coefficients.

THz Spectroscopy of Cancer Cells

THz spectroscopy can recognize cancer cells based on signal properties, real-time observation of minute structural changes, and study of intracellular water dynamics. The complete procedure is quick, real-time, non-invasive, and label-free. It could result in the creation of an innovative clinical analysis tool. Three THz images are generated for each fresh tissue sample: a fresh image, an FFPE image, and a pathology image, as illustrated in Fig. 31. In [98], authors summarize the procedure. In core THz system imaging, tissues are positioned on polystyrene slides for transmission or polystyrene panes for reflection [99, 100]. THz measurements are carried out by scanning the sample and calculating the signal emitted or reflected at each place in relation to a reference. To correct for any phase shifts, it's critical to normalize the observed signal with a well-chosen reference [99]. Then the THz image can be created by measuring each location's temporal domain peak or single frequency magnitude [101], deconvolution of reference signal [102], integration of frequency domain spectral power [98, 102–104], or using statistical signal processing for cancer classification [102, 103].

According to recent research developments with respect to the advancement of near-field imaging technologies, THz imaging resolution is improving [105]. Figure 32 displays frequency domain photographs of an infiltrating ductal carcinoma at 1 THz, showing reduced transmission and increased reflection in malignant areas compared to surrounding normal fibrous and fatty tissue parts. Many additional researches have made similar findings. The observed disparity was explained by the increased THz vibration absorption, reflection, or refractive index that was caused by the presence of more water in malignant areas.

Imaging devices must be small and simple to use in order to be used in fast cancer screening during surgery. A notable example of such a system is the handheld THz pulsed imaging (TPI) system, which is represented schematically in Fig. 33 [106]. The quartz tip scans a 15×2 mm area in this TPI device and measurements are gathered in 26 pixels. The accuracy of this technique in identifying malignant regions was 75%. However, this ex-vivo examination has the problem that the material must be divided into pieces of uniform thickness (usually on

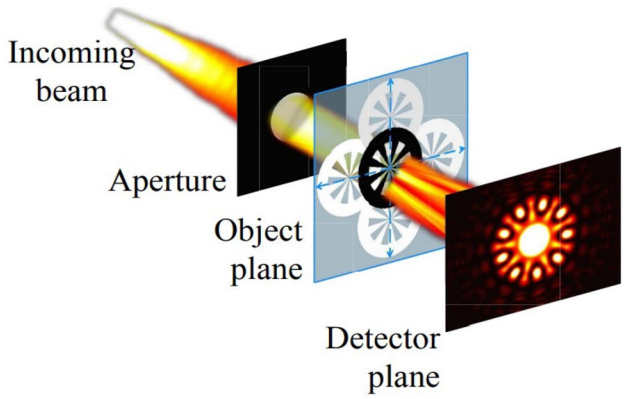

Fig. 29 Transmission ptychography [81]

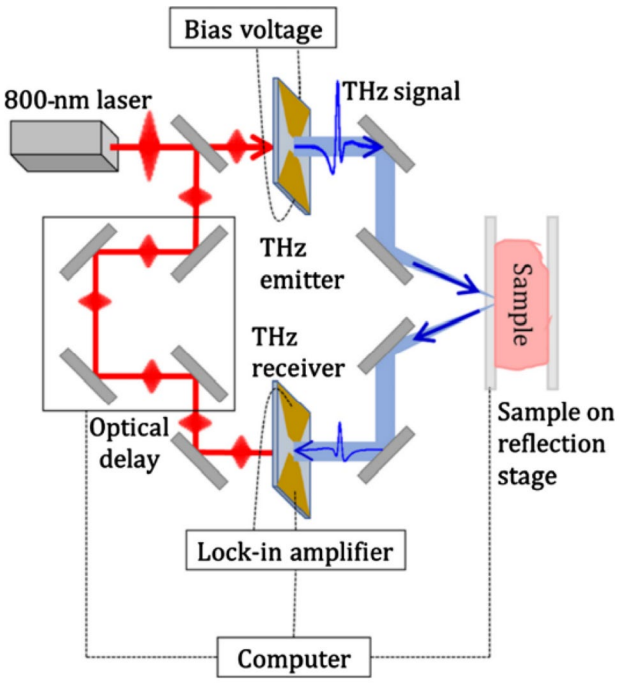

Fig. 30 Cancer detection in excised breast tumor using THz imaging system [96]

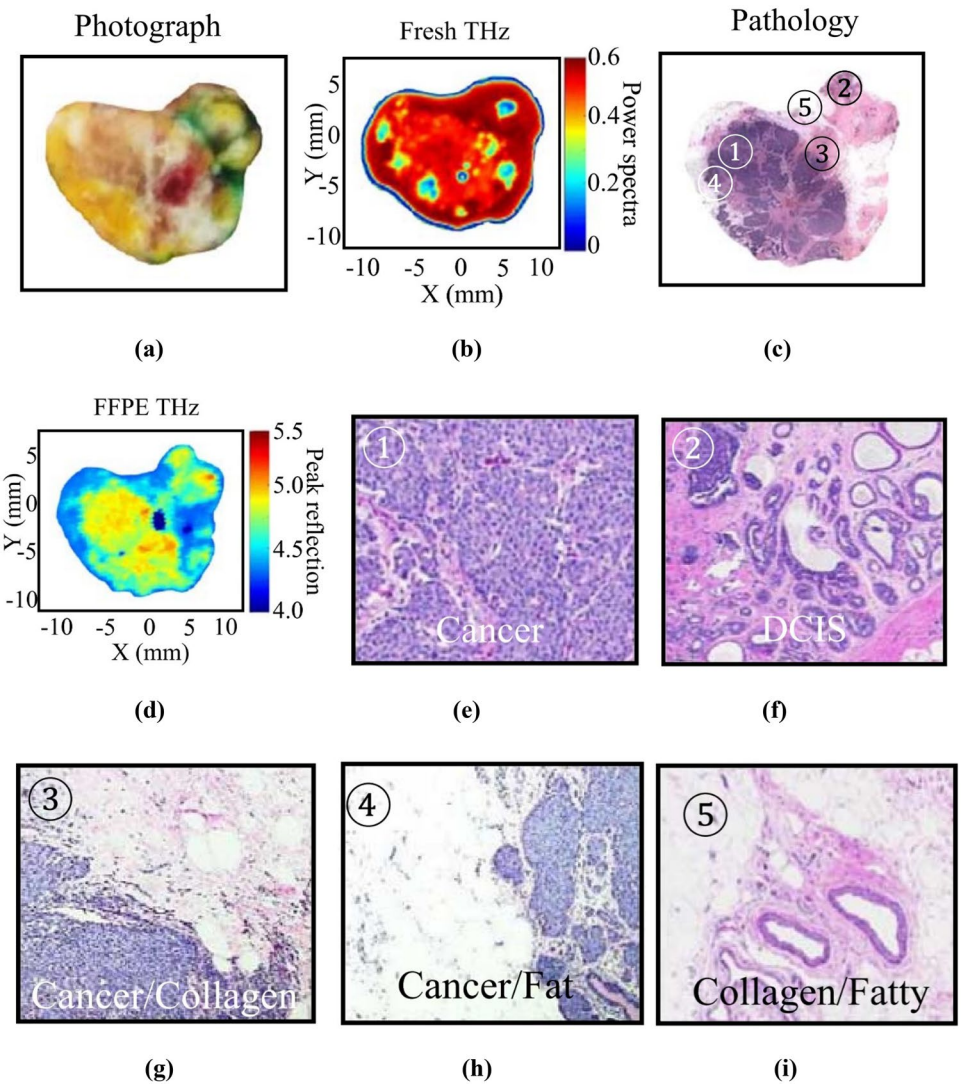

Fig. 31 Human breast cancer tissue captured in THz images [96]

the scale of micrometers) in order for THz waves to pass through. The human body is made up of several different components, including a significant amount of water, which prevents THz waves from penetrating it deeply. Because of this, most studies use ex-vivo tissue imaging, while very few do so with in-vivo tissue imaging. A 2.52 THz continuous wave was used to obtain images of brain gliomas with a resolution of 200 μm [107, 108]. Currently, in vivo THz imaging research is in its infancy. Two key difficulties remain in human body research. The first one is, compared to mouse tissue; human tissue includes substantially more types of components, complicating spectral analysis. The second is that variations in tissue composition between individuals will affect THz wave absorption and refraction differently. These two problems make it difficult to accurately identify malignant regions. THz pictures of cancer tissue are now mostly created using variations in the water content of normal and malignant tissue.

THz radiation has an ability to penetrate only a few hundred micrometers in human skin [109]. Several organizations have suggested freezing ways to increase the depth of THz radiation penetration into wet tissues since the absorption coefficient of ice is lower than that of liquid water [110, 111]. THz radiation can therefore travel farther into the tissue when the water molecules are frozen. They were able to discriminate between benign and malignant tissue slices using the freezing method, which is challenging to do in fresh situations. The same team was able to identify lymphatic metastases that were difficult to see in the fresh form by freezing the lymph node. Brain tissue samples afflicted by Alzheimer's disease are characterized using a freezing process. Up to a few millimeters below the surface, visual imaging and MR imaging function poorly [109] and are unable to identify the precise boundary below the skin's surface. The general clinical picture, as depicted in Fig. 34, does not adequately detect the cancer spread beneath the skin

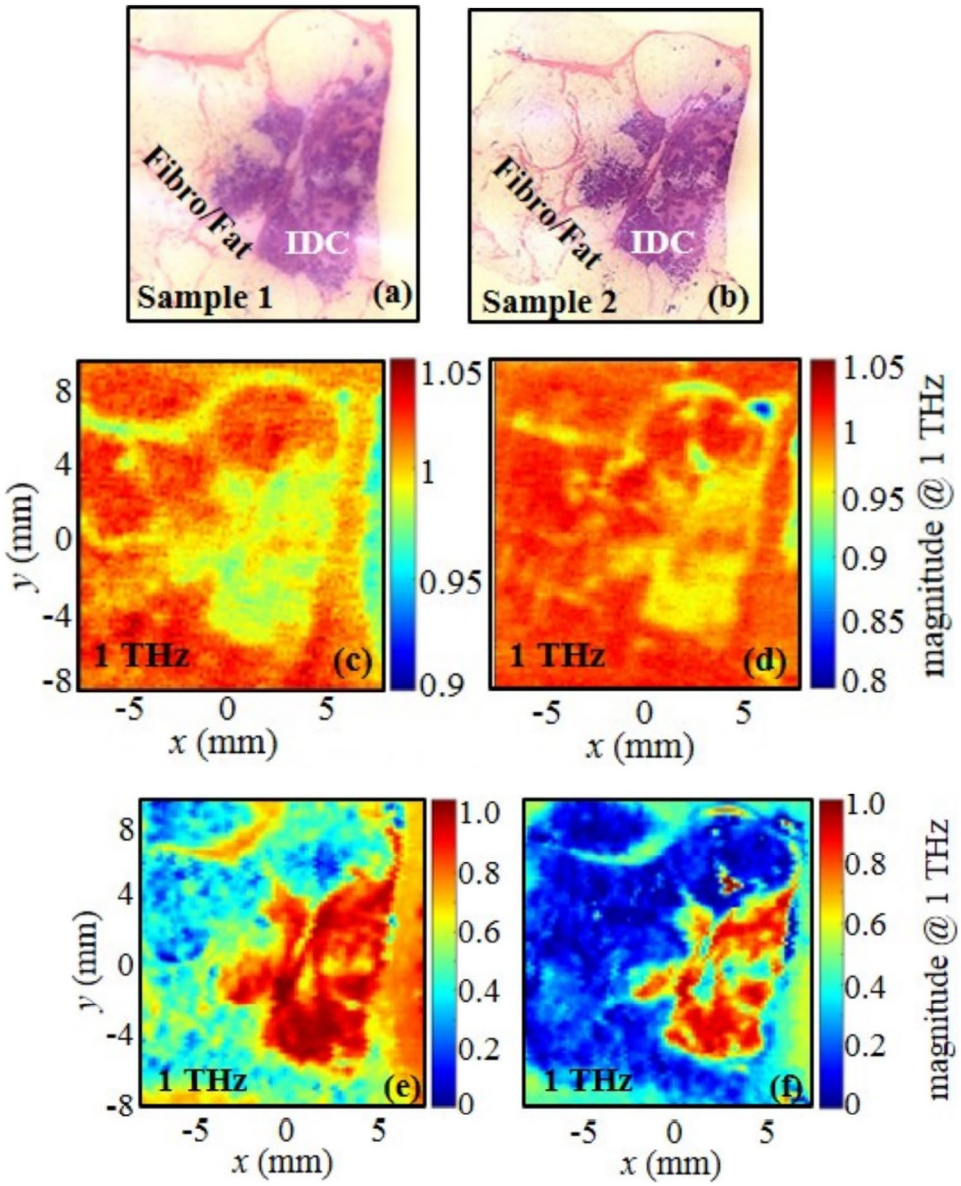

Fig. 32 Pictures of infiltrating ductal carcinoma. **a** and **b** The pathology for samples 1 and 2, respectively, **c** and **d** are the transmitted-magnitude pictures, **e** and **f** are the photos of the magnitude of reflection [99]

surface. The THz images reveal the depth of the cancer invasion into the skin which was 250 μm in this case [112]. The medical professional can remove only the malignant location while minimizing the destruction of good tissue with such exact depth and border information. These advantages of THz imaging in epithelial tissues imply that it has a large potential for cancer diagnosis on the exterior of internal organs, which may be helpful in situations like oral and digestive tumors.

As shown in Fig. 35, the data gathered utilizing different imaging techniques were compared to the THz pictures of tumor-bearing brain tissues. Using animal brain tumor models, the authors of [113] proved that THz imaging can define the border of the malignant region. THz imaging, according to [107], should be highly useful in identifying brain cancers utilizing patient-derived cancer models with traits similar to the diffuse border of human brain tumors.

Using blood constants, which offer qualitative and quantitative knowledge about significant constituents and waste products found in the human body, many diseases including cancer can be detected early. THz spectroscopy of blood cells on the other hand has not been substantially investigated. This is due to the fact that blood's THz spectrum is highly impacted by water, a key ingredient of blood, and lacks any clinically important spectral features [114]. Between 50 and 650 cm^{-1}, there are no notable changes in the spectrum between blood serum and water. A new method is demonstrated for qualitative and quantitative blood cell measurement because the linearity of THz signals and erythrocyte concentrations is excellent.

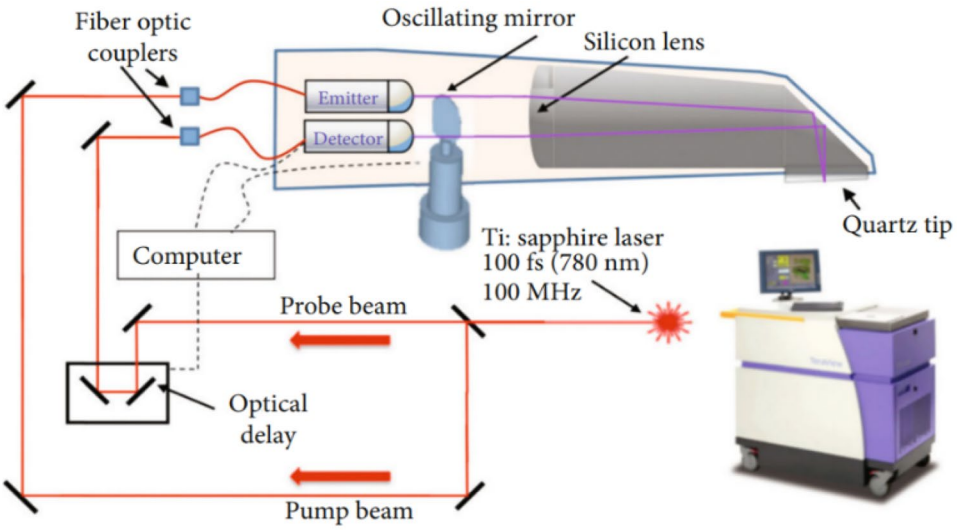

Fig. 33 Handheld TPI probe system [106]

THz Spectroscopy of Bacteria

Researchers have been examining the contributions of significant structural elements to the signature of the complete bacteria or spore as a result of the widespread use of THz technology for bacterial identification. Significant advances have been made in the areas of bacterial component characterization, spore identification, and cell detection [115]. THz waves can entirely penetrate through bacteria because of their small size and low absorption coefficient. Following that, microorganisms were examined qualitatively and quantitatively employing extensive research on bacteria, spores, and other bacterial components. Bacterial components namely DNA, dipicolinic acid (DPA), and metabolites are primarily responsible for the spectrum characteristics of bacteria or spores. The THz signature of bacterial cells and spores is produced by their DNA. THz spectroscopy can be used as a quick and label-free bacterial detection approach due to the diversity of biological contents [116]. Figure 36 depicts the basic analytical concepts of THz spectroscopy for bacterial detection.

THz metamaterials have recently risen to prominence as an effective method for detecting living and viable microbes [117–119]. Label-free detection has been developed by covering the substrate with an analyte-specific antibody [120–128]. The usage of antibody on the other hand is expensive and in general does not last making the sensors disposable. Therefore, a novel method for categorizing different types of microbes based on inherent characteristics, such as the dielectric constant, will be a game-changer in the development of an early detection tool. In [129], the authors studied the dielectric properties of molds, yeasts, and bacteria, adding to our basic understanding of microorganisms from a new perspective. This is predicated on the assumption that each group of microorganisms will have different dielectric characteristics due to their cellular

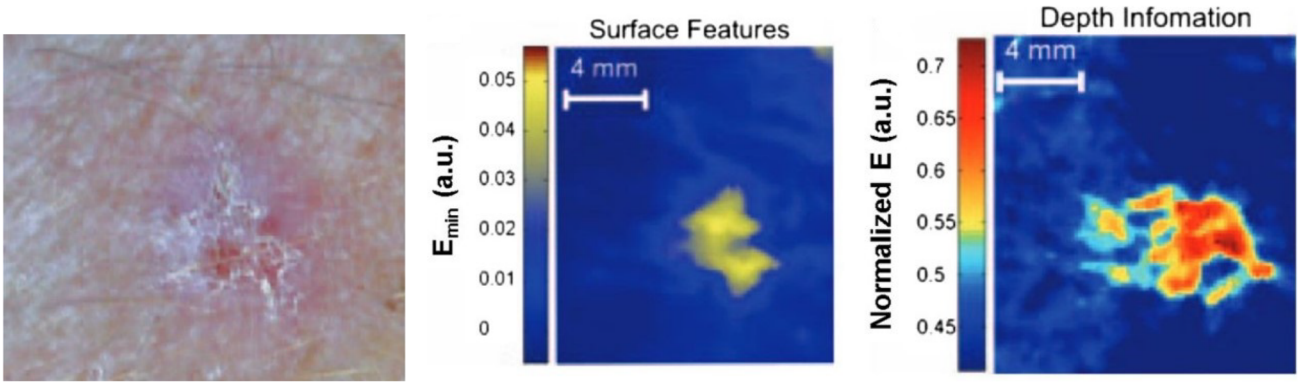

Fig. 34 **a** Cancer lesion on the arm of a patient. **b** THz image. **c** A THz picture of the tumor at a depth of 250-μm [112]

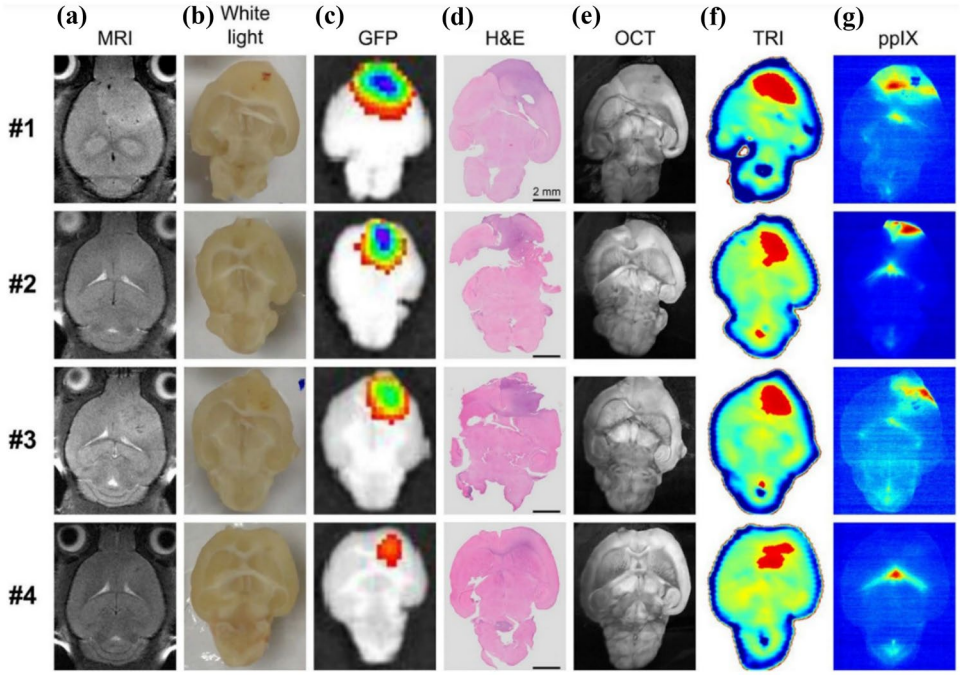

Fig. 35 THz images of tumor-bearing brain tissues [107]

shapes, as shown in Fig. 37. The composition of the cell wall is extremely important since many types of polysaccharides make up the rather thick walls of molds and yeasts in particular.

Concealed Object Detection in THz Ranges

THz imaging has four essential qualities that make it an effective tool in security screening applications, viz., 2D imaging, high-resolution 3D imaging, spectroscopy, and non-ionizing THz radiation. The measurement approach was created to test the possibility of detecting things wrapped in various types of fabrics. The measuring approach includes the hardware setup as well as the methodologies and algorithms employed during the measurements. A thermo-higro-barometer, four cameras, and two thermo elements make up the measurement setup [130, 131]. The four cameras used in the tests are commercially available namely a visible light (VIS) camera, a passive THz camera, and two infrared cameras.

Figure 38 depicts the measuring setup. The potential for finding concealed objects in the THz spectrum

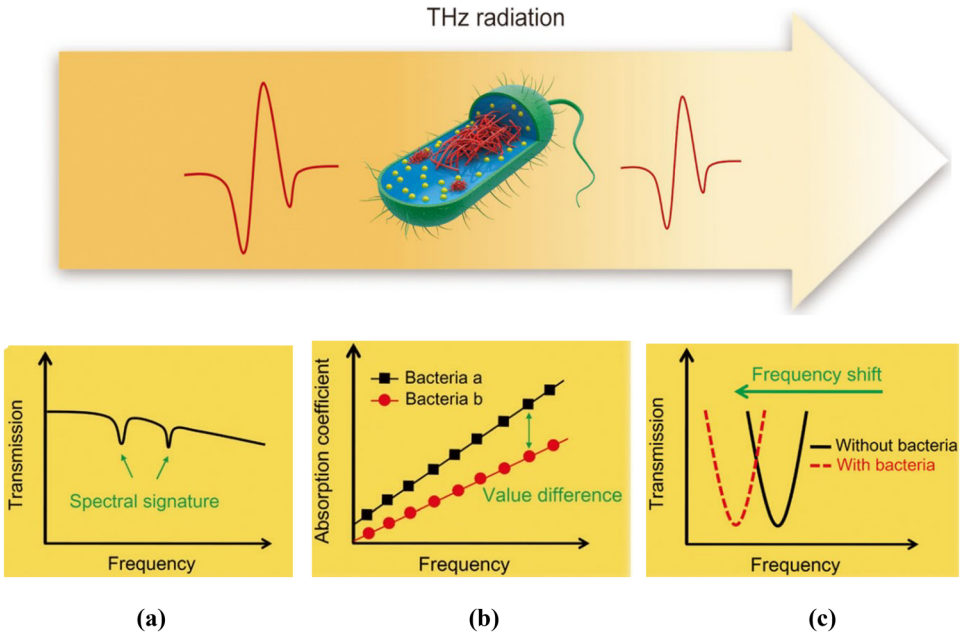

Fig. 36 THz spectroscopy of bacteria. **a** Spectral signature. **b** Absorption coefficients of bacterial species. **c** Resonant frequency shifts [116]

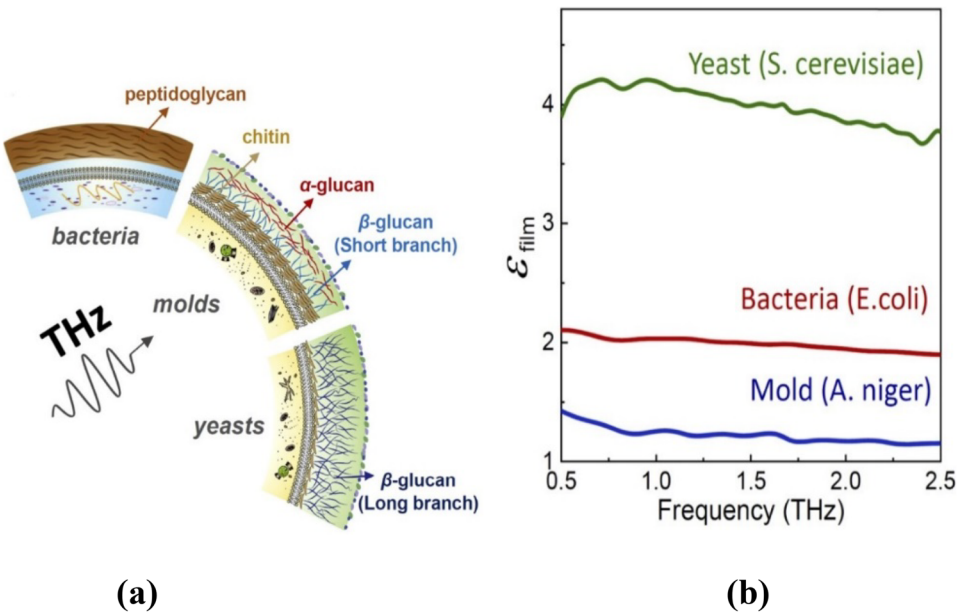

Fig. 37 **a** Mold, yeast, and bacterial cell wall compositions as well as their architectures. **b** Plots of dielectric constants that vary with frequency [129]

was tested using an imager operating at 250 GHz. To evaluate the viability of finding hidden objects in the infrared spectrum, two cameras were employed. A long-wavelength (LWIR) infrared camera is the first infrared camera utilized in the testing. A cooled InSbfocal plane array detector is used in the second infrared camera, which is a mid-wavelength (MWIR) infrared camera. Figure 39 depicts the collection of things. The experiment entailed gathering photographs of the person dressed in various outfits with various objects hidden beneath their clothing. The selection of objects to be disguised included both harmful and common objects, such as a wallet and a cell phone. The suggested algorithm was trained and tested using the data set of gathered photographs. The experiment has been broken down into 30-min sessions. The long-term measuring sessions were designed to gather images of several hidden objects with various contrasts and examine how decreasing contrast influenced detection and recognition. The preliminary research that established the session length showed that the hidden object used in this inquiry attained thermal equilibrium after 23–26 min. During measurement sessions, an individual clothed in various costumes with various objects concealed beneath clothing is captured in MWIR and THz images as shown in Fig. 40.

Two approaches for detecting the various concealed items are discussed in [133]. Both approaches execute detection and classification in a single architecture using

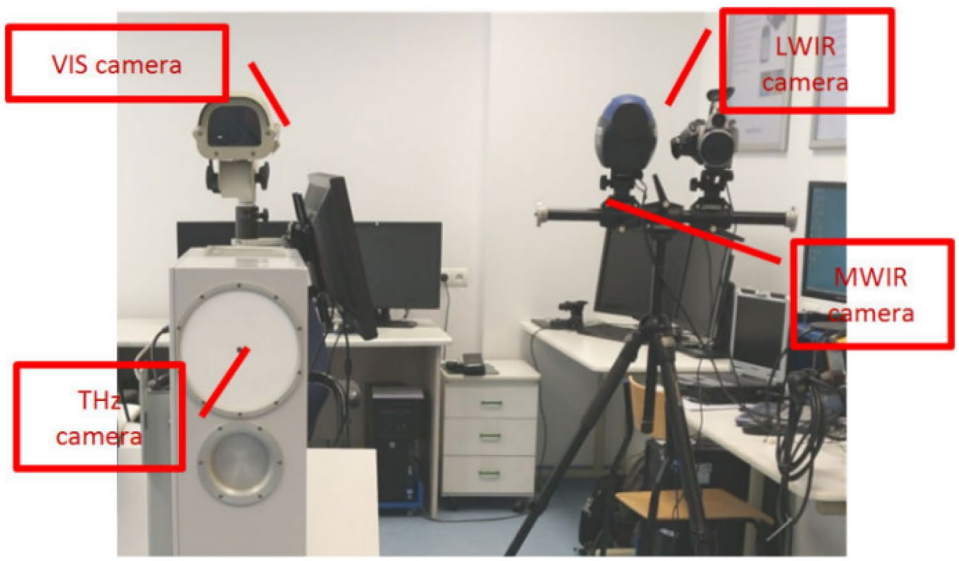

Fig. 38 Measurement setup. VIS camera: Visible light Camera; LWIR camera: Long-wavelength infrared camera; MWIR camera: Mid-wavelength infrared camera [132]

Fig. 39 Test objects [133]

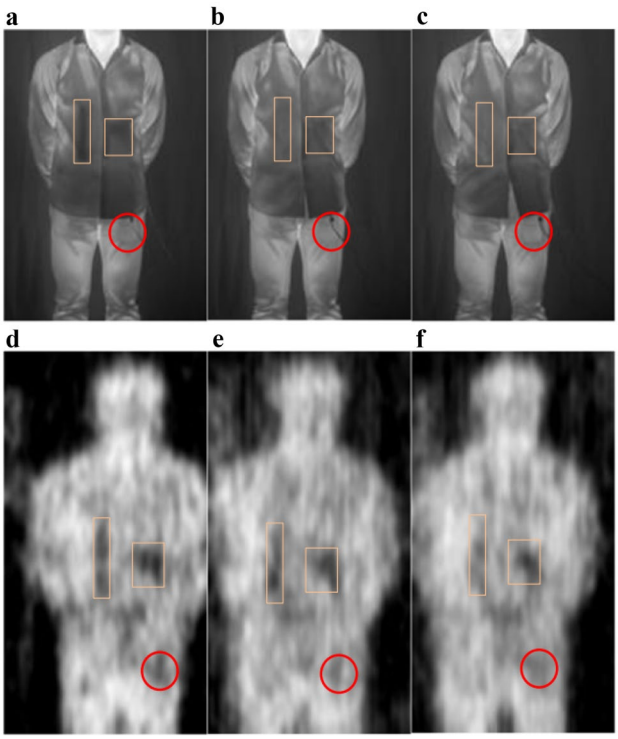

Fig. 40 Images of a person hiding a bomb and a firearm while donning a thick cotton shirt. **a** MWIR pictures were captured at the beginning of the measurement **b** after 15 min and **c** after 30 min. **d** THz pictures are captured at the commencement of the measurement **e** after 15 min and **f** after 30 min [133]

convolutional neural networks. You Only Look Once 3 (YOLO3) and R-FCN are the two deep learning-based techniques employed. Their architectures are depicted in Figs. 41 and 42.

Food Safety and Quality Inspection

Food safety and food quality are one of the key public concerns. THz imaging techniques help to test the safety and quality of food. To make sure of it, foreign bodies must be detected in food products. In the food sector, X-ray imaging is commonly employed to detect thick foreign bodies based on their noticeable density disparities [134–136]. Using a THz-TDS system, the authors in [137] evaluated the absorption spectra of nutmeat slices, shell, inner separator, and insects. The findings revealed that insects have distinct spectral characteristics, implying that THz technology could be used to identify pest damage in pecans. The inside of peanut shells, as well as the amount of peanuts, was clearly identifiable using this reflection-mode CW-THz imaging system (Fig. 43). The findings suggest that THz imaging could be used to identify pest damage in pecans. THz imaging is more reliable than X-ray imaging for low-density foreign body identification because the dielectric contrast mechanisms are considerably more pronounced at THz frequencies [138–140].

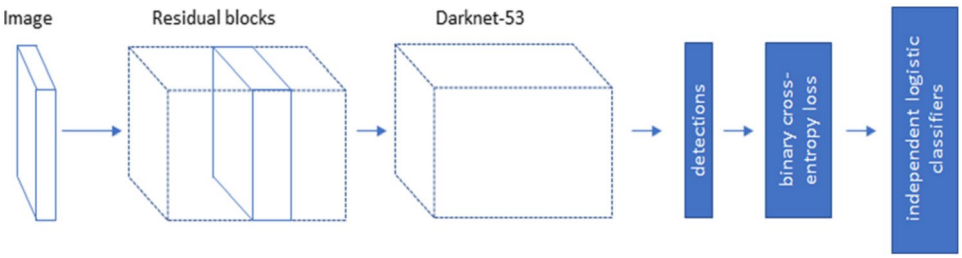

Fig. 41 Architecture of YOLO3 in hidden object detection

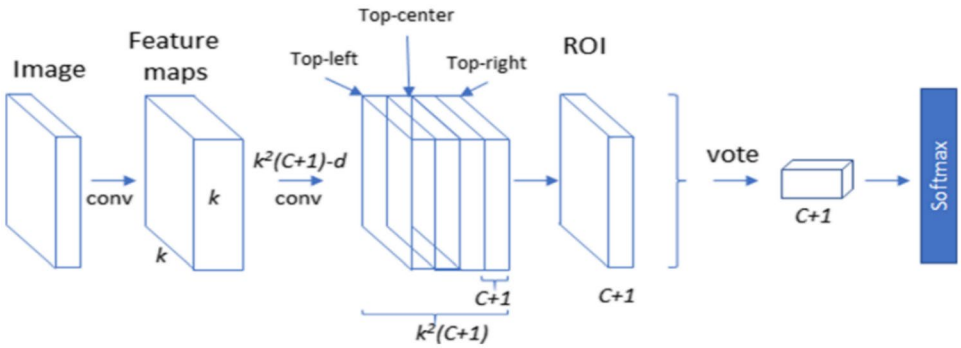

Fig. 42 Architecture of R-FCN in hidden object detection

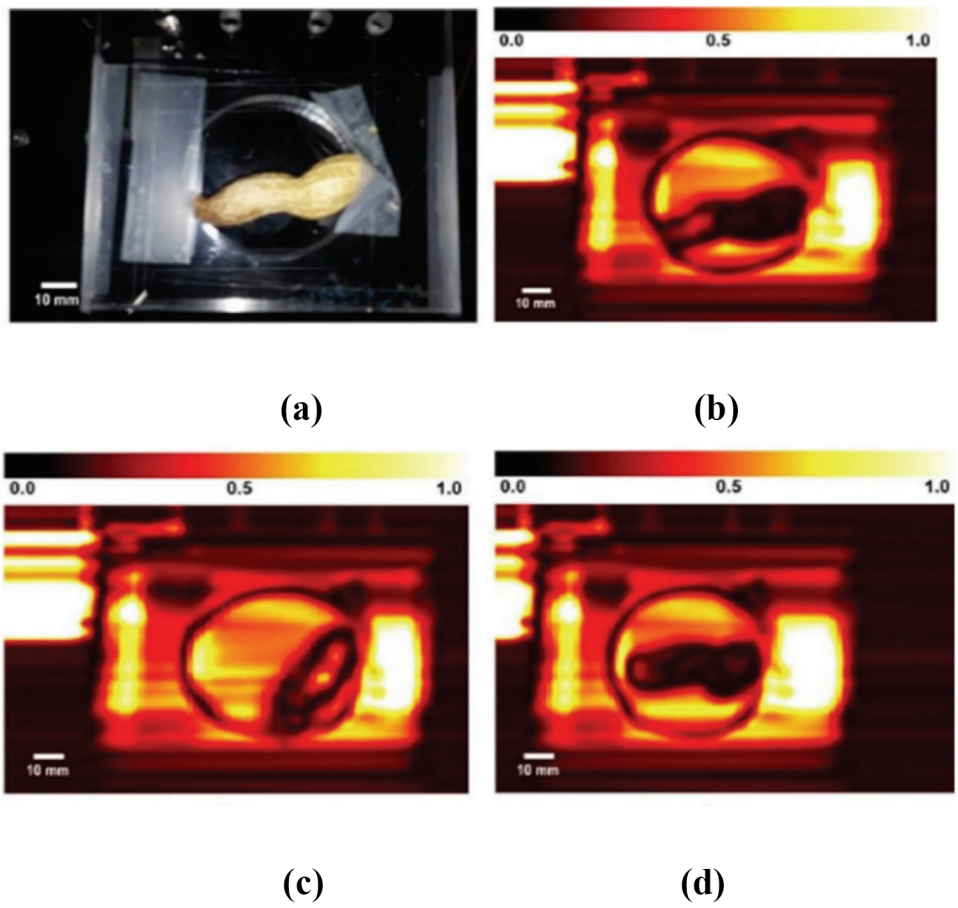

Fig. 43 **a** Peanut affixed on an acrylic support, Reflection picture from THz: **b** one peanut in a shell **c** empty shell and **d** two peanuts in a shell [88]

Table 3 THz frequencies and applications

Ref	THz frequency range	Sector/product	Findings
[86]	0.2–2 THz	Agriculture/Preservatives in grains	➔ Peak absorption was observed for sodium diacetate at 1.08 THz, 1.29 THz and 1.58 THz ➔ THz absorption peaks at low frequencies were attributed to phonon, intramolecular, or intermolecular collective motion
[103]	0.15–3.5 THz	Medical/Freshly excised breast cancer tumors	➔ Resolution reached 200 µm ➔ In comparison to healthy tissues, the malignant regions had increased absorption coefficients and refractive indices
[118]	0.6 to 1.4 THz	Biomedical/Yeast cells	➔ The surface concentration area is not far from the detection volume ➔ A 2 m wide slot results in a 3.5 m resonant frequency shift that is saturated
[141]	0.3–2 THz	Agriculture/Transmission behavior of plant leaves	➔ The attenuation coefficient and refractive index of coffee leaves were measured ➔ Computations were done due to thickness, permittivity and electrical characteristics of coffee leaves
[142]	0.4 and 0.75 THz	Food/Chocolate	➔ By contrasting their refractive indices, it is possible to distinguish between foreign bodies and other nuts ➔ Maintaining the scanning rate of 0.5 m/s reduces the effect of sample thickness
[143]	0.2 to 3 THz	Biomedical/Human hair	➔ Using THz-TDS Human hair was detected ➔ It is possible to detect even one hair
[144]	0.2 THz	Food/Milk	➔ Detects the presence of metals, polymers and insects
[145]	0 to 3 THz	Food/Harmful food additives	➔ The distinctive peaks of saccharin in both solution and pellet were located ➔ Peak frequencies for Thiabendazole (pellet and solutions) were 0.9, 1.2, 2.0, and 2.4 THz ➔ EDTA-2Na for the sample solution did not exhibit a peak, but pellet displayed two characteristic peaks at 1.9 and 2.4 GHz
[146]	0.2 to 1.6 THz	Industry/Talc powder in flour	➔ Peaks in the absorption of talc powder at 0.95, 1.36, and 1.56 THz ➔ One can determine the type of powder a sample of is made of using its refractive index and absorption coefficient
[147]	0.5 to 6 THz	Food/Honey	➔ Tetracycline, sulfathiazole, and Sulfapyridine were found at frequencies between 0.5 and 2.6 THz ➔ At 1.064 THz, Sulfapyridine showed a distinct single peak. Two peaks for sulfathiazole were seen at 1.88 THz and 2.04 THz ➔ There were a number of little peaks for tetracycline between 3.25 and 5.16 THz ➔ Antibiotics could be found in quantities as low as 1% weight for weight
[148]	1 to 10 THz	Food/ Gas barrier films include water molecules	➔ Linear correlation was discovered between the spectral intensity and the quantity of water molecules in the film ➔ The film's atoms did not mix with the water molecules, which continued to exist as "free water molecules" ➔ THz-TDS was used for monitoring water molecules inside a sample and assessing gas barrier films
[149]	0.1 to 1.5 THz	Medical/Skin Cancer	➔ THz TPS was used to examine the optical characteristics and spectrum characteristics of malignant skin melanocytes ➔ The distinct optical characteristics made it simple to distinguish between normal and cancerous melanocytes in mice
[150]	0.4–1.4 THz	Agriculture/Carbendazim in solutions	➔ There were very little amounts of carbendazim found ➔ The concentration of carbendazim has an impact on the metamaterials resonance peak ➔ Higher carbendazim concentrations led to reduced metamaterial frequency resonance ➔ Using metamaterial and THz spectroscopy, pesticides can be found with extremely high sensitivity
[151]	0–2.5 THz	Agriculture/Insect damaged wheat	➔ The shell, inner separator, and meat all had different absorption coefficients at frequencies higher than 1.2 THz ➔ Compared to dry weevil and nutmeat, the living insect showed a greater absorption rate

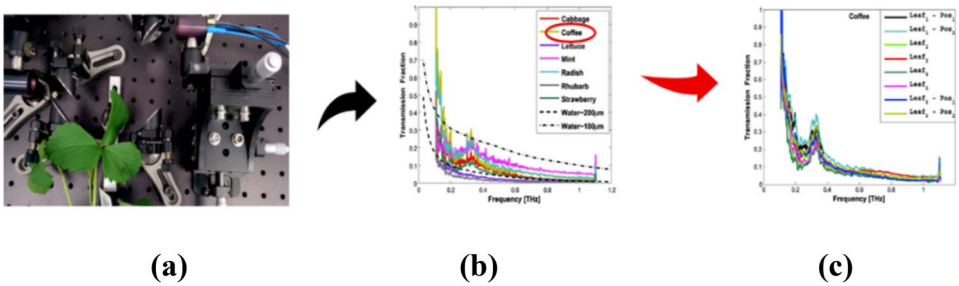

Fig. 44 **a** Continuous THz system, **b** THz transmission spectra of seven distinct plant leaves and **c** coffee leaf with several spots on the leaf [141]

Agricultural Applications

Initial applications of THz imaging included monitoring water content in plant leaves and detecting signs of plant dryness. THz has also been availed for pesticide and hazardous compound detection in crops, crop yield estimation, transgenics detection, seed quality management, and soil inspection. The authors in [152] looked at the THz properties of seven common plant leaves (Fig. 44). Transmission loss was calculated in strawberry, coffee, radish, lettuce, mint, cabbage, and rhubarb found a wide range of THz transmission loss between 0.3 and 0.4 THz. THz transmission loss varies depending on several aspects, including leaf texture, thickness, uniformity, and density. The THz transmission loss fluctuation was highest in cabbage leaves and lowest in coffee leaves. The texture and thickness of coffee leaves are consistent. The group also investigated the propagation of THz signals through thick layers of coffee leaves [141]. The thickness and permittivity measurements were used to make the calculations, which revealed a repetition pattern at around 130 GHz.

For the estimation of water in rapeseed leaves, the spectral data was analyzed using the Savitzky-Golay method, followed by partial least squares (PLS), boosting-PLS, and kernel PLS (KPLS). KPLS model is providing accuracy compared to other methods. According to the authors in [153], to measure the amount of water in leaves in the field, THz spectroscopy must be combined with mathematical modelling methods. THz-TDS system has been used to explore a variety of food and agriculture items. This technique can offer information on both phase and amplitude. THz pictures of a leaf which is of 60 mm long at different frequency bands are shown in Fig. 45. In order to detect the veins in the leaf, water absorption maxima exceeding 0.5 THz are required. Above 1.0 THz, the thorns in the leaf can also be seen. The results of the experiments show that THz TDS can be utilized for agricultural item inspection or monitoring.

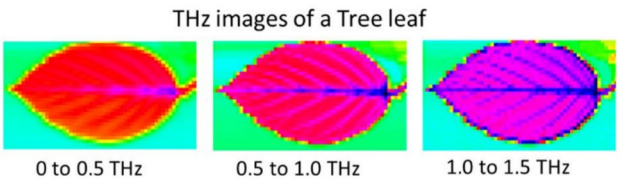

Fig. 45 Tree leaf THz pictures [153]

Using Swissto12 system, the authors in paper [154] conducted a preliminary investigation about the amount of water and any pesticides found in leaves. It also discovers the permittivity as well as the path-loss response of fresh and drought-stressed leaves. As illustrated in Fig. 46, the entire calibration process was designed to eliminate any measurement mistakes caused by the system or any other external source. The Swissto12 is compatible with frequencies between 0.75 and 1.2 THz and thicknesses between 40 and 4 mm. Furthermore, when running the experiments on various leaves, scattering parameters (S-parameters) were measured [155].

The experiment included six different fresh leaves: cauliflower, basil, iceberg, sage, cabbage, and lettuce, as shown in Fig. 47a. These leaves were all kept in the lab for 4 days with the same environmental factors. These leaves were not watered on the test days. The temperature maintained in the test environment was 23 °C ± 0.1 °C. The water content and any surface abnormalities on the leaves were assessed at three distinct points on the leaves. To examine the measurement findings of the leaves, Vernier callipers were used. The thickness of each leaf was measured independently under the same environmental circumstances. The thickness of the leaves at various positions

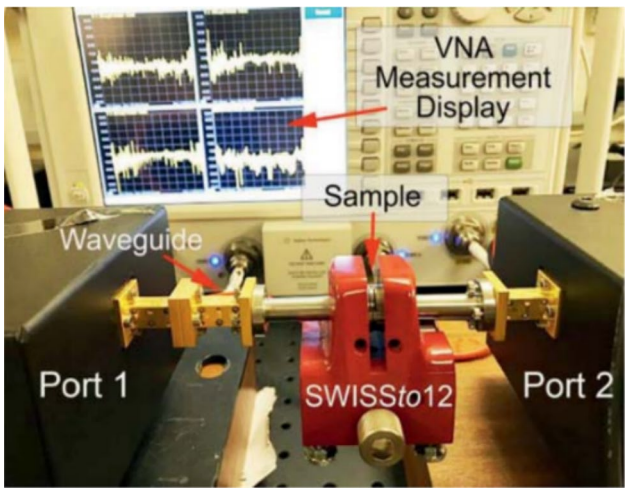

Fig. 46 Swissto12 THz system [154]

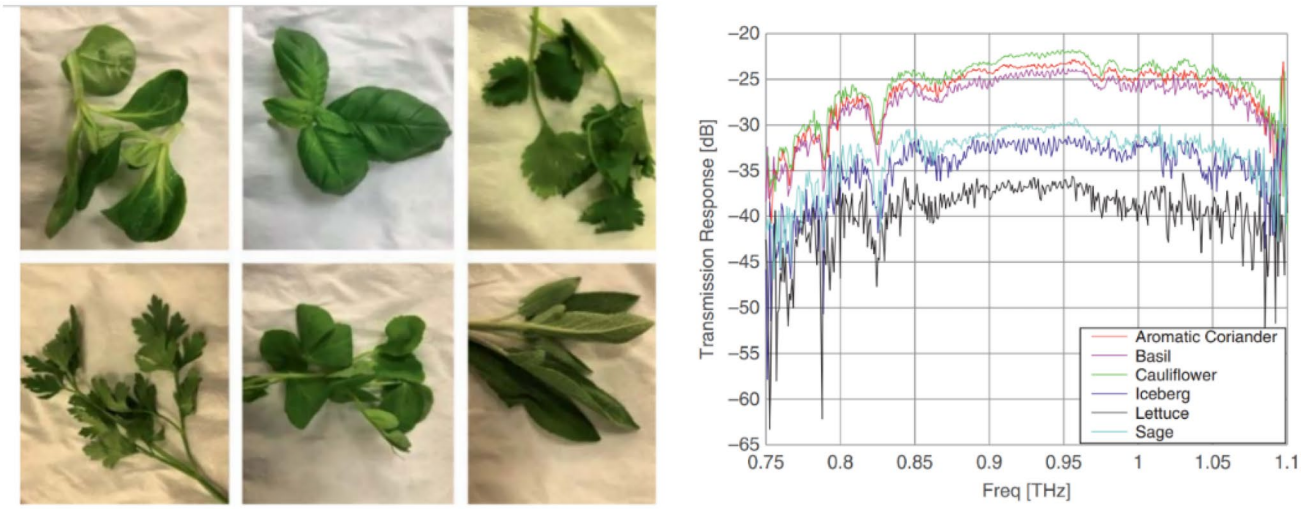

Fig. 47 **a** Samples of several fresh leaf types, **b** transmission response of various leaves [154]

was determined by repeating this process three times. During the process, it was discovered that the thickness rose steadily as the water content increased. According to the measurements, it was discovered that different leaves had varying levels of attenuation, which was obviously related to the amount of water in the leaves or the presence of pesticides. Cauliflower leaves are free of pesticides and have less water content than those of other plants, as seen in Fig. 47b. The leave reaction to path-loss is highly correlated with the amount of water in the leaves as well as their physical characteristics. As a result, it also emphasizes data on absorption loss, revealing the water content's absorption and reflection by the leaves. Absorption loss might be brought on by surface flaws or a considerable absorption of water content at the time of measurement.

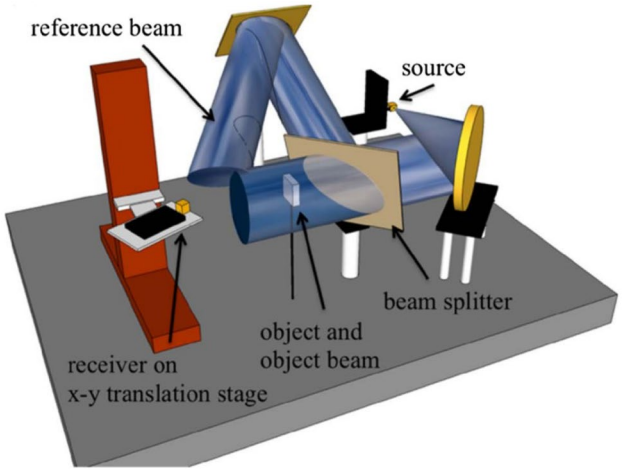

Fig. 48 THz holographic imager [155]

Holography and Ptychography Applications

THz digital holography (TDH) deals with the acquisition and processing of holograms with digital holographic images. THz sources suitable are THz laser, backward wave oscillator (BWO), or frequency multiplier and amplifiers following a synthesized microwave signal source. Two complementary detector technologies used are the diode detector and sub harmonic mixer receiver. The illustrative applications include imaging the internal void structure of visibly opaque dielectrics and imaging a thick terahertz lens using the dual-wavelength reconstruction method. Using THz holographic imager [155], holograms of amplitude and phase objects in transmission are captured and reconstruction is performed using angular spectrum and Fresnel diffraction methods. The experimental setup used to obtain holograph is "prototypical THz holographic imager" as shown in Fig. 48.

The in-line CW TDH approach is used for the early detection and treatment of liver cancer in high-risk groups of patients. The THz phase image showed evidence of fibrosis in the liver cancer tissue, and at a resolution of 158 μm, the appearance of healthy liver tissue was more homogeneous than that of the cancerous tissue. Hepatocellular carcinoma (HCC) tissue is found using CW THz digital in-line holography imaging system working at 2.52 THz [156]. With the help of initial value optimization and constraint conditions, this method presented phase reconstruction methods for in-line digital holography, which increased calculation efficiency. The digital photo of the sample is shown in Fig. 49.

The forewing of cicadas (Cryptotympana atrata) was imaged using a CW THz ptychography imaging system

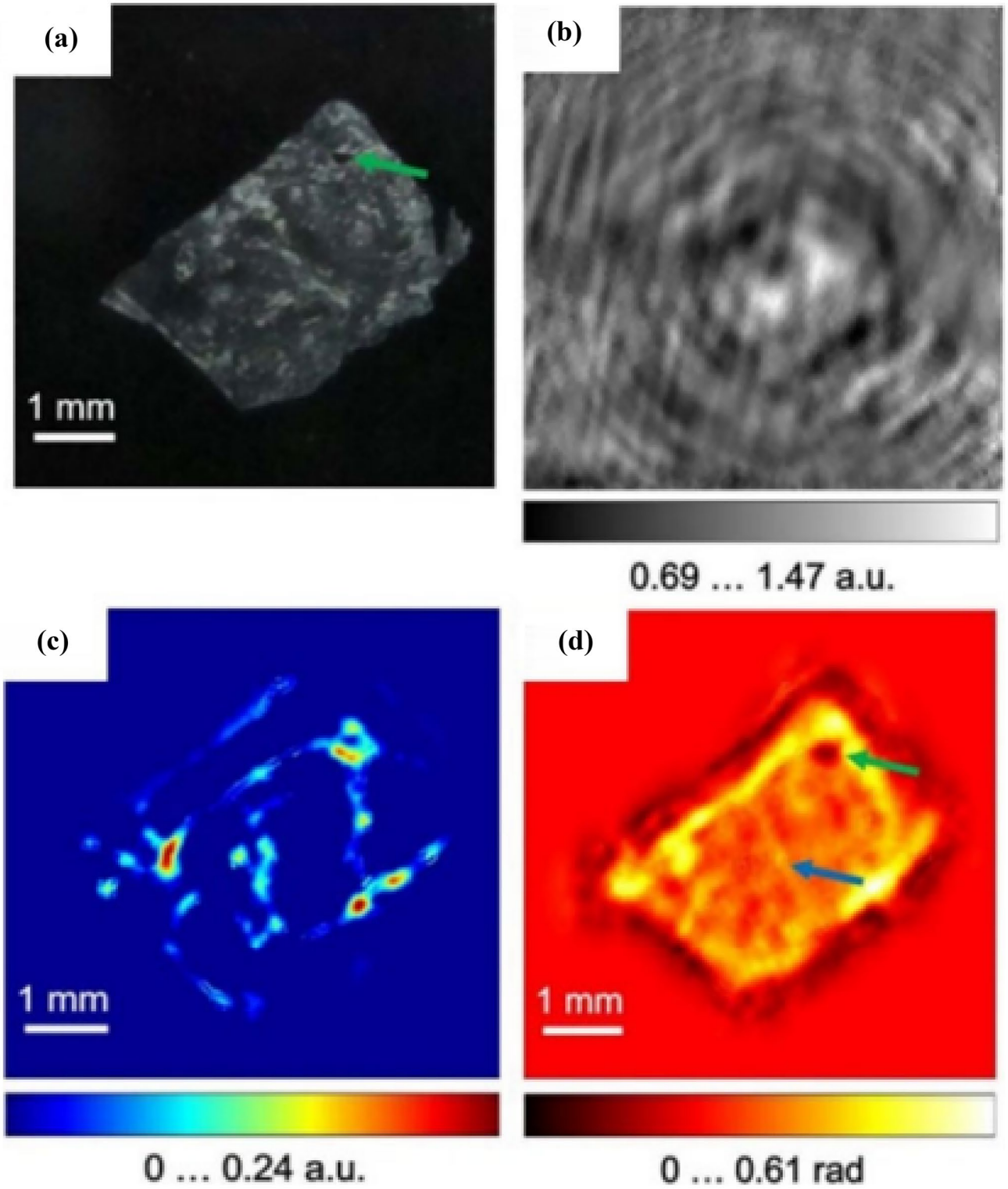

Fig. 49 **a** CW THz in-line holography of human liver cancer sample, **b** THz hologram, **c** reconstructed amplitude, and **d** phase images [156]

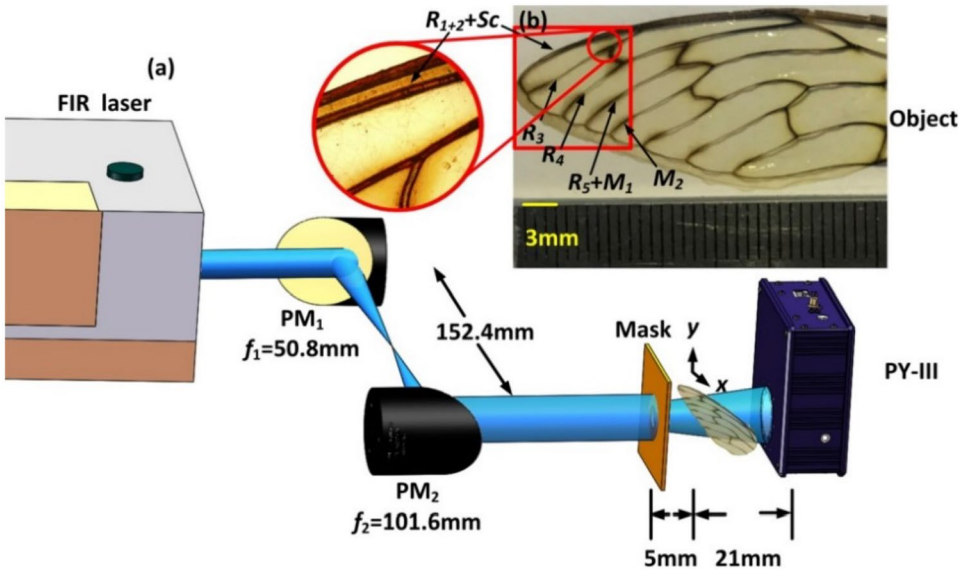

Fig. 50 **a** CW THz ptychography **b** forewing of cicadas, PMs: parabolic mirrors, Sc: subcostal, Rs: radius (R_1, R_2, R_3, R_4, R_5), Ms: media (M_1, M_2) and "+" indicates the convex vein [157]

made up of a FIRL 295 at 2.52 THz [157] and a pyrocam III detector, as illustrated in Fig. 50. During data collection, the sample was motorized by a 2-axis translation stage. The optical thickness of the membrane and veins can be obtained using CW THz ptychography using the complex-valued transmittance function that has been rebuilt. The THz scale venation has several features, making the reconstruction findings sensitive to probe translational errors. Phase retrieval algorithms find applications in terahertz coded aperture imaging and for non-destructive inspection applications [158].

Table 3 provides THz frequencies and corresponding applications. THz technology has revealed major differences between infected and healthy tissues. THz radiation is generally non-ionizing and of low intensity, making it suitable for biological application to both living and removed tissue. Because of their shorter wavelength, THz frequencies outperform microwaves in terms of imaging resolution and outperform infrared methods in terms of fat tissue transmittance. Many tumors, including basal cell carcinoma, brain, colon, and breast cancer, have been treated by THz imaging. THz waves can be utilized for characterizing and identifying a variety of meals and packaging materials in addition to passing through them. THz imaging has been used successfully in the non-invasive detection of dangerous compounds, toxins, and pathogens in food, and it is a great replacement for X-rays in food inspection and quality control activities. Because clothing transmits a lot of THz energy in that range, most THz-based hidden object detection systems operate below 1 THz. THz-based concealed object detection is built on the capacity to pierce fabrics and other substances with low water content. THz has also been used for soil inspection, detecting pesticides and other dangerous substances in crops, monitoring seed quality, identifying transgenic organisms, and estimating crop production.

Conclusion

The importance of THz technology and the numerous THz antennas used for THz imaging, also covering 6G frequencies, are discussed in this article. THz antennas were studied for their properties, features, and applications. A brief summary has been used to cover the THz communication. There has been discussion on the value of opening up the THz band as well as its possible uses in wireless communication in the future. The literature includes a thorough analysis of the various THz antenna types and some discussion on the choice of THz antenna material. Various THz image reconstruction techniques were also discussed. The quality of the image and, thus, the radiation dose are significantly impacted by image reconstruction. The goal of picture reconstruction is to obtain the least amount of noise possible for a given radiation dose without losing image correctness or spatial resolution. Because images of the same quality can be recreated at a lower dose, image reconstructions that increase image quality can result in a reduction in radiation exposure. The paper examined two basic categories of reconstruction methods: analytical reconstruction and iterative reconstruction (IR). Furthermore, various THz imaging applications were addressed and compared. THz technology has shown great promise in biomedical research, but a number of challenges need to be removed before it can be widely used in clinical settings. THz irradiation's biological safety is still unknown due to a lack of scientific evidence. THz waves have very low photon energies and were first believed to be harmless for human cells, tissues, and even the body. Researchers are reconsidering the bio-safety of THz irradiation in biomedical applications after recent studies showed that it can alter the genome, proteome, and transcriptome of cells

and tissues at certain intensities and periods. This review identified some open research issues in the work, which offer up new research vistas.

Author Contribution All the authors contributed to the study, conception, data collection, data analysis, and interpretations. A literature review and study on design techniques of THz imaging algorithms were written by Vulugundam Anitha. THz imaging applications and the study on implementation were contributed by Ankur Beohar. THz antennas design study and performance comparison were handled by Anveshkumar Nella. All the authors contributed to completing the writing and presentation of the whole manuscript.

Data Availability All the data generated during and/or analyzed during the current study are available from the corresponding author on reasonable request.

Code Availability Not applicable.

Declarations

Ethics Approval This work does not contain any studies with human participants or animals performed by any of the authors.

Consent to Participate Informed consent was obtained from all authors.

Consent for Publication The authors confirm that there is informed consent to the publication of the data contained in the article.

Conflict of Interest The authors declare no competing interests.

References

1. Lee AWM, Qin Qi, Sushil Kumar S, Williams BS, Quin Hu, Reno JL (2006) Real-time terahertz imaging over a standoff distance (>25 meters). Appl Phys Lett 89:141125. https://doi.org/10.1063/1.2360210
2. Fathololoumi S, Dupont E, Chan CWI, Wasilewski ZR, Laframboise SR, Ban D, Matyas A, Jirauschek C, Hu Q, Liu HC (2012) Terahertz quantum cascade lasers operating up to ~200 K with optimized oscillator strength and improved injection tunneling. Opt Express 20(4):3866–3876. https://doi.org/10.1364/OE.20.003866
3. Escorcia I, Grant J, Gough J, Cumming DRS (2016) Uncooled CMOS terahertz imager using a metamaterial absorber and pn diode. Opt Lett 41(14):3261–3264. https://doi.org/10.1364/OL.41.003261
4. Rogalski A, Sizov F (2011) Terahertz detectors and focal plane arrays. Opto-Electron Rev 19(3):346–404. https://doi.org/10.2478/s11772-011-0033-3
5. Amanti MI, Scalari G, Beck M, Faist J (2012) Stand-alone system for high resolution, real-time terahertz imaging. Opt Express 20:2772–2778. https://doi.org/10.1364/OE.20.002772
6. Locatelli M, Ravaro M, Bartalini S, Consolino L, Vitiello MS, Cicchi R, Pavone F, De Natale P (2015) Real-time terahertz digital holography with a quantum cascade laser. Sci Rep 5:13566. https://doi.org/10.1038/srep13566
7. Yamagiwa M, Ogawa T, Minamikawa T, Abdelsalam DG, Okabe K, Tsurumachi N, Mizutani Y, Iwata T, Yamamoto H, Yasui T (2018) Real-time amplitude and phase imaging of optically opaque objects by combining full-field off-axis terahertz digital holography with angular spectrum reconstruction. J Infrared, Millimeter Terahertz Waves 39:561–572. https://doi.org/10.1007/s10762-018-0482-6
8. Usami M, Iwamoto T, Ukasawa RF, Tani M, Watanabe M, Sakai K (2002) Development of a THz spectroscopic imaging system. Phys Med Biol 47(27):3749–3753. https://doi.org/10.1088/0031-9155/47/21/311
9. Tatiana Latychevskaia and Hans-Werner Fink (2007) Solution to the twin image problem in holography. Phys Rev Lett 98(23). https://doi.org/10.1103/PhysRevLett.98.233901
10. Maiden AM, Rodenburg JM (2009) An improved ptychographical phase retrieval algorithm for diffractive imaging. Ultramicroscopy 109(10). https://doi.org/10.1016/j.ultramic.2009.05.012
11. Vettikalladi H, Sethi WT, Abas AFB, Ko W, Alkanhal MA, Himdi M (2019) Sub-THz antenna for high-speed wireless communications systems. Hindawi, Int J Antennas Propag 2019:9573647. https://doi.org/10.1155/2019/9573647
12. He Y, Chen Y, Zhang L, Wong S-W, Chen ZN (2020) An overview of terahertz antennas. China Commun 17:124–165. https://doi.org/10.23919/J.CC.2020.07.011
13. Sharma A, Singh G (2009) Rectangular microstrip patch antenna design at THz frequency for short distance wireless communication systems. J Infrared, Millimeter Terahertz Waves 30:1. https://doi.org/10.1007/s10762-008-9416-z
14. Vizard DR (2006) Millimeter-wave applications: from satellite communications to security systems. Microw J 49(7):22–26
15. Ahmad I, Ullah S, Ullah S, Habib U, Ahmad S, Ghaffar A, Alibakhshikenari M, Khan S, Limiti E (2021) Design and analysis of a photonic crystal based planar antenna for THz applications. Electronics 10(16):1941. https://doi.org/10.3390/electronics10161941
16. Temmar MNE, Hocini A, Khedrouche D, Zamani M (2019) Analysis and design of a terahertz microstrip antenna based on a synthesized photonic bandgap substrate using BPSO. J Comput Electron 18(Springer):231–240. https://doi.org/10.1007/s10825-019-01301-x
17. Jha KR, Singh G (2012) Analysis and design of terahertz microstrip antenna on photonic bandgap material. J Comput Electron 11(4):364–373. https://doi.org/10.1007/s10825-012-0416-9
18. Chahat N, Reck TJ, Jung-Kubiak C, Nguyen T, Sauleau R, Chattopadhyay G (2015) 1.9-THz multiflare angle horn optimization for space instruments. IEEE Trans Terahertz Sci Technol 5(6):914–921. https://doi.org/10.1109/TTHZ.2015.2487781
19. Fan K, Hao Z-C, Hong W (2016) A 325–500 GHz high gain antenna for terahertz applications. International Symposium on Antennas and Propagation (ISAP), pp. 780–781
20. Sawada H, Kanno A, Yamamoto N, Fujii K, Kasamatsu A, Ishizu K, Kojima F, Ogawa H, Hosako I (2017) High gain antenna characteristics for 300 GHz band fixed wireless communication systems. Progress in Electromagnetics Research Symposium – Fall (PIERS - FALL), pp 1409–1412. https://doi.org/10.1109/PIERS-FALL.2017.8293350
21. Wang X, Deng C, Hu W, Lv X, Ligthart LP (2017) Dual-band dielectric-loaded horn antenna for terahertz applications. International Applied Computational Electromagnetics Society Symposium (ACES), pp. 1–2
22. Zhou MM, Cheng YJ (2018) D-band high-gain circular-polarized plate array antenna. IEEE Trans Antennas Propag 66(3):1280–1287. https://doi.org/10.1109/TAP.2018.2796299
23. Bird T (2006) Terahertz radio systems: the next frontier? CSIRO ICT Centre, Mersfield, NSW, vol. 5, pp. 1-11.
24. Gearhart SS, Ling CC, Rebeiz GM (1991) Integrated millimeter-wave corner-cube antennas. IEEE Trans Antennas Propag 39(7):1000–1006. https://doi.org/10.1109/8.86921
25. Gearhart SS, Ling CC, Rebeiz GM, Davee H, Chin G (1991) Integrated 119-μm linear corner-cube array. IEEE Microw Guided Wave Lett 1(7):155–157. https://doi.org/10.1109/75.84567

26. Markish O, Leviatan Y (2016) Analysis and optimization of terahertz bolometer antennas. IEEE Trans Antennas Propag 64(8):3302–3309. https://doi.org/10.1109/TAP.2016.2573861
27. Zheng Xu, Dong X, Borneman J (2014) Design of a reconfigurable MIMO system for THz communications based on graphene antennas. IEEE Trans Terahertz Sci Technol 4(5):609–661. https://doi.org/10.1109/TTHZ.2014.2331496
28. Liu Z, Meng Y, Futai Hu, Xiao Q, Yan P, Gong M (2019) Largely tunable terahertz circular polarization splitters based on patterned graphene nanoantenna arrays. IEEE Photonics J 11(5):1–11. https://doi.org/10.1109/JPHOT.2019.2935752
29. Wang Y, Zhang X, Wang J, Liu J, Wang Y, Yang K, Yinglin (2010) Manipulating surface plasmon polaritons in a 2-D T-shaped metal-insulator-metal plasmonic waveguide with a joint cavity. IEEE Photon Technol Lett 22(17):1309–1311. https://doi.org/10.1109/LPT.2010.2053531
30. Feng N-N, Brongersma ML, Dal Negro L (2007) Metal-dielectric slot-waveguide structures for the propagation of surface plasmon polaritons at 1.55 μm. IEEE J Quant Electron 43(6):479–485. https://doi.org/10.1109/JQE.2007.897913
31. Hua Lu, Zeng C, Zhang Q, Xueming Liu Md, Hossain M, Reineck P, Min Gu (2015) Graphene-based active slow surface plasmon polaritons. Sci Rep 5(8443):1–7. https://doi.org/10.1038/srep08443
32. Bonaccorso F, Sun Z, Hasan T, Ferrari AC (2010) Graphene photonics and optoelectronics. Nat Photonics 4(9):611–622. https://doi.org/10.1038/nphoton.2010.186
33. Varshney G (2020) Tunable terahertz dielectric resonator antenna. Silicon, Springer. https://doi.org/10.1007/s12633-020-00577
34. Varshney G, Gotra S, Kaur J, Pandey VS, Yaduvanshi RS (2019) Obtaining the circular polarization in a nano-dielectric resonator antenna for photonics applications. Semicond Sci Technol 34(7):07LT01. https://doi.org/10.1088/1361-6641/ab1fd1
35. Varshney G, Gotra S, Pandey VS, Yaduvanshi RS (2018) Inverted sigmoid shaped multiband dielectric resonator antenna with dualband circular polarization. IEEE Trans Antennas Propag 66(4):2067–2072. https://doi.org/10.1109/TAP.2018.2800799
36. Varshney G (2020) Reconfigurable graphene antenna for THz applications: a mode conversion approach. Nanotechnology 31:13. https://doi.org/10.1088/1361-6528/ab60cc
37. Meng Xie, Guizhen Lu (2017) Research on terahertz photoconductive antenna. IEEE 5th International Symposium on Electromagnetic Compatibility (EMC-Beijing), pp. 1–5, 2017. https://doi.org/10.1109/EMC-B.2017.8260432
38. Zhang L, Dai Z (2015) Terahertz fuze antenna technique based on dielectric lens. J Terahertz Sci Electron Inf Technol 13(1):31–34
39. Llombart N, Chattopadhyay G, Skalare A, Mehdi I (2011) Novel terahertz antenna based on a silicon lens fed by a leaky wave enhanced waveguide. IEEE Trans Antennas Propag 59(6):2160–2168. https://doi.org/10.1109/TAP.2011.2143663
40. Alonso-DelPino M, Llombart N, Chattopadhyay G, Lee C, Jung-Kubiak C, Jofre L, Mehdi I (2013) Design guidelines for a terahertz silicon micro-lens antenna. IEEE Antennas Wirel Propag Lett 12:84–87. https://doi.org/10.1109/LAWP.2013.2240252
41. Hossain AKMZ, Ibrahimy MI, Motakabber SMA (2014) Integrated Si lens antenna with planar log spiral feed for THz band. International Conference on Computer and Communication Engineering, pp. 284–287. https://doi.org/10.1109/ICCCE.2014.87
42. Hao Z-C, Wang J, Yuan Q, Hong W (2017) Development of a low-cost THz metallic lens antenna. IEEE Antennas Wirel Propag Lett 16:1751–1754. https://doi.org/10.1109/LAWP.2017.2671880
43. Hao Z-C, Hong W, Chen J-X, Zhai JF (2018) Investigations on the terahertz beam scanning antennas with a wide scanning range. 12th European Conference on Antennas and Propagation (EuCAP), pp. 1–3. https://doi.org/10.1049/cp.2018.0702
44. Paul Moseley, Giorgio Savini, Peter Ade (2018) Large aperture metal-mesh lenses for THz astronomy. 12th European Conference on Antennas and Propagation (EuCAP), pp. 1–3. https://doi.org/10.1049/cp.2018.0604
45. Dyck A, Rösch M, Tessmann A, Leuther A, Kuri M, Wagner S (2019) A transmitter system-in-package at 300 GHz with an off-chip antenna and GaAs-based MMICs. IEEE Trans Terahertz Sci Technol 9(3):335–344. https://doi.org/10.1109/TTHZ.2019.2910511
46. Lei-Jun Xu, Tong F-C, Bai X, Li Q (2018) Design of miniaturised on-chip slot antenna for THz detector in CMOS. IET Microwaves Antennas Propag 12(8):1324–1331. https://doi.org/10.1049/iet-map.2017.0833
47. Rubani Q, Gupta SH, Pani S, Kumar A (2019) Design and analysis of a terahertz antenna for wireless body area networks. Optik 179:684–690. https://doi.org/10.1016/j.ijleo.2018.10.202
48. Rabbani MS, Ghafouri-Shiraz H (2017) Liquid crystalline polymer substrate based THz microstrip antenna arrays for medical applications. IEEE Antennas Wireless Propag Lett 16:1533–1536. https://doi.org/10.1109/LAWP.2017.2647825
49. Gurnoor Singh Brar, Vatanjeet Singh and Ekambir Sidhu (2016) Stacked decagon shaped THz microstrip patch antenna design for detection of GaAs semi-conductor properties. International Conference on Automatic Control and Dynamic Optimization Techniques (ICACDOT) International Institute of Information Technology (I^2IT), Pune. https://doi.org/10.1109/ICACDOT.2016.7877691
50. Zhong J-Y, Lin W-J, Cheng J-H, Kung Y-H, Chen J-P, Tsai J-H (2019) A high spectral efficiency receiver at 57–66 GHz using 65-nm CMOS in LTCC package with Polarization MIMO. IEEE Access 7:129466–129479. https://doi.org/10.1109/ACCESS.2019.2938845
51. Cheema HM, Shamim A (2013) The last barrier: on-chip antennas. IEEE Microwave Mag 14(1):79–91. https://doi.org/10.1109/MMM.2012.2226542
52. Burasa P, Djerafi T, Constantin NG, Ke Wu (2017) On-chip dualband rectangular slot antenna for single-chip millimeter-wave identification tag in standard CMOS technology. IEEE Trans Antennas Propag 65(8):3858–3868. https://doi.org/10.1109/TAP.2017.2710215
53. Jalili H, Momeni O (2017) 17.10 A 318-to-370GHz standing-wave 2D phased array in 0.13μm BiCMOS. 2017 IEEE International Solid-State Circuits Conference, pp. 310–311, pp. 2376–8606. https://doi.org/10.1109/ISSCC.2017.7870385
54. Kong S, Shum KM, Yang C, Gao L, Chan CH (2021) Wide impedance-and gain-bandwidth terahertz on-chip antenna with chip-integrated dielectric resonator. IEEE Trans Antennas Propag 69(8):4269–4278. https://doi.org/10.1109/TAP.2021.3060060
55. Garbacz P (2016) Terahertz imaging – principles, techniques, benefits, and limitations. Problemy Eksploatacji 81–92
56. Shalaby M, Vicario C, Hauri CP (2015) High-performing nonlinear visualization of terahertz radiation on a silicon charge-coupled device. Nat Commun 6:8439. https://doi.org/10.1038/ncomms9439
57. El Fatimy A, Myers-Ward RL, Boyd AK, Daniels KM, Kurt Gaskill D, Barbara P (2016) Epitaxial graphene quantum dots for high-performance terahertz bolometers. Nat Nanotechnol 11:335–338. https://doi.org/10.1038/nnano.2015.303
58. Soumekh M (1999) Synthetic aperture radar signal processing. Wiley, New York
59. Zhang S (2009) Engineering electromagnetic theory. Science Press, Beijing
60. Weng Cho Chew (1990) Waves and fields in inhomogeneous media. Van Nostrand Reinhold, New York
61. Wang G, Qi F, Liu Z, Liu C, Xing C, Ning W (2020) Comparison between back projection algorithm and range migration

algorithm in terahertz imaging. IEEE Access 8:18772–18777. https://doi.org/10.1109/ACCESS.2020.2968085
62. Sheen DM, McMakin DL, Hall TE (2001) Three-dimensional millimeter-wave imaging for concealed weapon detection. IEEE Trans Microw Theory Tech 49(9):1581–1592. https://doi.org/10.1109/22.942570
63. Guo Q, Chang T, Geng G, Jia C, Cui H-L (2016) A high precision terahertz wave image reconstruction algorithm. Sensors 16:1139. https://doi.org/10.3390/s16071139
64. Ahmed SS, Schiessl A, Schmidt L-P (2009) Multistatic mm-wave imaging with planar 2D-array. German Microwave Conference, Munich, Germany, pp. 1–4. https://doi.org/10.1109/GEMIC.2009.4815908
65. Chana WL, Charan K, Takhar D, Kelly KF, Baraniuk RG, Mittleman DM (2008) A single-pixel terahertz imaging system based on compressed sensing. Appl Phys Lett 93(12):121105. https://doi.org/10.1063/1.2989126
66. Shang Y, Wang X, Sun W, Han P, Ye J, Feng S, Zhang Y (2019) Terahertz image reconstruction based on compressed sensing and inverse Fresnel diffraction. Opt Express 27(10):14725–14735. https://doi.org/10.1364/OE.27.014725
67. Stantchev RI, Sun B, Hornett SM, Hobson PA, Gibson GM, Padgett MJ, Hendry E (2016) Non-invasive, near-field terahertz imaging of hidden objects using a single-pixel detector. Sci Adv 2(6). https://doi.org/10.1126/sciadv.1600190
68. Stantchev RI, Phillips DB, Hobson P, Hornett SM, Padgett MJ, Hendry E (2017) Compressed sensing with near-field THz radiation. Optica 4(8):989–992. https://doi.org/10.1364/OPTICA.4.000989
69. Xu L-M, Fan W-H, Liu J (2014) High-resolution reconstruction for terahertz imaging. Appl Opt 7891–7897.https://doi.org/10.1364/AO.53.007891
70. Fosodeder P, Hubmer S, Ploier A, Ramlau R, Van Frank S, Rankl C (2021) Phase-contrast THz-CT for non-destructive testing. Opt Express 29(10):15711–15723. https://doi.org/10.1364/OE.422961
71. Park SC, Park MK, Kang MG (2003) Super-resolution image reconstruction: a technical overview. IEEE Signal Process Mag 20(3):21–36. https://doi.org/10.1109/MSP.2003.1203207
72. Elad M, Feuer A (1997) Restoration of a single super resolution image from several blurred, noisy, and under sampled measured images. IEEE Trans Image Process 6(12):1646–1658. https://doi.org/10.1109/83.650118
73. Borman S, Stevenson RL (1998) Super-resolution from image sequences-a review. Midwest Symposium on Circuits and Systems, IEEE. https://doi.org/10.1109/MWSCAS.1998.759509
74. Stark H, Oskoui P (1989) High-resolution image recovery from image-plane arrays, using convex projections. J Opt Soc Am A 6(11):1715–1726. https://doi.org/10.1364/JOSAA.6.001715
75. Li Y, Li L, Hellicar A, Guo YJ (2008) Super-resolution reconstruction of terahertz images. Terahertz Mil Secur Appl VI. 6949. https://doi.org/10.1117/12.777814
76. Gao H, Li C, Wu S, Fang G (2018) Study of terahertz MIMO imaging with fast reconstruction algorithm. 2018 IEEE MTT-S International Wireless Symposium (IWS). https://doi.org/10.1109/IEEE-IWS.2018.8400832
77. Yang G, Li C, Gao H, Fang G (2020) Phase shift migration with SIMO superposition for MIMO-side looking imaging at terahertz band. IEEE Access 8:208418–208426. https://doi.org/10.1109/ACCESS.2020.3017617
78. Yang G, Li C, Shiyou W, Zheng S, Liu X, Fang G (2021) Phase shift migration with modified coherent factor algorithm for MIMO-SAR 3D imaging in THz band. Remote Sens 13(22):4701. https://doi.org/10.3390/rs13224701
79. Lei T, Tobin B, Liu Z, Yang S-Y, Sun D-W (2021) A terahertz time-domain super-resolution imaging method using a local-pixel graph neural network for biological products. Anal Chim Acta 1181. https://doi.org/10.1016/j.aca.2021.338898
80. Heimbeck MS, Everitt HO (2020) Terahertz digital holographic imaging. Adv Opt Photon 12(1):1–59. https://doi.org/10.1364/AOP.12.000001
81. Valzania L, Hack E, Zolliker P, Bronnimann R, Feurer T (2018) Resolution limits of terahertz ptychography. Society of Photo-Optical Instrumentation Engineers (SPIE) Photonics, Proceedings 10677. https://doi.org/10.1117/12.2307157
82. Rodenburg JM, Faulkner HM (2004) A phase retrieval algorithm for shifting illumination. Appl Phys Lett 85(20):4795–4797. https://doi.org/10.1063/1.1823034
83. Rodenburg JM (2008) Ptychography and related diffractive imaging methods. Adv Imaging Electron Phys 150:87–184. https://doi.org/10.1016/S1076-5670(07)00003-1
84. Valzania L, Feurer T, Zolliker P, Hack E (2018) Terahertz ptychography. Opt Lett 43(3):543–546. https://doi.org/10.1364/OL.43.000543
85. Seifert J, Bouchet D, Loetgering L, Mosk AP (2021) Efficient and flexible approach to ptychography using an optimization framework based on automatic differentiation. OSA Continuum 4(1):121–128. https://doi.org/10.1364/OSAC.411174
86. Ge H, Jiang Y, Lian F, Zhang Y (2016) Terahertz spectroscopy investigation of preservative molecules. Optik 127(12):4954–4958. https://doi.org/10.1016/j.ijleo.2016.02.048
87. Shin HJ, Sung-Wook C, Ok G (2018) Qualitative identification of food materials by complex refractive index mapping in the terahertz range. Food Chem 245:282–288. https://doi.org/10.1016/j.foodchem.2017.10.056
88. Ok G, Park K, Kim HJ, Chun HS, Choi S-W (2014) High-speed terahertz imaging toward food quality inspection. Appl Opt 53(7):1406–1412. https://doi.org/10.1364/AO.53.001406
89. Wang K, Sun D-W, Hongbin Pu (2017) Emerging non-destructive terahertz spectroscopic imaging technique: principle and applications in the agri-food industry. Trends Food Sci Technol 67:93–105. https://doi.org/10.1016/j.tifs.2017.06.001
90. Yan L, Liu C, Hao Qu, Liu W, Zhang Y, Yang J, Zheng L (2018) Discrimination and measurements of three flavonols with similar structure using terahertz spectroscopy and chemometrics. Journal of Infrared Milli Terahz Waves 39:492–504. https://doi.org/10.1007/s10762-018-0474-6
91. Castro-Camus E, Palomar M, Covarrubias AA (2013) Leaf water dynamics of Arabidopsis thaliana monitored in-vivo using terahertz time-domain spectroscopy. Sci Rep 3:2910. https://doi.org/10.1038/srep02910
92. Leili AH, Akbari E, Toudeshki A, Homayouni T, Alizadeh A, Ehsani R (2020) Terahertz spectroscopy and imaging: a review on agricultural applications. Comput Electron Agric 177:105628. https://doi.org/10.1016/j.compag.2020.105628
93. Lee D-K, Kim G, Kim C, Jhon YM, Kim JH, Lee T, Son J-H (2016) Ultrasensitive detection of residual pesticides using THz near-field enhancement. IEEE Trans Terahertz Sci Technol 6(3):389–395. https://doi.org/10.1109/TTHZ.2016.2538731
94. Nie P, Qu F, Lin L, He Y, Feng X, Yang L, Gao H, Zhao L, Huang L (2021) Trace identification and visualization of multiple benzimidazole pesticide residues on toona sinensis leaves using terahertz imaging combined with deep learning. Int J Mol Sci 22(7). https://doi.org/10.3390/ijms22073425
95. Lee D-K, Kim G, Son J-H, Seo M (2016) Highly sensitive terahertz spectroscopy of residual pesticide using nano-antenna. Terahertz, RF, Millimeter, and Submillimeter-Wave Technology and Applications IX, International Society for Optics and Photonics, San Francisco, CA, USA. https://doi.org/10.1117/12.2212055
96. El-Shenawee M, Vohra N, Bowman T, Bailey K (2019) Cancer detection in excised breast tumors using terahertz imaging and spectroscopy. Biomed Spectrosc Imaging 8(1–2):1–9. https://doi.org/10.3233/bsi-190187

97. Gavdush AA, Chernomyrdin NV, Malakhov KM, Beshplav S-I, Dolganova IN, Kosyrkova AV, Nikitin PV, Musina GR, Katyba GM, Reshetov IV, Cherkasova OP, Komandin GA, Karasik VE, Potapov AA, Tuchin VV, Zaytsev KI (2019) Terahertz spectroscopy of gelatin-embedded human brain gliomas of different grades: a road toward intraoperative THz diagnosis. J Biomed Opt 24(02):1. https://doi.org/10.1117/1.JBO.24.2.027001
98. Vohra N, Bowman T, Diaz PM, Rajaram N, Bailey K, El-Shenawee M (2018) Pulsed terahertz reflection imaging of tumors in a spontaneous model of breast cancer. Biomed Phys Eng Expr 4(6). https://doi.org/10.1088/2057-1976/aae699
99. Bowman T, El-Shenawee M, Campbell LK (2016) Terahertz transmission vs reflection imaging and model-based characterization for excised breast carcinomas. Biomed Opt Express 7(9):3756–3783. https://doi.org/10.1364/BOE.7.003756
100. Bowman T, Yuhao Wu, Gauch J, Campbell LK, El-Shenawee M (2017) Terahertz imaging of three-dimensional dehydrated breast cancer tumors. J Infrared Millimeter Terahertz Waves 38:766–786. https://doi.org/10.1007/s10762-017-0377-y
101. Bowman T, Chavez T, Khan K, Wu J, Chakraborty A, Rajaram N, Bailey K, El-Shenawee M (2018) Pulsed terahertz imaging of breast cancer in freshly excised murine tumors. J Biomed Opt 23(2). https://doi.org/10.1117/1.JBO.23.2.026004
102. Bowman TC, El-Shenawee M, Campbell LK (2005) Terahertz imaging of excised breast tumor tissue on paraffin sections. IEEE Trans Antennas Propag 63(5):2088–2097. https://doi.org/10.1109/TAP.2015.2406893
103. Bowman T, Vohra N, Bailey K, El-Shenaweea M (2019) Terahertz tomographic imaging of freshly excised human breast tissues. J Med Imaging 6(2):23501. https://doi.org/10.1117/1.JMI.6.2.023501
104. Chavez T, Bowman T, Jingxian Wu, Bailey K, El-Shenawee M (2018) Assessment of terahertz imaging for excised breast cancer tumors with image morphing. J Infrared Millimeter Terahertz Waves 39(12):1283–1302. https://doi.org/10.1007/s10762-018-0529-8
105. Peng Y, Shi C, Wu X, Zhu Y, Zhuang S (2020) Terahertz imaging and spectroscopy in cancer diagnostics: a technical review. BME Front 2020:1–11, Article ID 2547609. https://doi.org/10.34133/2020/2547609
106. Grootendorst MR, Fitzgerald AJ, Susan G, de Koning B, Santaolalla A, Portieri A, Van Hemelrijck M, Young MR, Owen J, Cariati M, Pepper M, Wallace VP, Pinder SE, Purushotham A (2017) Use of a handheld terahertz pulsed imaging device to differentiate benign and malignant breast tissue. Biomed Opt Express 8(6):2932–2945. https://doi.org/10.1364/BOE.8.002932
107. Ji YB, Seung Jae Oh, Kang S-G, Heo J, Kim S-H, Choi Y, Song S, Son HY, Kim SH, Lee JH, Haam SJ, Huh YM, Chang JH, Joo C, Suh J-S (2016) Terahertz reflectometry imaging for low and high grade gliomas. Sci Rep 6(1):1–9. https://doi.org/10.1038/srep36040
108. Limin Wu, Degang Xu, Wang Y, Liao B, Zhinan Jiang Lu, Zhao ZS, Nan Wu, Chen T, Feng H, Yao J (2019) Study of in vivo brain glioma in a mouse model using continuous-wave terahertz reflection imaging. Biomed Opt Express 10(8):3953–3962. https://doi.org/10.1364/BOE.10.003953
109. Cheon H, Yang HJ, Son J-H (2017) Toward clinical cancer imaging using terahertz spectroscopy. IEEE J Sel Top Quantum Electron 23(4):8600109. https://doi.org/10.1109/JSTQE.2017.2704905
110. Hoshina H, Hayashi A, Miyoshi N, Fukunaga Y, Otani C (2009) Terahertz pulsed imaging of frozen biological tissues. Appl Phys Lett 94:123901. https://doi.org/10.1063/1.3106616
111. Son J-H, Seung Jae Oh, Cheon H (2019) Potential clinical applications of terahertz radiation. J Appl Phys 125:190901. https://doi.org/10.1063/1.5080205
112. Wallace VP, Fitzgerald AJ, Shankar S, Flanagan N, Pye R, Cluff J, Arnone DD (2004) Terahertz pulsed imaging of basal cell carcinoma ex vivo and in vivo. Br J Dermatol 151(2):424–32. https://doi.org/10.1111/j.1365-2133.2004.06129.x
113. Oh SJ, Kim S-H, Ji YB, Jeong K, Park Y, Yang J, Park DW, Noh SK, Kang S-G, Huh Y-M, Son J-H, Suh J-S (2014) Study of freshly excised brain tissues using terahertz imaging. Biomed Opt Expr 5(8):2837–2842
114. Liu Y, Hao L, Meiqiong T, Jiaoqi H, Wei L, Jinying D, Xueping C, Weiling F, Yang Z (2019) The medical application of terahertz technology in non-invasive detection of cells and tissues: opportunities and challenges. RSC Adv 9(17):9354–9363
115. Bykhovski A, Globus T, Khromova T, Gelmont B, Woolard D (2007) An analysis of the THz frequency signatures in the cellular components of biological agents. Int J High Speed Electron Syst 17(02):225–237. https://doi.org/10.1142/S012915640700445X
116. Yang X, Yang Ke, Luo Y, Weiling Fu (2016) Terahertz spectroscopy for bacterial detection: opportunities and challenges. Appl Microbiol Biotechnol 100(12):5289–5299. https://doi.org/10.1007/s00253-016-7569-6
117. Park SJ, Hong JT, Choi SJ, Kim HS, Park WK, Han ST, Park JY, Lee S, Kim DS, Ahn YH (2014) Detection of microorganisms using terahertz metamaterials. Sci Rep 4:4988. https://doi.org/10.1038/srep04988
118. Park SJ, Son BH, Choi SJ, Kim HS, Ahn YH (2014) Sensitive detection of yeast using terahertz slot antennas. Opt Express 22(25):30467–30472. https://doi.org/10.1364/OE.22.030467
119. Park SJ, Cha SH, Shin GA, Ahn YH (2017) Sensing viruses using terahertz nano-gap metamaterials. Biomed Opt Express 8(8):3551–3558. https://doi.org/10.1364/BOE.8.003551
120. Chen H-T, Padilla WJ, Zide JMO, Gossard AC, Taylor AJ, Averitt RD (2006) Active terahertz metamaterial devices. Nature 444(7119):597–600. https://doi.org/10.1038/nature05343
121. Chen H-T, Padilla WJ, Averitt RD, Gossard AC, Highstrete C, Lee M, O'Hara JF, Taylor AJ (2008) Electromagnetic metamaterials for terahertz applications. Terahertz Sci Technol 1(1):42–50. https://doi.org/10.1117/12.751613
122. Tao Hu, Chieffo LR, Brenckle MA, Siebert SM, Liu M, Strikwerda AC, Fan K, Kaplan DL, Zhang X, Averitt RD, Omenetto FG (2011) Metamaterials on paper as a sensing platform. Adv Mater 23(28):3197–3201. https://doi.org/10.1002/adma.201100163
123. O'Hara JF, Withayachumnankul W, Al-Naib I (2012) A review on thin-film sensing with terahertz waves. J Infrared Millimeter Terahertz Waves 33:245–291. https://doi.org/10.1007/s10762-012-9878-x
124. Tao Hu, Brenckle MA, Yang M, Zhang J, Liu M, Siebert SM, Averitt RD, Mannoor MS, McAlpine MC, Rogers JA, Kaplan DL, Omenetto FG (2012) Silk-based conformal, adhesive, edible food sensors. Adv Mater 24(8):1067–1072. https://doi.org/10.1002/adma.201103814
125. O'Hara JF, Singh R, Brener I, Smirnova E, Han J, Taylor AJ, Zhang W (2008) Thin-film sensing with planar terahertz metamaterials: sensitivity and limitations. Opt Express 16(3):1786–1795. https://doi.org/10.1364/OE.16.001786
126. Azad AK, Dai J, Zhang W (2006) Transmission properties of terahertz pulses through subwavelength double split-ring resonators. Opt Lett 31(5):634–636. https://doi.org/10.1364/OL.31.000634
127. Menikh A, Mickan SP, Liu H, Maccoll R, Zhang X-C (2004) Label-free amplified bioaffinity detection using terahertz wave technology. Biosens Bioelectron 20:658–62. https://doi.org/10.1016/j.bios.2004.03.006
128. Xiaojun Wu, Quan B, Pan X, Xinlong Xu, Xinchao Lu, Changzhi Gu, Wang Li (2013) Alkanethiol-functionalized terahertz metamaterial

as label-free, highly-sensitive and specific biosensor. Biosens Bioelectron 42:626–631. https://doi.org/10.1016/j.bios.2012.10.095
129. Yoon SA, Cha SH, Jun SW, Park SJ, Park J-Y, Lee S, Kim HS, Ahn YH (2020) Identifying different types of microorganisms with terahertz spectroscopy. Biomed Opt Expr 11(1). https://doi.org/10.1364/BOE.376584
130. Kastek M, Piątkowski T, Dulski R, Chamberland M, Lagueux P, Farley V (2012) Multispectral and hyper spectral measurements of soldier's camouflage equipment. Proc SPIE 8382:83820K. https://doi.org/10.1117/12.918393
131. Kowalski M, Kastek M, Palka N, Polakowski H, Szustakowski M, Piszczek M (2013) Investigation of concealed objects detection in visible, infrared and terahertz ranges of radiation. Photon Lett Poland 5(4):167–169. https://doi.org/10.4302/plp.2013.4.16
132. Kowalski M, Kastek M, Szustakowski M (2014) Concealed objects detection in visible, infrared and terahertz ranges. World Acad Sci Eng Technol Int J Civil Environ Eng 8:10. https://doi.org/10.4302/plp.2013.4.16
133. Kowalski M (2019) Hidden object detection and recognition in passive terahertz and mid-wavelength infrared. J Infrared Millimeter Terahertz Waves 40:1074–1091. https://doi.org/10.1007/s10762-019-00628-7
134. Afsah-Hejri L, Hajeb P, Ara P, Ehsani RJ (2019) A comprehensive review on food applications of terahertz spectroscopy and imaging. Compr Rev Food Sci Food Saf 18. https://doi.org/10.1111/1541-4337.12490
135. Jordens C, Rutz F, Koch M (2006) Quality assurance of chocolate products with terahertz imaging. 9th European Conference on NDT, Berlin (Germany) (ECNDT)
136. Shi Y, Chang JS, Esposito CL, Lafontaine C, Berube MJ, Fink JA, Espourteille FA (2011) Rapid screening for pesticides using automated online sample preparation with a high-resolution benchtop orbitrap mass spectrometer. Food Addit Contam 28(10):1383–1392. https://doi.org/10.1080/19440049.2011.590822
137. Li B, Cao W, Mathanker S, Zhang W, Wang N (2010) Preliminary study on quality evaluation of pecans with terahertz time-domain spectroscopy. Proc SPIE Int Soc Opt Eng 7854. https://doi.org/10.1117/12.882201
138. Lee Y-K, Choi S-W, Han S-T, Woo DH, Chun HS (2012) Detection of foreign bodies in foods using continuous wave terahertz imaging. J Food Prot 75(1):179–83. https://doi.org/10.4315/0362-028X.JFP-11-181
139. Wang C, Qin J, Wendao X, Chen M, Xie L, Ying Y (2018) Terahertz imaging applications in agriculture and food engineering: a review. Trans ASABE 61(2):411–424. https://doi.org/10.13031/trans.12201
140. Jiang Y, Ge H, Lian F, Zhang Y, Xia S (2016) Early detection of germinated wheat grains using terahertz image and chemometrics. Sci Rep 6:21299. https://doi.org/10.1038/srep21299
141. Afsharinejad A, Davy A, O'Leary P, Brenann C (2018) Transmission through single and multiple layers of plant leaves at THz frequencies. IEEE Global Communications Conference, pp. 1–6. https://doi.org/10.1109/GLOCOM.2017.8254561
142. Jordens C, Koch M. Detection of foreign bodies in chocolate with pulsed terahertz spectroscopy. Opt Eng 47(3):037003. https://doi.org/10.1117/1.2896597.
143. Hiromoto N, Shiba N, Yamamoto K (2013) Detection of a human hair with polarization-dependent THz-time domain spectroscopy. 38th International Conference on Infrared, Millimeter, and Terahertz Waves (IRMMW-THz), pp. 1–2. https://doi.org/10.1109/IRMMW-THz.2013.6665804
144. Ok G, Kim HJ, Chu HS, Choi S-W (2014) Foreign-body detection in dry food using continuous sub-terahertz wave imaging. Food Control 42:284–289. https://doi.org/10.1016/j.foodcont.2014.02.021
145. Yoneyama H, Yamashita M, Kasai S, Ito H, Ouchi T (2007) Application of terahertz spectrum in the detection of harmful food additives. Joint 32nd International Conference on Infrared and Millimeter Waves and the 15th International Conference on Terahertz Electronics. https://doi.org/10.1109/ICIMW.2007.4516498.
146. Xiao-Li Z, Jiu-Sheng L (2010) Diagnostic techniques of talc powder in flour based on the THz spectroscopy Diagnostic techniques of talc powder in flour based on the THz spectroscopy. Journal of Physics: Conference Series, 3rd International Photonics & Opto Electronics Meetings 276:2–5. https://doi.org/10.1088/1742-6596/276/1/012234
147. Massaouti M, Daskalaki C, Gorodetsky A, Koulouklidis AD, Tzortzakis S (2013) Detection of harmful residues in honey using terahertz time-domain spectroscopy. Appl Spectrosc 67(1):1264–1269. https://doi.org/10.1366/13-07111
148. Inamo M, Sakai K, Kiwa T, Tsukada K (2016) Application to non-destructive evaluation of gas barrier films using a high-speed terahertz time-domain spectroscopy. 2016 Progress in Electromagnetic Research Symposium (PIERS), p. 3921. https://doi.org/10.1109/PIERS.2016.7735475
149. Goryachuk A, Begaeva VA, Khodzitsky MK, Truloff AS (2015) The optical properties and spectral features of malignant skin melanocytes in the terahertz frequency range. J Phys 735. https://doi.org/10.1088/1742-6596/735/1/012073
150. Qin B, Li Z, Fangrong Hu, Cong Hu, Chen T, Zhang H, Zhao Y (2018) Highly sensitive detection of carbendazim by using terahertz time-domain spectroscopy combined with metamaterial. IEEE Trans Terahertz Sci Technol 8(2):149–154. https://doi.org/10.1109/TTHZ.2017.2787458
151. Tan Z, Jun L, Luo J, Xie J (2014) Continuous-wave terahertz imaging applied to detect infestations caused by insects in grain. Adv J Food Sci Technol 6(2):271–274. https://doi.org/10.19026/ajfst.6.23
152. Afsharinejad A, Davy A, Naftaly M (2017) Variability of terahertz transmission measured in live plant leaves. IEEE Geosci Remote Sens Lett 14(5):636–638. https://doi.org/10.1109/LGRS.2017.2667225
153. Radhanpura K, Farrant D, Du J (2017) Measurement of agricultural products using terahertz hyperspectral imaging. 42nd International Conference on Infrared, Millimeter, and Terahertz Waves (IRMMW-THz). https://doi.org/10.1109/IRMMW-THz.2017.8066930
154. Adnan Zahid, Muhammad Imran and Qammer HA (2018) Terahertz sensing at nano-scale for future agriculture. Res Rev: J Bot Sci 7(4). https://doi.org/10.1002/9781119552635.ch11
155. Heimbeck MS, Ng WR, Golish DR, Gehm ME, Everitt HO (2015) Terahertz digital holographic imaging of voids within visibly opaque dielectrics. IEEE Trans Terahertz Sci Technol 5(1):110–116. https://doi.org/10.1109/TTHZ.2014.2364511
156. Zhang Y, Wang C, Huai B, Wang S, Zhang Y, Wang D, Rong L, Zheng Y (2021) Continuous-wave THz imaging for biomedical samples. Appl Sci 11(1). https://doi.org/10.3390/app11010071
157. Rong Lu, Tang C, Wang D, Li B, Tan F, Wang Y, Shi X (2019) Probe position correction based on overlapped object wavefront cross-correlation for continuous-wave terahertz ptychography. Opt Express 27(2):938–950. https://doi.org/10.1364/OE.27.000938
158. Peng L, Luo C, Wang H, Cheng Y, Yang Q, Liu K (2019) Application of phase retrieval algorithms in terahertz coded aperture imaging. The International Radar Symposium IRS 2019, June 26–28, Germany. https://doi.org/10.23919/IRS.2019.8768124